THE UNIVERSITY *of* EDINBURGH

This thesis has been submitted in fulfilment of the requirements for a postgraduate degree (e. g. PhD, MPhil, DClinPsychol) at the University of Edinburgh. Please note the following terms and conditions of use:

- This work is protected by copyright and other intellectual property rights, which are retained by the thesis author, unless otherwise stated.
- A copy can be downloaded for personal non-commercial research or study, without prior permission or charge.
- This thesis cannot be reproduced or quoted extensively from without first obtaining permission in writing from the author.
- The content must not be changed in any way or sold commercially in any format or medium without the formal permission of the author.
- When referring to this work, full bibliographic details including the author, title, awarding institution and date of the thesis must be given.

Towards a computational screening programme for energetic materials

Imogen Louise Christopher

This thesis is submitted for the degree of

Doctor of Philosophy

The University of Edinburgh

2024

Declaration

I declare that this thesis was composed by myself, that the work contained herein is my own except where explicitly stated otherwise in the text, and that this work has not been submitted for any other degree or processional qualification except as specified.

Imogen Christopher

2024

Abstract

Energetic materials, encompassing explosives, pyrotechnics and propellants, are of vital importance to the world. They have a range of applications including military, aerospace, industrial and even domestic applications. Their use is ubiquitous throughout the world but historically there has not been a systematic development process for new materials. Because of their ability to release vast amounts of energy upon initiation energetic materials are inherently dangerous to work with. Therefore, it is important to be able to understand not only how dangerous a material can be, but also why these materials behave the way they do.

Computational methods provide a valuable tool for screening new energetic materials without having to handle potentially dangerous samples. This thesis is focused on the development of a fully computational screening programme for new energetic materials, wherein the properties of hypothesised materials can be calculated, and the performance of the material assessed in a quick and safe manner.

Chapter 3 details a study to determine the best method to calculate the heat of formation of solid EMs. The heat of formation of energetic materials is vital to know, as it is routinely used in software such as EXPLO-5 to calculate the detonation parameters of EMs. While heat of formation can be measured experimentally, several methods have been proposed to calculate heat of formation without having to carry out any experimental measurements. Methods reported for calculating gas phase heats of formation include group equivalence methods and isodesmic equations, as well as a simple semi-empirical quantum mechanical method, known as PM7. Within this thesis these three methods have been compared using a chemically broad series of 20 CHNO containing energetic molecules, while PM7 was tested with a further 31 inorganic compounds. PM7 performed the best (R^2 = 0.995). Methods for calculating sublimation or lattice enthalpies, used to calculate solid-state heats of formation, are also evaluated here. The work here allows for heats of formation of a range of systems, single-component molecular solids, salts, and co-crystals to be calculated. For the latter it is noted that an estimate of the lattice

energy can be obtained from simply summing the energy terms for the corresponding co-former species.

Chapters 4 and 5 are focused on utilising a recently developed computational model to predict the impact sensitivity from a crystal structure alone. This method models the vibrational up-pumping of initial impact energy through a crystal structure, and has thus far accurately predicted the relative sensitivity of well-known EMs, is used extensively to explore structure-property relationships of energetic co-crystals and polymorphic series.

Chapter 4 shows how this method can be used to predict the sensitivity of a co-crystal consisting of energetic nitrotriazolone (NTO) and non-energetic 4,4'-bipyridine (BIPY). This chapter also highlights the power of computational methods to understand the structural changes of systems when experimental methods fall short. High pressure crystallography showed unusual behaviour with the crystal undergoing a colour change from colourless to yellow above 4 GPa. This, combined with the knowledge of other bipyridine containing co-crystals led to the assumption that the system undergoes a phase transition from co-crystal to salt at high pressure. However, computational modelling of the proton transfer system through potential energy surfaces along the N—H···N vector along with fitting of 1D Schrodinger equations confirmed that the resulting co-crystal of NTO.BIPY is a proton migration system, with the colour change being due to system compression. Prediction of the impact sensitivity of the co-crystal suggests that the sensitivity is increased in relation to the parent energetic, NTO. This is due to the introduction of BIPY which increases the number of vibrational pathways to initiation. However, the introduction of the non-energetic BIPY simultaneously dilutes the energetic power of this system.

Finally in Chapter 5 the effect that polymorphism can have on impact sensitivity is explored. Analysis has been carried out on experimentally determined polymorphs of RDX and DNAN, which both exhibit high pressure polymorphs. For both RDX and DNAN the most sensitive structures are those which exist at high pressures. And for RDX this offers more detailed understanding of the detonation pathway of α-RDX, suggesting that the less sensitive α-RDX undergoes a phase change or molecular conformation change to a more sensitive form during impact sensitivity testing. The results for DNAN polymorphs suggest interesting results as the high pressure form,

DNAN-VI is predicted to be highly sensitive, even though molecules pack in parallel layers. This crystal packing is usually indicative of insensitivity to impact, which is contradicted here. It is postulated that the change in the vibrational modes of the methoxy group, which are largely controlled by crystal packing, leads to the increase in the predicted sensitivity. The latter half of Chapter 5 will focus on how the impact sensitivity model will function in a fully computational screening programme. The impact sensitivity of structures of EMs obtained through crystal structure prediction are calculated, and show that impact sensitivity is expected to change significantly across polymorphic forms, therefore when devising a computational screening programme, the best estimation that may be possible is to classify new energetic materials as either primary or secondary explosives.

The work presented in this thesis aims to provide pathways for developing a fully computational screening programme for new energetic materials, covering methods used to predict detonation properties through the molecular structure and implementing an *ab initio* method to predict the sensitivities of solid structures. The latter has shown that crystal packing plays a large role in the sensitivity of a material and has also provided insight into structure-property relationships which can be used for the design of new and safe energetic materials.

Lay Summary

Energetic materials, which include explosives, pyrotechnics, and propellants, are essential components in various applications such as the military, aerospace, industry, and even in households. These materials are highly valuable due to their ability to release significant amounts of energy, but they are also inherently dangerous to handle. Therefore, understanding their safety and behaviour is crucial. To address this, computational methods have been developed to screen and assess new energetic materials without needing to work with potentially hazardous samples.

This thesis focuses on creating a fully computational screening program for these materials, allowing researchers to calculate the properties and performance of hypothetical materials quickly and safely. In Chapter 3 different methods are explored to calculate the heat of formation of solid energetic materials, which is crucial for predicting their detonation parameters. While this can be measured experimentally, the study compares various computational methods and determines the best method for calculating the solid heat of formation for a wide range of different sub-groups of energetic materials.

Chapters 4 and 5 introduce a computational model that predicts the impact sensitivity of energetic materials based solely on their crystal structure. This model has proven largely accurate in predicting the sensitivity of well-known energetic materials. Additionally, the thesis explores the impact of polymorphism on sensitivity, particularly in high-pressure polymorphs. It is discovered that high-pressure forms are often more sensitive, and this understanding provides insights into the structure-property relationships of these materials. Overall, this thesis aims to pave the way for a comprehensive computational screening program for new energetic materials. It includes methods for predicting heats of formation based on molecular structure and the testing of an *ab initio* approach for predicting the sensitivity of solid materials. The research underscores the importance of crystal packing and the effects of co-crystallisation on material sensitivity and provides valuable insights into structure-property relationships for designing safer energetic materials.

Acknowledgements

Doing a Ph.D. is incredibly hard work, and even more so when a global pandemic decides to interrupt your studies. I would say the fact that this thesis has been written is a miracle, but it is not. It is the evidence that I have had an incredible amount of support around me, and that is something which cannot be taken for granted.

First, I must give thanks to my supervisors, Professor Carole Morrison for her amazing passion and dedication as a supervisor – having you as a supervisor is truly one of the formative parts of my life. And to Professor Colin Pulham whose tenacity for energetics is wonderful, it has been a pleasure to work with you these past years. Thanks also go to Professor Simon Parsons for enlightening and valuable conversations throughout my academic career.

Thanks go to Dr Adam Michalchuk without whom there would be no vuppy code, and no thesis. To Dr Xiaojiao Liu and Dr Hayleigh Lloyd thank you for all work done on synthesising, and characterisation of NTO.BIPY. Dr Matt Reeves from the Parsons group, thanks for the code of Mr PIXEL which was less traumatising to use in my PhD than it was in my master's project. Thank you to Dr. Nisa Atceken for introducing me to the need for heats of formation. To Dr Lisette Warren and Jack Hemingway, thank you for being wonderful members of the Morrison group and for being at the end of a team's call whenever we needed to share ideas.

A huge thank you too to Dr Murray Low for being a force to be reckoned with and for modelling what a great educator should look like. And although I didn't spend as much time in there as I had hoped, I cannot take for granted the support of those who have passed through the doors of Office 82 throughout the years; Hannah Logan for being there from before the Sunamp days; Emily Goddard, Rebecca Rae, Nisa Atceken, Akachai Khumsri, Fi McIver-Jones, Angela Fong, Edmund Morris and Monica Chandwani.

My everlasting thanks goes to the friends I have made along the way; Emily Payne, Katie Grant, Lara Dunn, Victoria Porley, Ella Rice and Georgia Dodsworth. Without you all life would have been a lot harder, and a lot less fun.

Thank you to my family who have supported me especially, to mum and Holly for their check-ins and nodding along with whatever I have told them, even though I’m sure it’s gone in one ear and out the other. And of course, to Jonathan, best friend, confidant, shoulder to cry on – thanks for being the best person I ever could have hoped for.

Contents

List of Abbreviations 11
Chapter 1 12
Introduction 12
1.1 A brief introduction to, and history of, energetic materials 12
1.2 Predictive Methods 15
1.3. Co-crystallisation 21
1.4 Polymorphism 23
1.5 Development of a fully computational screening programme 24
Aims of this thesis 24
References 27
Chapter 2 34
Computational Methods 34
2.1 *Ab initio* methods 34
2.1.1. Hamiltonian operator, $\boldsymbol{H}$ 35
2.1.2. Wavefunction, $\boldsymbol{\psi}$ 37
2.2. Solid state calculations 37
Geometry Optimisation 39
Vibrational frequency calculation 40
2.3. Semi empirical methods 41
PIXEL 43
2.4. Specialised software used for modelling energetic materials 44
Local Mode Vibrational Analysis - LModeA. 44
EXPLO5 44
VUP.PY 46
References 52
Chapter 3 56
Calculation of heat of formation and determination of bond strengths by local mode analysis 56
3.1. Introduction 56
3.2. Computational Methods 61
3.3. Results and Discussion 64
Calculating gas phase heats of formation. 64
Calculating solid heats of formation 70
Local force constant calculations. 75
3.4. Conclusion 77

References ... 78
Chapter 4 ... 86
Tuning energetic properties through co-crystallisation: nitrotriazolone and 4,4'-bipyridine. ... 86
4.1. Introduction ... 86
4.2. Computational Methods ... 89
4.3. Results and Discussion ... 91
4.3.1. Crystal structure and high pressure behaviour of NTO.BIPY ... 91
4.3.2. Response to pressure ... 93
4.3.3. High pressure computational modelling ... 95
4.3.4. Calculation of detonation parameters ... 100
4.3.5. Impact sensitivity calculations. ... 102
4.4. Conclusions ... 109
5.1 Introduction ... 116
5.2. Computational Methods ... 118
5.3. Results and Discussion ... 121
5.3.1. 1,3,5trinito-1,3,5-triazinane (RDX) ... 121
5.3.2. 2,4-dinitroanisole (DNAN) ... 132
5.3.3. 1,3,5-trinitrotoluene (TNT) ... 147
5.3.4. Nitrotriazalone (NTO) ... 149
Conclusions ... 153
Chapter 6 – Conclusions and Future Work ... 161
Appendices ... 164

List of Abbreviations

2PhonDoS	2-phonon density of states
BIPY	4,4’-bipyridine
CL-20	Hexanitrohexaazaisowurtzitane
CoM	Centre of Mass
DFT	Density Functional Theory
DFPT	Density Functional Perturbation Theory
DNAN	2,4-Dinitroanisole
DoS	Density of States
EM	Energetic Material
ESP	Electrostatic Potential
FOX-7	1,1-diamino-2,2-dinitroethylene
HMX	1,3,5,7-Tetranitro-1,3,5,7-tetrazocane
HNB	Hexanitrobenzene
IS	Impact Sensitivity
NCI	Non-covalent interaction
NTO	Nitrotriazolone
PES	Potential energy surface
RDX	1,3,5-Trinitro-1,3,5-triazinane
TATB	2,4,6-Trinitrobenzene-1,3,5-triamine
TNT	Trinitrotoluene

Chapter 1

Introduction

1.1 A brief introduction to, and history of, energetic materials

Energetic materials (EMs), including explosives, propellants, and pyrotechnics, are of great importance to the modern world as they possess the ability to release large amounts of energy upon initiation. This has ensured their use in a range of applications such as military, industrial, and commercial applications. External stimulations, such as shock, heat, friction or spark lead to the breakdown of the chemical structure which results in the rapid release of energy. The three different ways in which EMs can behave, namely detonation, deflagration, and combustion, is categorised by the rate determining step and the propagation rate. Detonation results in a shock wave being generated. This shock wave propagates through the material and leads to the temperature and pressure increasing which allows for further propagation of the shock wave. Detonation is defined by the speed of this shock wave being super-sonic. Deflagration is characterised by a sub-sonic combustion in a material where the fuel and oxidiser are pre-mixed. Finally, combustion is an exothermic, sub-sonic, chemical reaction between a fuel and an oxidiser. The manner in which the energy is released determines the application for the material, with for instance materials which deflagrate typically used in applications where an object needs to be moved, such as in propellants. Classification of EMs is typically dependent upon impact sensitivity – primary energetics have a low impact sensitivity, typically categorised at less than 4 J of energy needed to induce detonation and are particularly dangerous to handle because of this. Conversely secondary energetics do not detonate readily and typically burn or deflagrate, however detonation of secondary explosives can be achieved by shock waves.[1]

The first known explosive was "black powder", also known as gunpowder. Developed in China in the 10th century it is a mixture of KNO_3, S_8 and charcoal.[2] Gunpowder was used in military applications throughout modern history, and indeed it was only the onset of industrialised warfare which led to the rapid development of new EMs in the 19th and 20th centuries.

Nitroglycerin (Figure 1) was first synthesised in 1847, but had limited use in mining applications, due to its inability to be detonated by a fuse.[3] The invention of a blasting cap by Alfred Nobel solved this problem. His invention consisted of a small amount of primary explosive, which generated a shock wave of sufficient power to induce detonation of the nitroglycerin. Blasting caps are still used today, to allow for the detonation of less sensitive, but more powerful, secondary explosives. Further work by Nobel on nitroglycerin led to the invention of dynamite, a mixture of nitroglycerin with sorbents and other additives to stabilise the nitroglycerin, in 1867. Dynamite quickly overtook black powder as the explosive of choice as it is safer to handle and allowed for widespread use in construction applications.

The realisation in 1891 that 2,4,6-trinitrotoluene (TNT, Figure 1.1), used as a yellow dye at the time, possesses explosive powers led to its widespread adoption, in part due to its greater insensitivity compared to dynamite.[4] To this day TNT is typically used as the standard to which other EMs are compared to. The onset of the second world war prompted the development and refinement of the syntheses of new EMs to rapidly increase, with the streamlined production of 2,4,6-Trinitrobenzene-1,3,5-triamine (TATB), 1,3,5-Trinitroperhydro-1,3,5-triazine (RDX) and 1,3,5,7-Tetranitro-1,3,5,7-tetrazocane (HMX) being the result (Figure 1).[5]

Considering the range over which EMs are used, from military to industrial to aerospace applications, it is vital that EMs are chemically stable to thermal, mechanical, and electrical stimuli during storage and transportation, whilst maintaining the ability to detonate only when required. The 1980s saw considerable effort to reduce the sensitivity of EMs by taking known high energy density materials (which are often sensitive to stimuli) and binding them with insensitive energetic binders and plasticisers, resulting in polymer-bonded explosives (PBXs), where the EM is dispersed amongst the binders. A commonly used example is composition-4, C4, which is a mixture of RDX and dioctyl sebacate as the plasticiser, and thickeners such as rubber.[6]

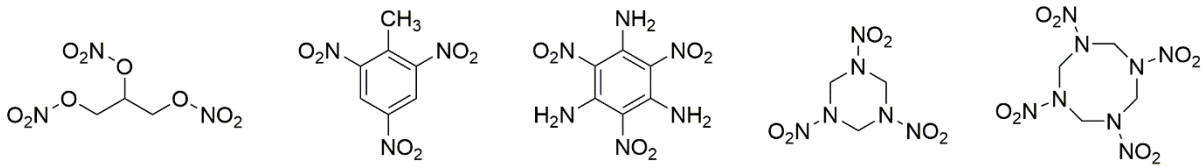

Figure 1.1 Molecular structures of commonly used energetic materials.

While creating mixtures is a straightforward and proven way to alter the properties of EMs, sensitivity is not the only pressing issue when it comes to developing new formulations. Another factor to investigate is the long term effects of EMs, including the toxicity and environmental impact. A prime example of this is the need to phase out lead in EMs. Lead azide, $Pb(N_3)_2$, is a highly sensitive material which is used to initiate secondary explosives, while lead salts are frequently used as a burn rate modifier in double based propellants.[7–9] REACH legislation has placed lead on the candidate list for substances of very high concern, meaning it could be placed on the annex list due to environmental and health concerns. A number of potential replacements have been suggested, with the copper-coordination polymer known as DBX-1 being a well-known example[10]. Current research is still being carried out to understand the role that lead plays in double based propellants, so that suitable replacements can be chosen.[11,12] Nitroaromatic compounds, including TNT, RDX and HMX, are known to have a significant environmental impact.[13,14] TNT is particularly resistant to biodegradation and is known to induce reproductive toxicity in organisms.[15] While formulating mixtures using these nitroaromatic EMs is attractive due to the avoidance of having to implement new industrial synthetic procedures, it is obvious that a focus in the development of new EMs must be on designing new energetic molecules, or somehow tailoring the properties of existing materials.

Computational screening methods, which are used to identify and design materials with desirable properties, have the potential to be valuable to the energetic community. Most of the EMs widely in use to this day had been first developed in the middle of the twentieth century. Therefore, structure-property relationships, which can increasingly be explored via modelling, could not be understood at the time. With the near exponential increase in computing power over the past 50 years, the potential to not only investigate structure property relationships on a case-by-case basis, but to use these relationships to propose design criteria for new EMs can now

be realised. The matter, therefore, now turns to how to understand structure-property relationships.

Computational screening methods have the potential to play a vital role in the development of new EMs. Computer processing power is more efficient than ever before, and as such fast and reliable predictive methods have the potential to revolutionise EM development. In other chemical industries, notably the pharmaceutical industry, computational screening plays a vital role, where it is used to identify new drugs and new druggable binding sites, either directly through atomistic simulation, or through the use of quantitative structure-activity relationships.[16,17] The overwhelming success of computational methods in drug design highlights its usefulness in other chemical industries. The EM industry is the perfect candidate for developing computational screening programmes as the synthesis of new EMs is potentially highly dangerous, so computational screening can reduce user hazards, while additionally establishing structure-property relationships for the systematic design of new EMs with tailored properties.

1.2 Predictive Methods

Historically, it has been difficult to implement design criteria for new EMs. Properties such as impact sensitivity are not known to correlate directly with easily known quantities such as chemical formula. Several relationships between molecular and solid structures with impact sensitivity have been proposed over the years. As noted above, EMs are commonly nitrated materials, as the nitro group provides both oxygen and nitrogen, with the latter acting as a fuel alongside the hydrocarbon component. Upon initiation, the products formed are typically N_2, CO_2 and H_2O, the formation of which provides the thermodynamic driver for the reaction. An early metric that is widely adopted to determine the explosive power of a material is the oxygen balance, OB%, which describes the degree to which an explosive molecule can be oxidised.[18] The method for calculating OB% is described in equation 1, which was first proposed in 1948.

$$OB\% = \frac{-1600}{Mol.wt.of\ compound}\left(2X + \frac{Y}{2} + M - Z\right)$$

Where X = number of carbon atoms, Y = number of hydrogen atoms, Z = number of oxygen atoms and M = number of metal atoms. In effect, OB% gives a measure of

the number of oxygen atoms in excess, or deficient for 100 g of a compound. As OB% approaches zero (i.e. no excess or deficient oxygen following combustion), is it thought that the properties of the material, i.e. their strength and explosive power, approach their maxima. Although it was initially proposed that OB% could be correlated against impact sensitivity, this has since been disproven.[19,20]

Software programmes, including CHEETAH[21] and EXPLO-5[22] are routinely used by experimentalists to predict detonation parameters of EMs. They rely on equations of state to model the detonation of an EM and generates useful energetic parameters including the heat of detonation, the velocity of detonation, the detonation pressure and temperature, and the detonation products. Only three input parameters are needed: (i) the density of the standard state EM, (ii) the condensed phase heat of formation, ΔH_f, and (iii) the chemical formula. The last term is readily obtainable, while the first is easily measured *via* crystallographic methods; however, the heat of formation is a harder parameter to measure. It can be measured experimentally using bomb calorimetry to measure the heat of reaction, and then applying Hess's law (and using the standard state heats of formation for the combustion products H_2O, CO_2 and N_2) to calculate the heat of formation of the EM. Obviously, combustion of EMs poses an inherent danger and so moving away from calorimetry is essential for safer characterisation of EMs. Additionally, there must be sufficient material to be able to measure the heat of reaction, which can be difficult if materials are being synthesised in order to be analysed in a high-throughput screening process of new materials. Being able to predict the ΔH_f of a material is therefore an important tool to have, especially if it can be done in a quick and simple way.

Aside from the use of the thermochemical codes, there are scant other predictive methods used in the field of energetics. Recently, work has turned to formulating a model which can be used to predict the sensitivity of a material. Sensitivity can be categorised in several different ways, including heat, shock, friction, spark, and impact. Taking the last one of these, impact sensitivity (IS) is literally a measure of how much energy is required to initiate a material and is a vital metric to assess the safety of the EM, and as mentioned above determines the application for an EM. The development of secondary EMs, for instance, focuses on combining insensitivity with detonation velocities comparable to primary EMs. IS can be reported in several ways, but all methods rely on the principle of a drop weight test, with the most

common used apparatus being the BAM hammer fall test (Figure 1.2). Dropping standard weights from various heights onto a material is used to obtain an h_{50} value, which is the height at which 50 % of samples will initiate when the weight is dropped. However, not all impact sensitivities are reported as h_{50}. Another value that is reported is the limiting impact energy, E_0, below which no impacts lead to initiation.

As well as confusion in reported impact sensitivities, to measure IS by the drop hammer method sufficient material must be synthesised to carry out the multiple tests that are required. Not only can a computational predictive method provide clarity to IS measurements reported in various ways, it can also reduce the risk that is associated with working with potentially dangerous materials. Given this premise, it is unsurprising that the topic of predicting impact sensitivity has been in discussion for multiple decades. However, lack of knowledge of the actual detonation pathway for EMs has limited progress. Reports in this area include that by Bowden and Yoffe, who proposed that mechanical means of detonation, such as impact or friction, result in the formation of “hot spots” within a crystal.[23] These hot sports propagate throughout the bulk material, leading to bond dissociation and thus an explosion.

Figure 1.2. BAM fall hammer test

Several correlations between molecular and crystalline properties and IS have been proposed. A particularly simple approach concerns a correlation between the strength of the weakest bond of the energetic molecule and bulk material impact sensitivity. Politzer *et. al.*[24] proposed a link between the strength of the C—NO_2 bond and the computed electrostatic potential maxima on the molecular surface. The C—NO_2 bond is typically the weakest bond in an energetic molecule, and the rupture of

such a bond is believed to be critical to the decomposition process of a material. Therefore, the strength of the weakest bond can give a good idea of how easily a molecule will fragment. This work was generalised further by Murray *et. al.*,[25] who further corroborated a correlation between impact sensitivity and a computed molecular surface electrostatic potential. However, this work was limited to nitroaromatic and nitroheterocycle EMs only. While many EMs fall into these two families, there are plenty of other EMs, such as azides, that do not. Moreover, while considering the strength of the weakest bond may be of importance when it comes to molecular design, focusing on molecular structure alone ignores the contribution of the crystal structure in directing material properties.

Another common approach which depends on the molecular structure alone is the relationship between impact sensitivity and the energy gap between the highest occupied molecular orbital and lowest unoccupied molecular orbital, the HOMO-LUMO gap. This can be considered as a molecular approximation of the band gap of a crystal, which is the separation of the valence and conduction band (discussed further below). It has been postulated that a small HOMO-LUMO gap will correlate with a more sensitive material, as an electronic excitation will occur more readily, promoting bond breaking and decomposition of the molecule. However, Murray *et. al*[26] have showed that working with molecular HOMO-LUMO gaps does not provide a reliable metric for predicting impact sensitivity.

Others have focused on the electronic band gap arising for the solid state structure of the EM. This is an important step forward, as it allows the effect of crystal packing and intermolecular interactions to be taken into account. Related to the measure of band gaps in solid structures is the mechanism of pressure-induced metallisation,[27] and vibrationally-induced metallisation.[28] Both propose dynamic narrowing of electronic band gaps induced by the shockwave which allows for excited electronic states to be easily reached, resulting in the formation of radicals and other unstable molecular species. This in turn could link into Bowden and Yoffe's hot-spot theory.

While it has been reported that the band gap can give a good measure for the IS of a material,[29] it has been noted that comparisons are only meaningful between EMs with similar structures, e.g. between metal azides or materials in the nitroaniline series (monoamino-2,4,6-trinitrobenzene, 1,3-diamino-2,4,6-trinitrobenzene and

1,3,5-triamino-2,4,6-trinitrobenzene). While this is a valuable resource for comparison of properties between related materials, it does not allow for comparison of properties between the groups, or indeed for a novel EM treated in isolation. It is of vital importance then that a successful predictive method can allow for comparison of properties between structurally diverse materials.

A further solid-state based model which has been proposed to model the detonation mechanism for EMs is the theory of vibrational energy transfer through up-pumping, first proposed by Coffey and Totton[30] and further by Zerilli and Totton.[31] This model describes a mechanism for the localisation of energy in crystalline materials, which can account for the theory of hot spot formations, which are thought to induce initiation in an EM.[32] The model assumes that initial mechanical impact energy initially excites low frequency phonon modes (which equates to intermolecular motion between molecules within the crystal structure). This energy then rapidly transfers into higher energy phonon states though phonon-phonon collisions. This then increases the population of the internal molecular modes of vibration (relating to molecular motion such as bond stretches or angle bends). The enhanced population of these modes then results in covalent bond dissociation, due to extreme vibrational motions, which results in initiation of the material. Typically, methods which are based on multi-phonon up-pumping have relied on experimental inelastic neutron scattering or Raman spectra to predict IS, however experimental data alone has not provided a predictive route. In 2018 Bernstein[33] proposed an *ab initio* method for calculating IS using the vibrational up-pumping method. Here, the top of the phonon bath (i.e., the highest frequency of a mode which can be populated by the initial shock wave) was unwaveringly set at 200 cm^{-1} for all six materials investigated in this study. This is not accurate as the size of the phonon bath region will vary depending on the molecular and crystal structures. For instance, there could be so-called “amalgamated modes”, which are molecular modes of vibration that combine with the phonon bath delocalised modes, and thus muddy the clear-cut divide between the expected 6*Z* (where *Z* = the number of molecules in the crystallographic unit cell) phonon vibrations, and the remaining 3*N*-6*Z* (where *N* = the number of atoms in the unit cell) molecular-based vibrations. Amalgamated modes typically involve the vibration of -NO_2 groups, so for EMs with -NO_2 groups the top of the phonon bath would likely occur at a higher wavenumber compared to EMs that do

not. Bernstein also proposed that overtone coupling pathways (i.e. phonon scatterings originating from the same vibrational state, analogous with overtone coupling seen in vibrational spectroscopy) could occur to the seventh order (i.e. the phonon scatters off itself seven times) to up-pump the vibrational energy up to the molecular modes. This is highly unlikely as the probability of multiple phonon scattering decreases rapidly beyond orders of about two or three.[32]

Work by Michalchuk in 2019[34] has a similar approach to the work of Bernstein, but allows for the top of the phonon bath to be determined on a case-by-case basis, while capping overtone coupling to a more realistic second order limit. In addition, phonon-phonon scattering between different phonon modes (akin to combination modes from vibrational spectroscopy) were also permitted. A range of structurally diverse EMs, exhibiting a broad range of experimental impact sensitivities, were studied. Not only did this provide excellent correlation with experimental results of impact sensitivity, but it also allows for the prediction of impact sensitivities of polymorphs and multi-component systems such as salts and co-crystals. The original method focused on sampling the phonon modes across the whole of the Brillouin zone,[34] but further work showed that sampling the phonons at just the zone-centre (gamma point) of the Brillouin zone was sufficient to differentiate between the primary EMs (IS < 4J) and secondary EMs (IS > 4J), as shown in Figure 1.3.[35] Note, however, by restricting sampling of the phonon bath vibrational modes to gamma-point only, some differentiation between the secondary EMs is lost. This must be tensioned against the considerable speed up (typically a factor of 10) that is achieved by limiting the calculation of vibrational frequencies to gamma-point only. This model will be used extensively in this work in order to predict the sensitivities of several different energetic material systems.

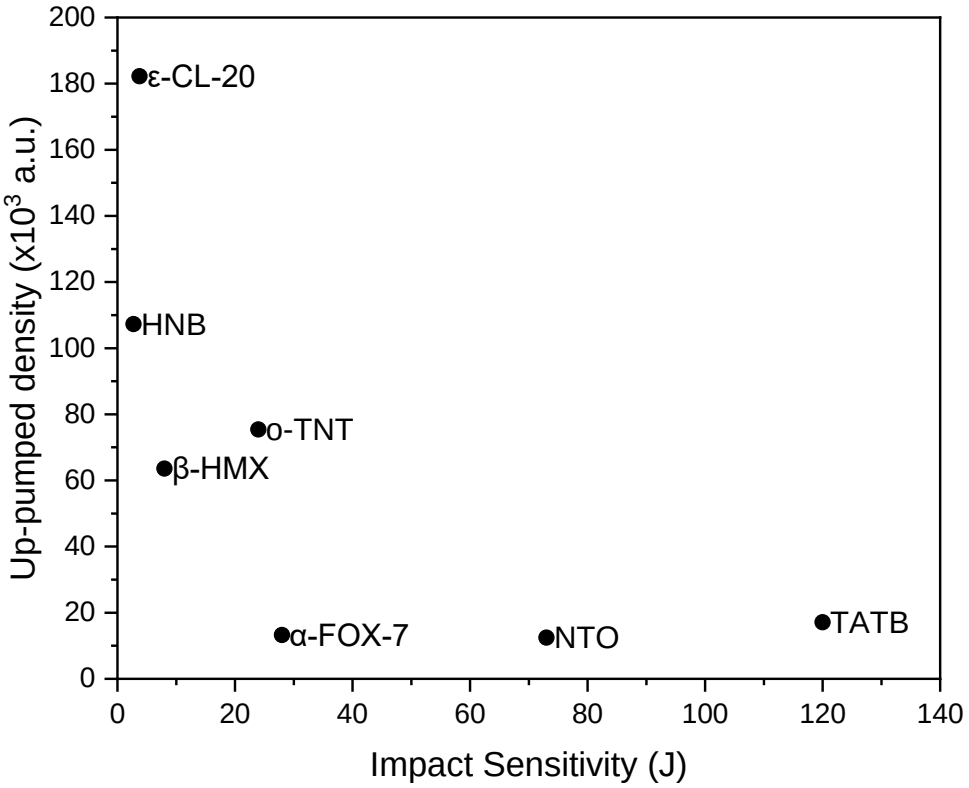

Figure 1.3. Predicted up-pumped density vs. experimental impact sensitivity. Predicted using the up-pumping model. Figure adapted from Michalchuk et. al.[35]

This vibrational up-pumping method has several benefits over other proposed predictive methods. The first is that this model unequivocally takes into account the solid structure of the material. This means that materials which depend upon intermolecular interactions to distinguish from one another, such as multicomponent systems and polymorphs, can be studied. While this method has been shown to work well for the seven materials highlighted in Figure 3, this is still a small data-set and a wider range of materials need to be studied. To that end, the majority of the work presented in this thesis will focus on the application of this new vibrational up-pumping model to investigate the structure-property relationships of EMs with regards to co-crystallisation and polymorphism.

1.3. Co-crystallisation

Co-crystallisation is the process by which two (sometimes more) molecular components are crystallised into a regular arrangement in the solid state and are held together by non-covalent interactions. This is in contrast to a salt, where the multiple components are ionic, and thus held together by electrostatic interactions. Co-crystallisation is commonly used in the pharmaceutical industry to alter drugs to

enable them to have more favourable properties, such as solubility, chemical stability and dissolution rate.[36] Indeed, several drugs are on the market today which are comprised of co-crystals, which highlights the emerging benefit of using co-crystallisation to tailor material properties.[37] The success of co-crystallisation in the pharmaceutical industry has led to the possibility of it being implemented for the design of insensitive EMs.[38] While less commonly used in the energetic community, co-crystallisation of common energetics has still been carried out to great success. One high profile example is the co-crystal of CL-20 and HMX.[39] Both are highly sensitive EMs, in fact CL-20 is too sensitive to be used for military use.[40] CL-20 and HMX were successfully co-crystallised in a 2:1 ratio and the resulting material is reported to have a sensitivity comparable to β-HMX but with a predicted detonation velocity some 100 m s^{-1} higher than β-HMX. This "taming" of CL-20 therefore potentially allows for this high-powered explosive to be used in military settings but with improved safety and handling properties. Additional energetic co-crystals include CL-20-TNT[41] and CL-20-MTNP.[42] This success of tailoring the properties of energetic materials by utilising co-crystallisation opens the door for further studies of co-crystals of energetic materials with the aim to tailor properties and deepen structure-property relationship understanding.

Although the majority of reported energetic co-crystals comprise of two energetic co-formers, EMs can also be co-crystallised with non-energetic components. Indeed, due to the overwhelming presence of (hydrogen bond acceptor) nitro groups in energetic molecules that is often not complemented with suitable hydrogen bond donor groups, crystal design based on hydrogen bonding is difficult when constrained to just energetic molecules. Some known examples are picric acid with 9-bromoanthracene (PIC-BRA)[43] and TNT with naphthalene or 4-aminobenzoic acid.[44] The effect that co-crystallisation with a non-energetic has on the energetic component seems to differ on a case-by-case basis. In the case of the PIC-BRA it was reported that the energetic performance of picric acid was compromised, due to what is essentially dilution of the energetic component with 9-bromoanthracene. Another co-crystal with a non-energetic co-former, of picric acid and 9-vinyalanthracene, reported by Şen *et. al*[45] also reports reduced sensitivity along with reduced detonation parameters as calculated by EXPLO5. Şen also notes that the co-crystal is seen to melt into the corresponding co-former components around the

melting point of 9-vinylanthracene, meaning that only the picric acid component would initiate. Prospective co-formers are selected based on their structure, for instance for their ability to form hydrogen bonds with the other co-former. The formation of these strong non-covalent interactions is thought to ensure the stability of the co-crystal. However, being able to predict how co-formers will interact and crystallise is difficult unless considerable computing power is employed. It is therefore important to understand the driving forces of co-crystallisation formation, as this can be used to understand structure-property relationships with properties such as IS.

1.4 Polymorphism

Polymorphism is the natural phenomenon by which crystal structures of the same material alter due to the difference in crystal packing. Polymorphs of the same material typically have different properties, including melting points, densities, and solubilities, and due to unique molecular packing, the impact sensitivity of EM polymorphs can be expected to differ.[46] Polymorphs can either be stable or metastable at ambient conditions. In addition, polymorphs have been known to be stable only under extreme conditions, such as under high pressure. The high pressure study of EMs is highly important as initiation of EMs often occurs under extreme temperature and pressures, so understanding how EMs behave under such conditions is an important consideration in the development of new safe materials.

During the initiation process, the shock wave pressure may approach 50 GPa and temperatures up to 5500 K.[47] It is therefore important to study the property and behaviours at such conditions. High pressures can be easily achieved in a diamond anvil cell (DAC) for single crystals of material, from which high pressure single crystal X-ray diffraction data to be collected. This has enabled a number of high pressure phase transitions in EMs to be identified, and high pressure structures to be characterised. EMs which have high pressure polymorphs reported include CL-20,[48,49] HMX,[50–52] NTO,[53,54] FOX-7,[55,56] RDX,[57–60] TNT[61] and TATB.[62]

Impact sensitivity testing via the fallhammer test can only consider the polymorphic form of an EM that is expressed at ambient conditions. However, an often overlooked issue is that structural changes can occur during impact testing, such as

a high pressure phase transition. This means that the experimental measurement can be erroneously assigned to the wrong polymorphic form. A recent study by Michalchuck et al showed that the predicted impact sensitivity of FOX-7 varies across the polymorphic series, with the energy required to induce initiation increasing as the layers of molecules in the crystal lattice become flatter.[63] In contrast, impact sensitivity testing, starting from the planar layered γ-FOX-7 reported an identical value to the herringbone α-form. This appeared at odds with the predictions until it was discovered by powder X-ray diffraction that the γ-FOX-7 form had reverted to the α-form at energies just below the initiation threshold. This sets the precedent to look further at the changes in crystal packing has on impact sensitivity.

1.5 Development of a fully computational screening programme

With the development of the vibrational up-pumping model for predicting impact sensitivity, and the already established software of EXPLO-5 which is regularly used to predict the explosive performance of EMs, the precedents needed to develop a fully computational screening programme are tantalisingly close. If the heat of formation of an EM can be calculated from just the structure of an isolated molecule, then the detonation parameters can be predicted. However, to predict impact sensitivity, the crystal structure of the material must be known. This is much harder to predict than the geometry of an isolated molecule. Geometry optimisation of a single molecule, to locate the global energy minimum on its potential energy surface, is a relatively simple task. However, to outright find the energy minimum in relation to a crystal structure is much harder, due to the massively increased number of degrees of freedom of the system. However, serious headway has been made to develop this method of crystal structure prediction (CSP), and as such it is becoming a more reliable computational predictive method.[64] With the increased accuracy of CSP, the potential for a fully computational screening programme can therefore come one step closer.

Aims of this thesis

The development of new EMs relies on understanding the fundamental structure-property relationships of these materials that can be provided by computational modelling. This thesis aims to cover two key steps in the development of a fully computational screening programme for new energetic materials. First, clarity on

how to calculate reliable heats of formation for all forms of EMs (single-component crystals, coordination polymers, co-crystals and salts) is achieved. This is done by understanding the different methods already proposed to predict this important parameter. Second, the newly developed method for predicting impact sensitivity needs to be tested against co-crystals of EMs, and applied to investigate how polymorphism affects this important metric for a number of EMs now known to present multiple polymorphs at pressures and temperatures that are relevant to the initiation pathway. This will also include additional plausible structures predicted by CSP. The thesis will be organised thus:

- In Chapter 2 a short overview of the computational methods applied in this thesis, focusing on their relevance to the work reported in Chapters 3-5, will be presented.
- In Chapter 3, a short review of the methods currently proposed to calculate gas and solid phase heats of formation will be presented, focusing on examples drawn from single-component solids, salts, co-crystals and coordination polymers for which experimental data could be sourced for direct comparison. Robust routes to obtain solid state heats of formation for all compound classes will be presented. In addition, this chapter will also explore the reliability of local mode analysis to quantify the strengths of bonds in energetic molecules.
- In Chapter 4, an investigation into a co-crystal composed of an energetic (Nitrotriazolone, NTO) and a non-energetic (Bipyridine, BIPY) will be presented. This work builds on earlier (experimental only) work within the group to provide the computational modelling component. This includes an investigation to ascertain whether a co-crystal or salt has been produced, and to investigate how the impact sensitivity of the multicomponent crystal compares with pure NTO, alongside an overview on how the energetic performance of NTO has been altered through co-crystallisation with a non-energetic molecule.
- In Chapter 5, a systematic study into how polymorphism can affect impact sensitivity will be presented. This includes two specific examples, 2,4-Dinitroanisole (DNAN) and RDX, which were previously studied experimentally by the group, alongside the polymorphic EM NTO.

- Chapter 6 concludes the thesis, and summarises how the central aims of this research have been met, and suggest further avenues for future study.

References

1 J. P. Agrawal, in *High Energy Materials: Propellants, Explosives and Pyrotechnics*, John Wiley & Sons, Ltd, 2010, pp. 1–67.

2 A. Marshall, *Explosives : Their manufacture, properties, tests and history*, P. Blakiston's Son & Co., Philadelphia, 1915.

3 M. A. Sobrero, Sur plusieurs composes detonants produits avec l'acide nitrique et le sucre, la dextrine, la lactine, la mannite et la glycerine, *Comptes Rendus*, 1847, **24**, 247–248.

4 C. Heaussermann, Über die explosiven Eigenschaften des Trinitrotoluols, *Z. Angew. Chem*, 1891, **4**, 508–511.

5 Peter O. K. Krehl, *History of Shock Waves, Explosions and Impact*, Springer.

6 Q. L. Yan, S. Zeman and A. Elbeih, Recent advances in thermal analysis and stability evaluation of insensitive plastic bonded explosives (PBXs), *Thermochim. Acta*, 2012, **537**, 1–12.

7 D. J. Hewkin, J. A. Hicks, J. Powling and H. Watts, The Combustion of Nitric Ester-Based Propellants: Ballistic Modification by Lead Compounds, *http://dx.doi.org/10.1080/00102207108952257*, 2007, **2**, 307–327.

8 A. P. Denisyuk and L. A. Demidova, Effect of Some Catalysts on Combustion of Double-Base Propellants, *Combust. Explos. Shock Waves 2004 403*, 2004, **40**, 311–318.

9 N. Kubota, T. J. Ohlemiller, L. H. Caveny and M. Summerfield, Site and Mode of Action of Platonizers in Double Base Propellants, *https://doi.org/10.2514/3.49583*, 2012, **12**, 1709–1714.

10 J. W. Fronabarger, M. D. Williams, W. B. Sanborn, J. G. Bragg, D. A. Parrish and M. Bichay, DBX-1 – A Lead Free Replacement for Lead Azide, *Propellants, Explos. Pyrotech.*, 2011, **36**, 541–550.

11 L. R. Warren, C. R. Pulham and C. A. Morrison, Towards understanding the catalytic properties of lead-based ballistic modifiers in double base propellants, *Phys. Chem. Chem. Phys.*, 2020, **22**, 25502–25513.

12 L. R. Warren, Z. Wang, C. R. Pulham and C. A. Morrison, A Review of the

Catalytic Effects of Lead-Based Ballistic Modifiers on the Combustion Chemistry of Double Base Propellants, *Propellants, Explos. Pyrotech.*, 2021, **46**, 13–25.

13 K.-S. Ju and R. E. Parales, Nitroaromatic Compounds, from Synthesis to Biodegradation, *Microbiol. Mol. Biol. Rev.*, 2010, **74**, 250–272.

14 P. Kovacic and R. Somanathan, Nitroaromatic compounds: Environmental toxicity, carcinogenicity, mutagenicity, therapy and mechanism, , DOI:10.1002/jat.2980.

15 D. R. S. Lima, M. L. S. Bezerra, E. B. Neves and F. R. Moreira, Impact of ammunition and military explosives on human health and the environment, *Rev. Environ. Health*, 2011, **26**, 101–110.

16 G. Sliwoski, S. Kothiwale, J. Meiler and E. W. Lowe, Computational Methods in Drug Discovery, *Pharmacol. Rev.*, 2014, **66**, 334.

17 X. Lin, X. Li and X. Lin, A Review on Applications of Computational Methods in Drug Screening and Design, *Molecules*, , DOI:10.3390/MOLECULES25061375.

18 W. C. Lothrop and G. Richard Handrick, The Relationship Between Performance and Consitution of Pure Organic Explosive Compounds., *Chem. Rev*, 1949, **44**, 419–445.

19 M. J. Kamlet and H. G. Adolph, The relationship of Impact Sensitivity with Structure of Organic High Explosives. II. Polynitroaromatic explosives, *Propellants, Explos. Pyrotech.*, 1979, **4**, 30–34.

20 B. M. Rice and E. F. C. Byrd, Relationships with oxygen balance and bond dissociation energies, 2022, 67–79.

21 L. Fried and P. Souers, 1994.

22 M. Suceska, in *Proc. of 32nd International Annual Conference of ICT, Karlsruhe, Germany, 2001*, OZM Research, Pardubice, 2001, pp. 110/1-110/13.

23 F. P. Bowden and A. Yoffe, Hot spots and the initiation of explosion, *Symp.*

Combust. Flame, Explos. Phenom., 1948, **3**, 551–560.

24 P. Politzer and J. S. Murray, Relationships between dissociation energies and electrostatic potentials of C-NO2 bonds: Applications to impact sensitivities, *J. Mol. Struct.*, 1996, **376**, 419–424.

25 J. S. Murray, P. Lane and P. Politzer, Relationships between impact sensitivities and molecular surface electrostatic potentials of nitroaromatic and nitroheterocyclic molecules, *Mol. Phys.*, 1995, **85**, 1–8.

26 P. Politzer and J. S. Murray, Are HOMO–LUMO gaps reliable indicators of explosive impact sensitivity?, *J. Mol. Model.*, 2021, **27**, 1–6.

27 S. V. Bondarchuk, Quantification of Impact Sensitivity Based on Solid-State Derived Criteria, *J. Phys. Chem. A*, 2018, **122**, 5455–5463.

28 A. A. L. Michalchuk, S. Rudić, C. R. Pulham and C. A. Morrison, Vibrationally induced metallisation of the energetic azide α-NaN3, *Phys. Chem. Chem. Phys.*, 2018, **20**, 29061–29069.

29 W. Zhu and H. Xiao, First-principles band gap criterion for impact sensitivity of energetic crystals: A review, *Struct. Chem.*, 2010, **21**, 657–665.

30 C. S. Coffey and E. T. Toton, A microscopic theory of compressive wave-induced reactions in solid explosives, *J. Chem. Phys.*, 1982, **76**, 949–954.

31 F. J. Zerilli and E. T. Toton, Shock-induced molecular excitation in solids.

32 D. D. Dlott and M. D. Fayer, Shocked molecular solids: Vibrational up pumping, defect hot spot formation, and the onset of chemistry, *J. Chem. Phys.*, 1990, **92**, 3798–3812.

33 J. Bernstein, Ab initio study of energy transfer rates and impact sensitivities of crystalline explosives, *J. Chem. Phys.*, 2018, **148**, 084502.

34 A. A. L. Michalchuk, M. Trestman, S. Rudić, P. Portius, P. T. Fincham, C. R. Pulham and C. A. Morrison, Predicting the reactivity of energetic materials: An: ab initio multi-phonon approach, *J. Mater. Chem. A*, 2019, **7**, 19539–19553.

35 A. A. L. Michalchuk, J. Hemingway and C. A. Morrison, Predicting the impact sensitivities of energetic materials through zone-center phonon up-pumping, *J.*

Chem. Phys., 2021, **154**, 1–11.

36 N. Qiao, M. Li, W. Schlindwein, N. Malek, A. Davies and G. Trappitt, Pharmaceutical cocrystals: An overview, *Int. J. Pharm.*, 2011, **419**, 1–11.

37 O. N. Kavanagh, D. M. Croker, G. M. Walker and M. J. Zaworotko, Pharmaceutical cocrystals: from serendipity to design to application, *Drug Discov. Today*, 2019, **24**, 796–804.

38 S. R. Kennedy and C. R. Pulham, in *Co-crystals: Preparation, Characterization and Applications Edited*, eds. B. Aakeroy and A. Sinha, The Royal Society of Chemistry, 2018, pp. 231–264.

39 O. Bolton, L. R. Simke, P. F. Pagoria and A. J. Matzger, High power explosive with good sensitivity: A 2:1 cocrystal of CL-20:HMX, *Cryst. Growth Des.*, 2012, **12**, 4311–4314.

40 R. L. Simpson, P. A. Urtiew, D. L. Ornellas, G. L. Moody, K. J. Scribner and D. M. Hoffman, CL-20 performance exceeds that of HMX and its sensitivity is moderate, *Propellants, Explos. Pyrotech.*, 1997, **22**, 249–255.

41 O. Bolton and A. J. Matzger, Improved Stability and Smart-Material Functionality Realized in an Energetic Cocrystal, *Angew. Chemie Int. Ed.*, 2011, **50**, 8960–8963.

42 Q. Ma, T. Jiang, Y. Chi, Y. Chen, J. Wang, J. Huang and F. Nie, A novel multi-nitrogen 2,4,6,8,10,12-hexanitrohexaazaisowurtzitane-based energetic co-crystal with 1-methyl-3,4,5-trinitropyrazole as a donor: experimental and theoretical investigations of intermolecular interactions, *New J. Chem.*, 2017, **41**, 4165–4172.

43 S. I. Bozkuş, K. S. Hope, B. Yüksel, N. Atçeken, H. Nazır, O. Atakol and N. Şen, Characterization and properties of a novel energetic Co-crystal formed between 2,4,6-Trinitrophenol and 9-Bromoanthracene, *J. Mol. Struct.*, 2019, **1192**, 145–153.

44 K. B. Landenberger and A. J. Matzger, Cocrystal Engineering of a Prototype Energetic Material: Supramolecular Chemistry of 2,4,6-Trinitrotoluene, 2010, **10**, 5341–5347.

45 N. Şen, H. Dursun, K. S. Hope, H. Nazir, N. Acar and O. Atakol, Towards low-impact-sensitivity through crystal engineering: New energetic co-crystals formed between Picric acid, Trinitrotoluene and 9-Vinylanthracene, *J. Mol. Struct.*, 2020, **1219**, 128614.

46 R. Bu, H. Li and C. Zhang, Polymorphic Transition in Traditional Energetic Materials: Influencing Factors and Effects on Structure, Property, and Performance, *Cryst. Growth Des.*, 2020, **20**, 3561–3576.

47 Ya.B. Zel'dovich and Yu.P. Raizer, *Physics of shock waves and high-temperature hydrodynamic phenomena*, Academic Press, 1967.

48 A. T. Nielsen, A. P. Chafin, S. L. Christian, D. W. Moore, M. P. Nadler, R. A. Nissan, D. J. Vanderah, R. D. Gilardi, C. F. George and J. L. Flippen-Anderson, Synthesis of polyazapolycyclic caged polynitramines, *Tetrahedron*, 1998, **54**, 11793–11812.

49 D. I. A. Millar, H. E. Maynard-Casely, A. K. Kleppe, W. G. Marshall, C. R. Pulham and A. S. Cumming, Putting the squeeze on energetic materials—structural characterisation of a high-pressure phase of CL-20, *CrystEngComm*, 2010, **12**, 2524–2527.

50 H. H. Cady, A. C. Larson, D. T. Cromer and IUCr, The crystal structure of α-HMX and a refinement of the structure of β-HMX, *Acta Crystallogr.*, 1963, **16**, 617–623.

51 R. E. Cobbledick and R. W. H. Small, The crystal structure of the δ-form of 1,3,5,7-tetranitro-1,3,5,7-tetraazacyclooctane (δ-HMX), *Acta Crystallogr. Sect. B Struct. Crystallogr. Cryst. Chem.*, 1974, **30**, 1918–1922.

52 B. L. Korsunskii, S. M. Aldoshin, S. A. Vozchikova, N. I. Golovina, N. V. Chukanov and G. V. Shilov, A new crystalline HMX polymorph: ε-HMX, *Russ. J. Phys. Chem. B 2010 46*, 2011, **4**, 934–941.

53 N. Bolotina, K. Kirschbaum and A. A. Pinkerton, Structural Science Energetic materials: a-NTO crystallizes as a four-component triclinic twin, *Acta Cryst*, 2005, **61**, 577–584.

54 N. B. Bolotina, E. A. Zhurova and A. A. Pinkerton, Energetic materials:

variable-temperature crystal structure of b-NTO, *J. Appl. Crystallogr.*, 2003, **36**, 280–295.

55 J. Evers, T. M. Klapötke, P. Mayer, G. Oehlinger and J. Welch, α- and β-FOX-7, polymorphs of a high energy density material, studied by X-ray single crystal and powder investigations in the temperature range from 200 to 423 K, *Inorg. Chem.*, 2006, **45**, 4996–5007.

56 M. J. Crawford, J. Evers, M. Göbel, T. M. Klapötke, P. Mayer, G. Oehlinger and J. M. Welch, γ-FOX-7: Structure of a High Energy Density Material Immediately Prior to Decomposition, *Propellants, Explos. Pyrotech.*, 2007, **32**, 478–495.

57 C. S. Choi and E. Prince, The crystal structure of cyclotrimethylenetrinitramine, *Acta Crystallogr. Sect. B Struct. Crystallogr. Cryst. Chem.*, 1972, **28**, 2857–2862.

58 D. I. A. Millar, I. D. H. Oswald, D. J. Francis, W. G. Marshall, C. R. Pulham and A. S. Cumming, The crystal structure of β-RDX—an elusive form of an explosive revealed, *Chem. Commun.*, 2009, **5**, 562–564.

59 A. J. Davidson, I. D. H. Oswald, D. J. Francis, A. R. Lennie, W. G. Marshall, D. I. A. Millar, C. R. Pulham, J. E. Warren and A. S. Cumming, Explosives under pressure—the crystal structure of γ-RDX as determined by high-pressure X-ray and neutron diffraction, *CrystEngComm*, 2008, **10**, 162–165.

60 D. I. A. Millar, I. D. H. Oswald, C. Barry, D. J. Francis, W. G. Marshall, C. R. Pulham and A. S. Cumming, Pressure-cooking of explosives—the crystal structure of ε-RDX as determined by X-ray and neutron diffraction, *Chem. Commun.*, 2010, **46**, 5662–5664.

61 R. M. Vrcelj, J. N. Sherwood, A. R. Kennedy, H. G. Gallagher and T. Gelbrich, Polymorphism in 2-4-6 Trinitrotoluene, *Cryst. Growth Des.*, 2003, **3**, 1027–1032.

62 B. A. Steele, S. M. Clarke and M. P. Kroonblawd, Pressure-induced phase transition in 1,3,5- triamino-2,4,6-trinitrobenzene (TATB), *Appl. Phys. Lett*, 2019, **114**, 191901.

63 A. A. L. Michalchuk, S. Rudić, C. R. Pulham and C. A. Morrison, Predicting the impact sensitivity of a polymorphic high explosive: the curious case of FOX-7, *Chem. Commun.*, 2021, **57**, 11213–11216.

64 S. M. Woodley, G. M. Day and R. Catlow, Structure prediction of crystals, surfaces and nanoparticles, *Philos. Trans. R. Soc. A*, 2020, **378**, 20190600.

Chapter 2

Computational Methods

This chapter will provide an overview of the computational methods used throughout this thesis. Computational modelling has been carried out on a wide range of systems, to study many different properties. For this reason, a wide range of computational methods have been used to investigate these properties. In Chapter 3, the focus is on isolated molecule calculations while in Chapters 4 and 5, solid state calculations are required in combination with a vibrational up-pumping model. Initially the theoretical background of first principles calculations will be described, highlighting the specific modelling software that will be used. The theory described here is based on work written in books by Meitzel, Rankin and Morrison[1]; Sholl and Steckel;[2] Lewars[3] where more in depth discussions can be found.

2.1 *Ab initio* methods

Ab initio, literally “from the start”, computational methods are ones that aim to solve the Schrodinger equation (Equation 2.1) given the input geometry of a system.

$$\hat{H}\psi = \frac{-\hbar}{2m_e}\nabla^2\psi + V\psi = E\psi \qquad (2.1)$$

The Hamiltonian operator, $\hat{H}$, describes the energy of the system, that is the sum of the kinetic ($\frac{\hbar}{2m_e}\nabla^2$) and potential energies (V). For the kinetic energy term, $\hbar$ is the reduced Planck constant, m_e is the mass of an electron and ∇^2 is the Laplacian operator. The potential energy term is made up of three terms, nuclei-nuclei, electron-electron, and nuclei-electron interactions. The wavefunction, denoted by ψ, describes the motion of the electrons of the system. Obtaining exact solutions to the Schrodinger Equation for a 1 electron system is a simple, but beyond this electron-electron interactions induce a many-body problem which makes the equation impossible to solve. Therefore, only approximate solutions can be made for systems beyond 1-electron systems. Several approximations are required, which will be described below.

2.1.1. Hamiltonian operator, $\widehat{H}$

The first approximation which can be made to model the Hamiltonian is the Born-Oppenheimer (BO) approximation.[4] Here the motion of electrons is magnitudes faster than the motion of an atomic nuclei. Therefore, nuclei are simply considered as positively charged point charges. This results in the nuclear kinetic energy term disappearing and the nuclear-nuclear electrostatic interaction can be calculated using Coulomb's law. While the BO approximation simplifies two of the terms in the Hamiltonian operator, the potential energy terms involving electrons are yet to be accounted for. Therefore, a number of other approximations have been developed to deal with the many body problem.

Hartree-Fock theory

Hartree-Fock theory is the simplest approximation. Initially, the Hartree method proposed electrons formed a spherically symmetric field around the nucleus.[5] This was used to approximate the electron-electron correlation induced potential of an atom. However, the resulting wavefunction is not antisymmetric, meaning that electron exchange (the pairing of opposite spins) is not modelled. The introduction of a Slater determinant by Fock[6] satisfies the antisymmetric properties of the solution (in that when two electrons of the same spin are placed in the same space the wavefunction collapses to 0) and improved this method further. Combining these two methods provides Hartree-Fock (HF) theory which allows for exact calculation of electron exchange. Electron correlation, the measure of how much the movement of one electron is influenced by all other electrons is simply ignored in HF theory. However, the HF approximation is disadvantageous if a system is being modelled which has areas of high electron density, such as double bonds. Therefore, post Hartree-Fock methods have been developed to overcome this shortfall.

Density Functional Theory

Density Functional Theory (DFT) is a different approach to dealing with the many-body problem. With DFT, the properties of the system can be determined from functionals of the electron density of the system. However, the exact functionals for exchange and correlation are not known so a number of functionals (often called xc functionals) based on different approximations have been made. Hybrid DFT functionals are the product of the combination of Hartree-Fock and DFT. This combines the best of both theories: the electron-electron correlation is approximated

as it is with DFT, while electron-electron exchange is exactly modelled as it is with HF theory. Hybrid DFT therefore provides an alternative which has a high accuracy but with a far lower computational cost. The majority of the work presented in this thesis uses DFT.

Exchange-Correlation Functionals

The most basic exchange-correlation functional is one that assumes the electron density is a uniform electron gas. Therefore, at a point *r* with density ρ(*r*), the exchange correlation will be the same as that of a uniform gas with the same density. This approximation is called the Local Density Approximation (LDA) and works well for solid metals, as the electron density is almost uniform in these systems. However, the approximation does not work as well in molecular solids.

An improved xc functional which works well for molecular solids the Generalised Gradient Approximation (GGA), which is dependant not just on the electron density (as it is in LDA) but also on the gradient of the electron density. This allows for better modelling of molecular systems which consist of areas of high electron density around atoms and the low electron density in the void space between molecules.

There is one drawback to the use of GGA functionals, that is that they are inherently local and do therefore not account for long range interactions which result in van der Waals interactions. These long range interactions are crucial to describing the interactions which can often dominate molecular crystals. Therefore, many semi-empirical and empirical corrections have been developed. The two most notable are the Grimme and Tkatchenko-Scheffler (TS).[7]

Throughout this thesis different models are used:

- Isolated molecules: The Becke, 3-parameter, Lee-Yang-Parr (B3LYP)[8] hybrid functional has been used. This is obtained by adding gradient corrections to LDA, exchange functions from Becke and correlation functions of Lee, Yang and Parr. This has been shown to work consistently well for organic molecules in terms of compromise between computational cost and accuracy of results.[9]
- Crystalline structures: Perdew-Burke-Ernzerhof (PBE) functional[10] has been used with CASTEP. This is a GGA functional, which provides good agreement

with experimental data when used in conjunction with the TS dispersion correction scheme. For calculations performed in CRYSTAL (see below) the HSE06 hybrid functional has been used.[11,12] HSE06 has been shown to perform well for the calculation of bandgaps in semiconductors.[13]

2.1.2. Wavefunction, $\boldsymbol{\psi}$

After the Hamiltonian the next part of the Schrodinger equation to consider is the wavefunction, ψ, as mentioned describes motion of the electrons in the system. Atomic wavefunctions are constructed to mimic the atomic radial distribution functions. These are approximately Gaussian shaped, so the most common way to model the atomic radial function is a summation of Gaussian functions. This collection of Gaussian functions is called the basis set. A larger number of functions should lead to a more accurate depiction of the real system's wavefunction, however the calculation will require more resources

In an isolated molecule system, the traditional way to think about electrons in atoms is through their atomic orbitals. Using the rules of molecular orbital theory, molecular orbitals for a molecule can be constructed *via* linear combination of atomic orbitals. This localised basis set is used for modelling isolated molecules in the Gaussian16 software package.[14] Two parts of the model need to be considered, as described above. First, the method which described the Hamiltonian operator must be chosen. For all calculations in this thesis, the hybrid DFT functionals have been used, specifically the split-valence basis sets have been used. Typically represented in the form X-YZg, where X describes the number of Gaussian functions describing the core atomic orbitals, while Y and Z describe the number of valence functions. The two numbers show that the valence orbitals are consisted of two basis functionals each. Additional terms can be added to the basis set, diffuse functionals (denoted by +) and polarisation functions (denoted by *). Polarisation functions allow for additional tailing on the Gaussian functionals, therefore allowing for more accurate modelling of polarised chemical bonds. The basis set used most for isolated molecules in this work is the 6-31G*, as most structures contain only C, H, N and O atoms.

2.2. Solid state calculations

Within this thesis the most common method for describing the wavefunction in solid systems is through a plane wave basis set. According to Bloch's theorem, solutions

to the Schrodinger equation in a periodic system take the form of plane waves modulated by a periodic function. Electrons are considered as waves which extend through the solid state system. These are also called delocalised basis sets, as the behaviour of the electrons is not dictated by the localised atomic orbital but by the construction of the solid system. Electrons in this instance are thought of as a summation of waves of varying wavelengths representing electrons of varying energies in the system. Increasing the cut off energy of the plane waves used provides a better quality basis sets as this provides a better representation of the real electrons in a system, but this does come with increased computational cost. The software CASTEP[15] which is used extensively in this thesis allows for the implementation of delocalised basis sets. A suitable cut off energy for the plane wave basis set can be determined from convergence testing. Carrying out single point energy calculations at increasing cut off energies allows for a reasonable cut off energy to be selected, when the convergence of the energy is below 0.02 eV/atom.

The use of plane-wave basis sets does propose an issue, it is possible for the valence and core electrons to interact during the simulation. Modelling all electrons in a system also increases the computational cost of the calculation. To combat these two issues pseudopotentials are used. Pseudopotentials model the core electrons in atoms as frozen, that is, these electrons are not involved in bonding. This is an accurate assumption, as valence electrons interact far more than core electron. The set of pseudopotentials which allow for the cut-off energy of the basis set to be at its lowest possible value are ultra-soft pseudopotentials, however these come with the caveat of having the largest possible radius on the pseudopotentials and so come with a diminishing quality of the calculation. Norm-conserving pseudopotentials offer more accurate representation of the scattering of ions and are better implemented into DFT and density functional perturbation theory (see below), which are used extensively in this thesis. Therefore, norm-conserving pseudopotentials are used throughout this work, using the 00PBE_OP pseudopotentials available in the CASTEP library.

Localised basis sets can also be used in solid state modelling. For specific applications it is advantageous to use localised basis sets in crystalline systems, as the package CRYSTAL does.[16] In this case, each crystalline orbital is constructed from a linear combination of Bloch functions, defined in terms of atomic orbitals. This

method relies heavily on the symmetry of the system to reduce computational cost as much as possible. The electron density of a system can be better modelled using localised basis sets, therefore in applications where the electronic structure of a system needs to be determined, localised basis sets are the preferred option, and thus are used in this work to calculate band structures.

Implementation of a localised basis set or delocalised basis set is dependent upon what properties are desired. Plane wave basis sets are advantageous as they are faster to run, and the plane wave basis sets are not dependent upon the type of atoms present in a system, so the same model chemistry can be applied to different systems.

Geometry Optimisation

The first step in an *ab initio* calculation is geometry optimisation, which allows for the minimum energy structure to be found. Following the determination of this lowest energy structure, further properties can be calculated. The initial structural input can either be constructed in a model builder, the typical case when dealing with isolated molecule calculations, or from an experimentally determined crystal structure, as is typical for solid state calculations.

Geometry optimisation relies on a self-consistent field (SCF) method which is an iterative method by which an initial wavefunction is used to solve the Schrödinger equation. The forces on the atoms are then calculated, by calculating the gradient of the potential energy surface (thus being at a minima the forces acting on atoms would be zero). Atoms are then moved, and the process is repeated. Geometry optimisation is considered converged when the change in forces on atoms between cycles is close to zero and when atomic displacements are also close to zero.

Of course, a starting geometry closest in energy to the minimum energy structure is desirable to avoid the instance of calculating a structure at a stationary point represented by a transition state or a local minimum. At a stationary point on the potential energy surface, the gradient of the potential energy surface is also zero, and once this state is achieved, geometry optimisation is completed, however it will not represent the global minimum. It is possible to check the curvature of the potential energy surface, i.e. to calculate the second derivative of the PES with respect to atomic positions. This calculation is called a vibrational frequency

calculation. It is important that before carrying out a vibrational frequency calculation that the geometry optimisation is carried out with tight convergence criteria, to ensure a global minimum structure is obtained.

Vibrational frequency calculation

Although a vibrational frequency calculation can simply be used to check if a geometry optimised structure is at the global minimum of the potential energy surface, much more valuable physical properties are obtained which are related to the vibrational spectrum, including infra-red and Raman spectra. The force constant matrix which is generated during a vibrational frequency calculation is required for local mode force constant analysis (LModeA described in Section 2.4). Vibrational spectra of solid structures will be used as the basis for the vibrational up-pumping model used to predict the relative impact sensitivity of EMs also described in Section 2.4.

To understand the implications of vibrational spectra, a brief introduction to the workings behind lattice dynamic calculations must be explained. Most work done when calculating vibrational frequencies is the construction of a Hessian matrix. A Hessian matrix is a square matrix of second-order partial derivatives, which describes the local curvature of a function of many variables. That is, it describes the curvature of the potential energy surface's energy with respect to geometry.

When a geometry is at a global minimum, this will mean that the force constants (that is the curvature of the PES) will be positive- changing the geometry in any such way will result in the energy of the system increasing. This means that if the geometry is representative of a higher order stationary point (such as a transition state) then in more than one dimension the curvature of the PES will be negative. This will be represented in a vibrational frequency calculation by negative, or imaginary frequencies. Therefore, the optimised geometry will not be representative of the global minimum of the potential energy surface. Therefore, a quality geometry optimisation is required before hand, especially in solid structures where there are more degrees of freedom.

In solid structures this is often called a lattice dynamics calculation. There are two methods to calculate, density functional perturbation theory (DFPT)[17] and finite displacement approach. DFPT calculates the dynamical matrix on multiple wave

vectors, and is interpolated over the Brillouin Zone, whereas the finite displacement method generates a supercell to capture these modes. When working with larger unit cells, as is often the case with the systems studied in this thesis, the use of finite displacement therefore increases the computational cost. Therefore, DFPT is used exclusively in this thesis.

2.3. Semi empirical methods

Semi-empirical methods are different from *ab initio* methods in that some parameters and approximations used are obtained from empirical data. Semi-empirical methods were first developed in the late twentieth century to deal with the lower computing power of the day, which limited the applications of *ab initio* methods to smaller molecules. While semi-empirical methods were attractive due their comparative speed, because of the reliance on empirical data to build the methods, results are only as good as the data used. Even considering the vast increase in computational power from when semi-empirical methods were first developed to the modern day, semi-empirical methods are still a frequently used tool, as they can still be used on much shorter timescales than *ab initio* methods. Within this thesis, the semi-empirical quantum mechanical method, PM7, is used to calculate the heats of formation of energetic molecules, and is compared extensively to other methods. While it s accuracy at calculating heats of formation for energetic molecules is discussed in further detail in Chapter 3, a brief introduction to the PM7 method is presented here.

The PM7 method is the third in the PM family after the introduction of PM3 in 1989[18] and PM6 in 2007.[19] All three methods fall under the Neglect of Diatomic Differential Overlap (NDDO) methods umbrella. These are considered the gold standard in semi-empirical methods. Similar to ab initio methods, semi-empirical methods use an algorithm to find the first and second derivatives of energy with respect to geometry to carry out geometry optimisation. However, particularly the PM*X* methods are parameterised to produce high quality parameters of geometry and heats of formation. Its semi-empirical nature comes from several types of reference data being used in parameter optimisation.

The method for calculating heats of formation from a semi-empirical method is as follows. The total internal energy of the molecule except for zero point vibrational

energy is used to calculate the heat of formation of the molecule. This is shown in the scheme Figure 2.1.

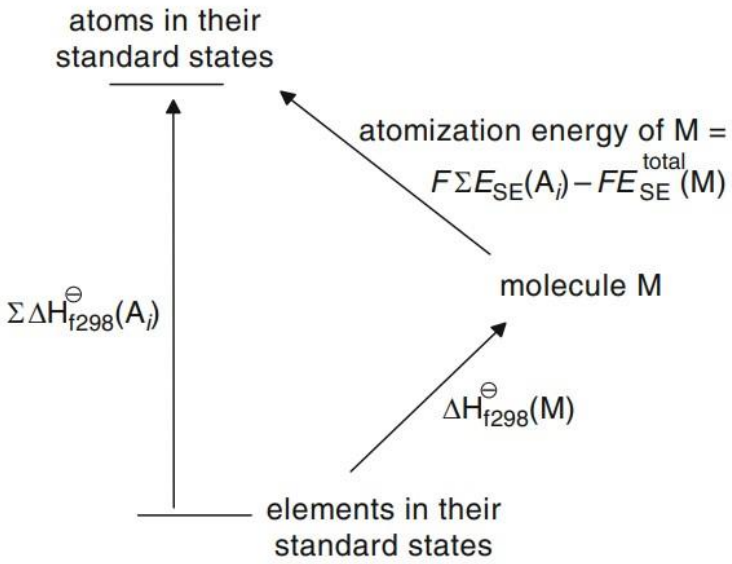

Figure 2.1 The method for calculating the heats of formation of a molecule using semi-empirical methods. Figure adapted from E. Lewars.[20]

- $\Sigma\Delta H_{f298}$ (A_i) is the sum, over all atoms A in the molecule, M, of the experimental 298 K heats of formation of the atoms
- ΔH_{f298} (M) is the 298 K heat of formation of M, which is the quantity needed.
- The atomisation energy of M, the energy of the atoms minus the energy of M. E_{SE}^{total} (M) is the energy of the molecule following optimisation. Where F converts the energy from Hartrees to kJ mol^{-1}.

Of course, this method could be carried out using a fully *ab initio* method, but the semi-empirical method is parameterised to ensure that a zero point energy (ZPE) correction does not need to be calculated.

Semi-empirical methods rely on the parameterisation of experimental quantities against calculated values to build an accurate model. Therefore, the quality of the data can affect the quality of the semi-empirical method. For PM3 100 reference data were used in its parameterisation. For PM6, over 9000 reference data were used. For PM7 the wealth of the CSD and ICSD was used to parameterise with regards to molecular structure, while thermochemical data, such as heats of formation, were obtained from large collections of data including JANAF, NIST online WebBook and

Lange's handbook. This large wealth of data used to parameterise PM7 results in the average unsigned errors (AUE) in the heats of formation by PM7 have decreased by 50 % relative to the previous PM6. Additionally, PM7 can be used for atoms H-La and Lu-Bi. The accuracy and the range over which the PM7 method can be used, in combination with its parameterisation with respect to heats of formation is the reason for its use in this work, compared to other semi-empirical methods.

PIXEL

PIXEL is a computer package which is used for modelling the intermolecular interactions in molecular crystal structures. This software is used to calculate the lattice energies in solid structures – something which is required in Chapter 3.

PIXEL works by first carrying out an *ab initio* molecular orbital calculation on the asymmetric unit of the crystal structure.[21,22] This generates the molecular electron density of the system. This, along with the nuclear density, is then divided into small cubic volumes, or 'pixels'. The four intermolecular interactions between each pixel pair is then calculated. The four intermolecular interactions being:

- Electrostatic: The attractive forces of opposite charges and the repulsive forces of like charges.
- Polarisation: The stabilising distortion of a cloud of electron density when a point charge approaches.
- Dispersion: The instantaneous fluctuations in electron density which cause instantaneous atomic and molecular dipoles. This causes further deformation in electron density in neighbouring molecules.
- Repulsion: The repulsion of the electrons when two atoms or molecules approach one another.

Each of the four intermolecular interactions is calculated for pairs of pixels from each molecule and summing the values. This is then expanded to the molecules in a set radius around the central asymmetric unit, the position of the molecules determined by the space group of the material. This radius is set to 18 Å, which is shown to be a good radius for organic molecular crystals. PIXEL was implemented using the python API MrPIXEL[23] in the Cambridge Structural Database, which automates the set up of PIXEL calculations from Mercury.

2.4. Specialised software used for modelling energetic materials

Local Mode Vibrational Analysis - LModeA.

One aspect of materials design which is important to the field of EMs is the strength of chemical bonds. As discussed above, the population of the vibrational modes which pertain to bond stretching can lead to the decomposition of the material. Knowing which chemical bonds are weak can be valuable when designing new EMs. The force constant of a chemical bond directly correlates with the bond strength, and force constants are routinely calculated during a geometry optimisation as the second derivate (that is, the curvature) of the potential energy surface provides the force constant of the motion. Thus, it would seem simple to obtain the force constants from a geometry optimisation. The software used to obtain these force constants of LModeA (Local Mode Analysis) which calculates the local mode force constants.[24–26] This is remarkably useful as previously only normal modes of vibration could be analysed, which compose of mixed molecular motion. While this software is not developed solely for use with energetic materials, its usefulness when it comes to aiding molecular design cannot be underestimated.

For a (non-linear) molecule with N atoms, there are 3N-6 normal modes of vibration. These modes of vibration are typically a combination of bond stretches, angle bends and dihedral motion. Therefore, calculating the force constants of these vibrational modes will not provide any information on the force constants of individual atoms. LModeA works by mass-decoupling the normal modes of vibration (as the number of normal modes of vibration map 1:1 onto the local modes of vibration) and therefore the force constants for the local modes of vibration can be extracted and used to evaluate the strengths of the bonds. The importance of the mass-decoupled nature of LModeA is that force constants calculated for different chemical bonds can be directly compared. LModeA can be implemented in a gas phase structure, following geometry optimisation and a vibrational frequency calculation. Implementation for solid-state structures is done using LModeA-nano.[27]

EXPLO5

EXPLO5 is a valuable piece of software used to evaluate the performance of an EM. It is used to solve thermodynamic equations between reaction products to find equilibrium composition.[28–30] Ideal detonation is assumed, with the calculation of the equilibrium composition and thermodynamic parameters of state of detonation

products along the shock adiabat of detonation products. The Chapman-Jouguet (C-J) point is calculated, which is the point at which the detonation wave travels at a velocity at which reacting gases just reach sonic velocity as the reaction ceases, and thus the detonation parameters are calculated.

To understand how EXPLO-5 calculates the detonation parameters, some background to the mechanism assumed during detonation should be considered. Detonation is defined as the supersonic propagation of chemical reactions through a material. The shock wave is what propagates through the material, this causes the compression of a thin layer of the material from the initial volume, V_0 (= $1/\rho_0$) where ρ_0 is the initial density, to V_1 in accordance with the shock adiabat for a given explosive. Due to compression of the material, the pressure increases from p_0 to p_1 this results in an increase in the temperature in the compressed explosive layer, which results in the initiation of the chemical reactions. When the chemical reactions are at their end, the volume and pressure of the reaction products reaches V_2 and p_2. This corresponds to a point on the shock adiabat for detonation products, which according to the steady-state model of detonation lies on a straight line with the points (V_0,p_0) and (V_1,p_1). This straight line is called the Rayleigh line. (Figure 2.2)

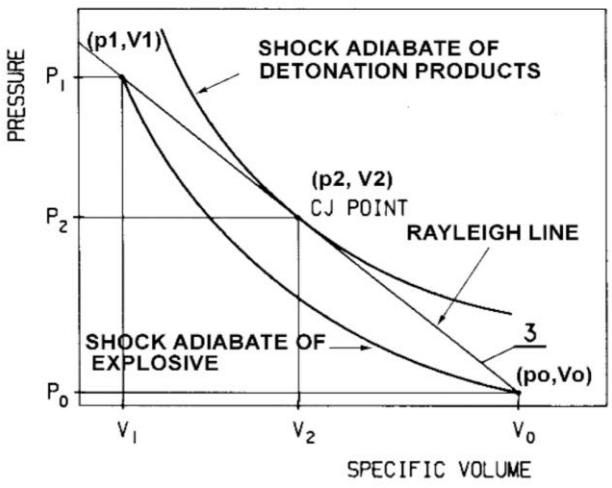

Figure 2.2. A schematic of a shock adiabat which is used to determine the C-J point in EXPLO-5. Image from Sućeska.[30]

EXPLO5 was used with the Becker-Kistiakowsky-Wilson equation of state (BKW-EOS) for gaseous products, which has been shown to accurately predict the detonation parameters for explosives with densities above 1 g cm^{-3}.[31] While the Cowan-Fickett equation of state was used for solid carbon. The C-J point was

determined, and the detonation parameters are calculated at this point, which is the shock adiabat's first derivative.

The enthalpy of formation and the chemical composition are used to estimate the detonation products, while the density is used to determine the shock adiabat. The BKW-EOS is then used, along with known thermodynamic relationships to determine the detonation parameters, including detonation temperature and detonation pressure and velocity.

An EOS is an equation which relates the pressure, volume, temperature and composition of a "fluid" system. The EOS takes the composition and predicts the phase and volumetric behaviour of the system over a wide range of pressures and temperatures. In EXPLO5, the BKW EOS calculates the composition at the C-J point. The C-J point is a point on the shock adiabat of detonation products at which the detonation velocity has its minimum value. Detonation products are also calculated.

VUP.PY

This work extensively uses a model based on a vibrational up-pumping method to predict the impact sensitivity of EMs. The term "phonon" to help describe the model chemistry used. In its simplest definition, a phonon is a discrete quantum of vibration, and is used as a descriptor for the excitation of atoms and molecules in a solid state structure. A simple background theory of the process: initial mechanical energy is believed to propagate through the external vibrations of a crystal and excite the local modes, resulting in the activation of trigger linkages, leading to bond breaking and initiation. Therefore, the up-pumping models this mechanism and determines the relative ease at which the initial mechanical energy can excite the local modes of vibration for an EM. A visual schematic for how the vibrational up-pumping model is used to predict impact sensitivity is shown in Figure 2.3.

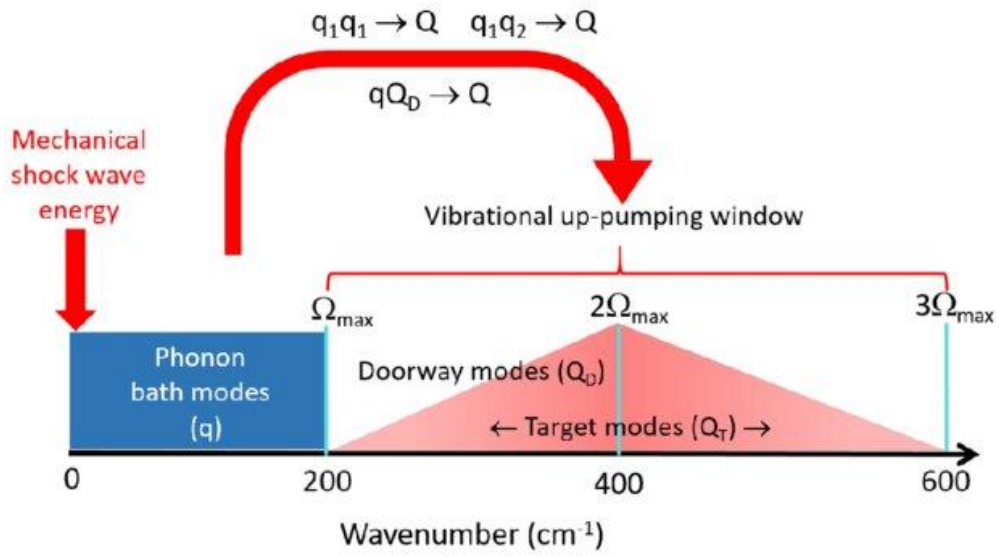

Figure 2.3. A simplified schematic of the vibrational up-pumping process. Red triangle representing the generated 2PhonDoS.

The vibrational up-pumping code as implemented through Python (VUP.PY) is the model that is used to first model how vibrational energy can be transferred through a solid structure, and then to predict the relative sensitivity of an EM. This code has been developed by Michalchuk and Morrison

The mechanism and theory behind this model is presented below:

- The initial shockwave that is incident on the EM initially excites the acoustic modes of the crystal. Acoustic modes of vibration are the modes where all molecules in a unit cell move in phase with one another. There are three acoustic modes relating to motion in the *x, y* and *z* directions. This energy then rapidly equilibrated over all lattice modes of vibration, *q*, to an upper limit of $\Omega_{max.}$ This is the upper limit of the so called *phonon bath*, the region in which motion of the vibrational spectrum is due to the delocalised motion of the molecules.

- The heating of the material is defined by the Grüneisen parameter. The Grüneisen parameter,γ, is defined by Equation 2.2. And describes how the compression of a material affects the change in temperature of the material. The Grüneisen parameter is assumed to be constant across all EMs-which is

generally a good approximation based on experimental data.[32] It is used to calculate the thermal energy under shock conditions.

- $\left(\frac{T_f}{T_0}\right) = \left(\frac{V_f}{V_0}\right)^{-\gamma}$ (2.2)

- As the compressibility of all materials is considered equivalent, the final bulk temperature of the material will be the same. For a value of $V/V_0 \approx 0.8$ with a value of $\gamma \approx 4$. Therefore, the final temperature upon compression is 953.6 K, with a ΔT = 655.6 K. The corresponding initial quasi temperature of the phonon bath is obtained by equation 2.3, and is directly proportional to C_{tot}/C_{ph}, where C_{tot} is the heat capacity of the complete set of vibrations and C_{ph} is the heat capacity of the phonon bath.

  ○

$$C_v = \int_0^{\Omega_{max}} \frac{\partial n}{\partial T} \hbar\omega \, g(\omega) \, d\omega \quad (2.3)$$

- Excess phonon energy is then up-pumped through phonon-phonon collisions. To allow for phonon scattering to occur, the vibrational motion of the material is assumed to be anharmonic. This allows for phonons to scatter off one another This can be explained by borrowing some terms from vibrational spectroscopy. Overtone and combination pathways of phonons lead to the excitation of initial impact energy. In vibrational spectroscopy, an overtone transition is due to the quantum number of the vibration changes in integer quantities. Here overtone energy levels are assumed to be integral multiples of phonon modes. Within this model, the second order overtone is considered to be the upper limit, as the rate of phonon-phonon scattering decreases with increasing order.

- The rate of phonon up pumping is: $\tau \propto V^3 \delta(-\omega_1 - \omega_2 - \Omega)$. Where δ is the 2 phonon density of states, in which the scattering of 2 phonons forms a third phonon of higher frequency. V^3 is the strength of scattering, as defined by the third order anharmonicity constant. The magnitude of V^3 follows: qqq > qqQ > qQQ > QQQ. Where q is an external mode (below Ω_{max}) and Q is an internal mode.

- The 2phonDOS that is obtained from the overtone scattering pathways are calculated and projected onto the phonon DOS. This forms the set of phonons that then scatter through the combination pathways; q_1q_2Q and q_1QQ (Steps 1 and 2 respectively in Figure 2.4). This set of phonons is called a 2phonDoS (the density of states which results from the combination of two phonons scattering off one another). The resulting 2phonDOS that is formed from these combination pathways is then projected over the underlying DOS and integrated. This provides a numerical quantification for the ease at which energy can be transferred from the acoustic modes of the crystal up to the localised, trigger bonds of the energetic material. This integral value is described as the *up-pumped density*.

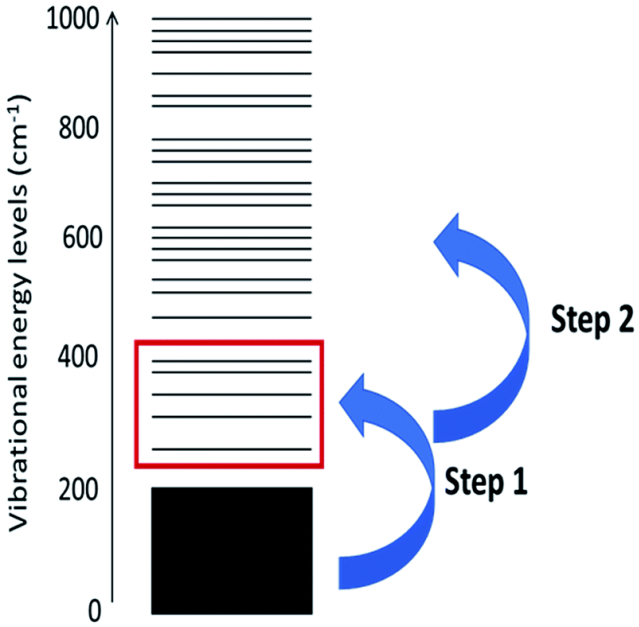

Figure 2.4. Showing the two step vibrational up-pumping mechanism. The black box denotes modes in the phonon bath, while the red rectangle represents the doorway modes.

Now that the overall mechanism for VUP.PY has been described, the work flow to carry out a vibrational up-pumping calculation will be described.

1. A vibrational frequency calculation is carried out at the Γ-point of the Brillouin zone using DFPT as implemented in CASTEP19. This is the vibrational spectrum of the structure.

2. Following the calculation, Gaussian smearing of 5 cm^{-1} is applied to the spectrum to approximate phonon dispersion. The spectrum is then normalised by the number of molecules in the unit cell. This acts as the input for the vibrational up-pumping procedure.

3. The DoS is split into two sections. The first is characterised by the low frequency, lattice modes which are dominated by external vibrations of the system (i.e. the motion of molecules relative to one another), while high frequency modes represent the internalised vibrational modes of the molecules in a system (i.e. the internal bond stretches, angle bends etc). The upper limit of the delocalised low frequency modes is characterised by the wavenumber $\Omega_{max.}$

4. Ω_{max} is identified on a case-by-case basis. It is known that Ω_{max} typically occurs in the region 200 ± 50 cm^{-1}, and is preceded by a region of continuous vibrational motion (i.e indiscreet gaussian peaks) and is succeeded by a large gap in the vibrational spectrum. However, visual inspection of the vibrational spectrum alone will not give the accurate value of Ω_{max}. This is a specific issue for identifying Ω_{max} in EMs. This is due to the abundance of functional groups such as $-NH_2$ and specifically $-NO_2$, which are, for lack of a better scientific term, waggly. Vibrational motion associated with these functional groups typically occur at lower wavenumbers than other functional groups. Therefore, it is possible that so called amalgamated motion occurs around Ω_{max}. Due to not knowing exactly which vibrational modes in the DoS represent, determining Ω_{max} from visual inspection of the DoS alone is not an accurate route. Another visual inspection that can be done is animating the simulated eigenvectors in Jmol, and visually monitoring when the vibrations change from delocalised to localised. Again, this method offers a considerable margin of error. A third, more accurate, method of determining Ω_{max} is done by monitoring the molecular centre of mass (CoM) displacement at each eigenvector. This is done individually for each molecule at each eigenvector and averaged across the number of molecules.[33] A combination of these approaches is used to assign $\Omega_{max.}$

5. After determining Ω_{max} the number of modes in the phonon bath is then counted, as this provides the basis for normalisation during the VUP.PY calculation.

6. The shock temperature is then calculated for the specific material. This is then applied to the phonon DoS and leads to a “hot” phonon bath. The shock temperature is then calculated using the ratio of the total bulk heat capacity of the material to the heat capacity with respect to the phonon bath: C_{tot}/C_{ph} where a ratio of 1:1 = 655.5 K, as proven in previous work.[33]

7. The input DoS is normalised to the number of vibrations which make up the phonon bath, which is denoted by Z(6+Y), where Z is the number of molecules in the unit cell, and Y is the number of amalgamated modes (defined as delocalised modes with a small degree of localised character).

8. The DoS is then thermally populated according to Bose-Einstein statistics, and then exposed to the calculated shock temperature which results in increased excitation of the low-energy phonon modes.

9. The 2phonDoS is then generated and projected over the 1-3 Ω_{max} region, as phonon collisions which result in excitation of higher modes is unlikely. This projected 2PhonDoS is shown visually through a red overlay as seen simplistically in Figure 2.3 and represents the total area over which energy can be up-pumped onto.

10. The integration of the 2phonDoS over the underlying DoS gives the up-pumped density, the metric which is used to compare relative impact sensitivities. The higher the value of up-pumped density, the more efficiently the crystal lattice of the EM can trap mechanical energy in its molecular vibrations.

11. The calculated up-pumped density is compared to experimental sensitivity, where available. This value more importantly can be compared to the calculated up-pumped density of other EMs (as is the case in Figure 1.3).

This overall VUP.PY method therefore includes the use of two other codes, the first for monitoring the CoM displacement over each eigenvector in the vibrational spectrum to determine the value of Ω_{max}, and the second to calculate the total heat capacity related to the vibrational motion, in order to determine the shock temperature, T_{shock}. Use of CoM displacement of molecules and the cumulative heat capacity of phonons with regard to wavenumber are referred to throughout this work to aid with the determination of the position of Ω_{max} and T_{shock}.

As the phonon DoS is directly affected from crystal packing and molecular structure, it is possible to rationalise the predicted IS of a material to its solid state structure, this is explored on a case-by-case basis throughout this thesis.

References

1 C. Morrison, D. Rankin and N. W. Mitzel, *Structural Methods in Molecular Inorganic Chemistry* , Wiley, 2013.

2 Sholl DS and Steckel JA, *Density functional theory: A Practical Introduction*, John Wiley & sons, Inc., 2009.

3 E. G. Lewars, *Computational chemistry: Introduction to the theory and applications of molecular and quantum mechanics*, Springer Netherlands, 2011.

4 M. Born and R. Oppenheimer, Zur Quantentheorie der Molekeln, *Ann. Phys.*, 1927, **389**, 457–484.

5 D. R. Hartree, The Wave Mechanics of an Atom with a Non-Coulomb Central Field. Part II. Some Results and Discussion, *Math. Proc. Cambridge Philos. Soc.*, 1928, **24**, 111–132.

6 V. Fock, Näherungsmethode zur Lösung des quantenmechanischen Mehrkörperproblems, *Zeitschrift für Phys.*, 1930, **61**, 126–148.

7 A. Tkatchenko and M. Scheffler, Accurate molecular van der Waals interactions from ground-state electron density and free-atom reference data, *Phys. Rev. Lett.*, 2009, **102**, 073005.

8 C. Lee, W. Yang and R. G. Parr, Development of the Colle-Salvetti correlation-

energy formula into a functional of the electron density, *Phys. Rev. B*, 1988, **37**, 785.

9 J. Tirado-Rives and W. L. Jorgensen, Performance of B3LYP density functional methods for a large set of organic molecules, *J. Chem. Theory Comput.*, 2008, **4**, 297–306.

10 J. P. Perdew, K. Burke and M. Ernzerhof, Generalized gradient approximation made simple, *Phys. Rev. Lett.*, 1996, **77**, 3865–3868.

11 J. Heyd, G. E. Scuseria and M. Ernzerhof, Hybrid functionals based on a screened Coulomb potential, *J. Chem. Phys.*, 2003, **118**, 8207.

12 J. Heyd and G. E. Scuseria, Efficient hybrid density functional calculations in solids: Assessment of the Heyd–Scuseria–Ernzerhof screened Coulomb hybrid functional, *J. Chem. Phys.*, 2004, **121**, 1187.

13 J. Heyd, J. E. Peralta, G. E. Scuseria and R. L. Martin, Energy band gaps and lattice parameters evaluated with the Heyd-Scuseria-Ernzerhof screened hybrid functional, *J. Chem. Phys.*, 2005, **123**, 174101.

14 M. J. Frisch, G. W. Trucks, H. B. Schlegel, G. E. Scuseria, M. A. Robb, J. R. Cheeseman, G. Scalmani, V. Barone, G. A. Petersson, H. Nakatsuji, X. Li, M. Caricato, A. V. Marenich, J. Bloino, B. G. Janesko, R. Gomperts, B. Mennucci, H. P. Hratchian, J. V. Ortiz, A. F. Izmaylov, J. L. Sonnenberg, D. Williams-Young, F. Ding, F. Lipparini, F. Egidi, J. Goings, B. Peng, A. Petrone, T. Henderson, D. Ranasinghe, V. G. Zakrzewski, J. Gao, N. Rega, G. Zheng, W. Liang, M. Hada, M. Ehara, K. Toyota, R. Fukuda, J. Hasegawa, M. Ishida, T. Nakajima, Y. Honda, O. Kitao, H. Nakai, T. Vreven, K. Throssell, J. Montgomery, J. A., J. E. Peralta, F. Ogliaro, M. J. Bearpark, J. J. Heyd, E. N. Brothers, K. N. Kudin, V. N. Staroverov, T. A. Keith, R. Kobayashi, J. Normand, K. Raghavachari, A. P. Rendell, J. C. Burant, S. S. Iyengar, J. Tomasi, M. Cossi, J. M. Millam, M. Klene, C. Adamo, R. Cammi, J. W. Ochterski, R. L. Martin, K. Morokuma, O. Farkas, J. B. Foresman and D. J. Fox, 2016.

15 S. J. Clark, M. D. Segall, C. J. Pickard, P. J. Hasnip, M. J. Probert, K. Refson and M. C. Payne, First principles methods using CASTEP, *Zeitschrift fuer Krist.*, 2005, **220**, 567–570.

16 R. Dovesi, V. . Saunders, C. Roetti, R. Orlando, C. M. Zicovich-Wilson, F. Pascale, B. Civalleri, K. Doll, N. . Harrison, I. . Bush, P. D'Arco, M. Llunell, M. Causa, Y. Noel, L. Maschio, A. Erba, M. Rerat and S. Casassa, 2017.

17 K. Refson, P. R. Tulip and S. J. Clark, Variational density-functional perturbation theory for dielectrics and lattice dynamics, *Phys. Rev. B - Condens. Matter Mater. Phys.*, 2006, **73**, 155114.

18 J. J. P. Stewart, Optimization of parameters for semiempirical methods I. Method, *J. Comput. Chem.*, 1989, **10**, 209–220.

19 J. J. P. Stewart, Optimization of parameters for semiempirical methods V: Modification of NDDO approximations and application to 70 elements, *J. Mol. Model.*, 2007, **13**, 1173–1213.

20 E. G. Lewars, in *Computational Chemistry*, Springer, Dordrecht, 2011, pp. 391–444.

21 A. Gavezzotti, Calculation of lattice energies of organic crystals: The PIXEL integration method in comparison with more traditional methods, *Zeitschrift fur Krist.*, 2005, **220**, 499–510.

22 A. Gavezzotti, Non-conventional bonding between organic molecules. the 'halogen bond' in crystalline systems, *Mol. Phys.*, 2008, **106**, 1473–1485.

23 M. G. Reeves, P. A. Wood and S. Parsons, MrPIXEL: Automated execution of Pixel calculations via the Mercury interface, *J. Appl. Crystallogr.*, 2020, **53**, 1154–1162.

24 W. Zou, R. Kalescky, E. Kraka and D. Cremer, Relating normal vibrational modes to local vibrational modes with the help of an adiabatic connection scheme, *J. Chem. Phys.*, 2012, **137**, 1–10.

25 E. Kraka and D. Cremer, Dieter Cremer's contribution to the field of theoretical chemistry, *Int. J. Quantum Chem.*, 2019, **119**, 1–28.

26 E. Kraka, W. Zou and Y. Tao, Decoding chemical information from vibrational spectroscopy data: Local vibrational mode theory, *Wiley Interdiscip. Rev. Comput. Mol. Sci.*, 2020, **10**, 1–34.

27 Y. Tao, W. Zou and S. Nanayakkara, LModeA-nano: A PyMOL plugin for Calculating Bond Strength in Solids, Surfaces and Molecules via Local Vibrational Mode Analysis, *J. Chem. Theory Comput.*, 2022, **18**, 1821–1837.

28 M. Sućeska, Calculation of the Detonation Properties of C-H-N-O explosives, *Propellants, Explos. Pyrotech.*, 1991, **16**, 197–202.

29 M. Sućeska, Calculation of detonation parameters by EXPLO5 computer program, *Mater. Sci. Forum*, 2004, **465**–**466**, 325–330.

30 M. Suceska, in *Proc. of 32nd International Annual Conference of ICT, Karlsruhe, Germany, 2001*, OZM Research, Pardubice, 2001, pp. 110/1-110/13.

31 M. Suceska, H. Y. S. Chan, B. Stimac and M. Dobrilovic, BKW EOS: History of Modifications and Further Improvement of Accuracy with Temperature-Dependent Covolumes of Polar Molecules, *Propellants, Explos. Pyrotech.*, , DOI:10.1002/PREP.202100278.

32 S. M. Peiris and G. J. Peirmarini, *Static Compression of Energetic Materials*, Springer Berlin Heidelberg, 2008.

33 A. A. L. Michalchuk, J. Hemingway and C. A. Morrison, Predicting the impact sensitivities of energetic materials through zone-center phonon up-pumping, *J. Chem. Phys.*, 2021, **154**, 1–11.

Chapter 3

Calculation of heat of formation and determination of bond strengths by local mode analysis

3.1. Introduction

Computational screening presents an attractive route in the new materials pipeline, as it offers a cost-effective way to assess candidates prior to synthesis. This is particularly desirable in the field of energetics where safety testing (such as impact, spark and friction sensitivity measurements) typically require gram-scale quantitates of compounds to be synthesised. This is extremely dangerous work when the material is novel and may initiate on the slightest perturbation.

Having access to reliable predictive models also opens up routes to the rational design of new energetics, by offering a path towards understanding structure-property relationships. Previous work in our group has focused on the ability to predict the impact sensitivities of EMs using first principles simulations, and our methods, which are based on a vibrational up-pumping model, have demonstrated success for a range of structurally and energetically diverse materials.[1,2,3] This predictive model highlighted the importance of low energy (*ca*. 200 ± 50 to 600 ± 150 cm^{-1}) molecular vibrational modes to channel (up-pump) the energy arising from the phonon scattering of the many low energy lattice mode vibrations which become vibrationally hot following a mechanically-induced shock event. Trapping this energy in the low energy molecular vibrations induces large amplitude vibrations that distort the molecular structure to the degree that electronic changes occur: band gaps narrow, electrons flow and unstable species emerge all on the timescale of a molecular vibration.[4] This marks the start of initiation. It therefore follows that crystal lattices with a high density of low-lying molecular vibrations will likely be sensitive to shock-induced detonation. The flip side also holds true: crystal lattices that are vibrationally sparse in this region will likely be shock-insensitive and are thus safer to handle.

Predicting impact sensitivities is only one aspect of an EM computational screening process. Also of key importance is the stored energy in the molecule, which can be gleaned from the solid-phase heat of formation energy, $\Delta H_{f(s)}$. This provides a route to calculating the heat of combustion, which in turn allows prediction of several parameters including the detonation pressure and the velocity and heat of explosion,[5] using thermo-chemical software methods such as CHEETAH[6] or EXPLO-5.[7]

The first step in calculating $\Delta H_{f(s)}$ begins with the gas-phase heat of formation, $\Delta H_{f(g)}$, and various methods have been proposed for this over the years. For instance, Benson's group increment theory (BGIT) exploited experimental heats of formation for individual groups of atoms to develop group equivalence values for linear and branched alkanes and alkenes.[8] While impressive at the time of inception, its application is limited to the types of molecules represented in the training set, and so it has limited scope beyond this area. More recently, quantitative structure-property relationship (QSPR) models have been realised as a powerful tool to explore the relationships that link molecular structure to material properties. Vatani *et. al*[9] devised a new QSPR method for predicting heats of formation for over 1000 organic molecules, covering almost all organic functional groups. However, transition and main group elements were not included in the training set, so whilst excellent results were obtained, widespread application is again limited.

Within the field of EMs isodesmic reaction equations[1011] and the atom and group equivalence methods[12] are commonly applied. The former relies on a reaction equation where the types of chemical bonds in the reactants and products are conserved, and the heats of formation are known for all other molecules in the reaction bar the one unknown.[13] Any intrinsic error associated with calculating any particular chemical bond is thereby cancelled out, meaning that relatively low-level computational methods can be employed to give fairly accurate results.[11] This method has been employed in computational chemistry for over 50 years, with recent developments automating the generation of parts of the isodesmic reaction equation.[14] But as a technique, in general, it has found little application beyond CHNO-containing molecules.

The atom equivalence method developed by Byrd and Rice is an advance on BGIT

and has been extensively applied to EMs,[15–18] but is again restricted to CHNO-containing molecules. Here atom equivalence energy values for the four atoms were determined through comparison of experimental heats of formation for molecules in a training set and their computationally derived molecular energies.[12] This method works well, reporting root mean square deviation of 12.6 kJ mol^{-1} and is arguably more efficient than the isodesmic equation route, as it requires just the optimised energy of the molecule of interest expressed at a prescribed quantum mechanical model chemistry. A further advantage is the absence of any reliance on other experimental data. However, the continued application to CHNO-only molecules limits its application in a computational screening programme for new EMs which should have the flexibility to draw upon main group and transition metal elements.

Given the limitations of these two methods, herein the use of the semi-empirical method PM7 to determine $\Delta H_{f(g)}$ has been persued.[19] This has been shown by Wan et al to out-perform previous semi-empirical methods for a set of 142 organic molecules.[20] Elioff *et.* al evaluated its capabilities compared to both the isodesmic and the group equivalence methods for nitrogen-containing organic molecules.[21] While the outcome showed that PM7 was the least accurate of the three (R^2 line of best fit against experimental data = 0.986, compared to 0.999 and 0.995 for the isodesmic and atom equivalence methods, respectively), it still performs relatively well, and carries the advantage of being an easily deployed method that can be used for any molecule containing atoms from H–La and Lu–Bi. Fomin *et al*[22] tested the PM7 method alongside other semi-empirical methods, namely PM6, PM5, PM3, AM/1 and MNDO, for calculating $\Delta H_{f(g)}$ for copper and alkaline earth metal complexes. They concluded that PM6 and PM7 both perform well, reporting R^2 values of 0.961 and 0.960, respectively. While these results are encouraging, further validation for the accurate prediction of $\Delta H_{f(g)}$ for a broader range of inorganic molecules would be welcome and will be provided here. The PM7 method also carries the advantage that no further calculations beyond a geometry optimisation are required, which renders it attractive as part of a high throughput study. Moreover, semi-empirical calculation methods have a wide application and user base, and are being continuously improved.[20]

Converting $\Delta H_{f(g)}$ to $\Delta H_{f(s)}$ requires the addition of an intermolecular interaction energy term, as captured by the sublimation energy, ΔH_{sub}, or the lattice energy, ΔH_L

(formally, $\Delta H_L = -\Delta H_{sub} - 2RT$). For single-component molecular solids, Politzer *et. al* have developed a route to determine ΔH_{sub} from consideration of the electrostatic potential (ESP).[2324] While they have applied this analysis to estimate many liquid, solid and solution parameters dependant on non-covalent interactions[25,26] it is their relationship to calculate ΔH_{sub} which is most relevant here. The method was developed initially using a training set of 34 CHNO molecules, and further parametrised by Byrd *et. al* using a training set of 38 CHNO-containing energetic molecules.[12] The ESP method tested here uses the parameters proposed by Byrd, as parameterisation was carried out at using the B3LYP/6-31G* computational model, rather than the HF/STO-5G* level originally used by Politzer. In addition, Byrd's training set included functional groups more likely to be present in EMs (e.g. azides and nitro groups).

For salts, an attractive route to $\Delta H_{f(s)}$ from $\Delta H_{f(g)}$ is via calculation of ΔH_L using the method developed by Jenkins *et. al*[27,28] that relies only on knowledge of the molecular (formula unit) volume and the stoichiometry of the salt. This method has been used by Gao *et. al*[29] to compare the estimated values of $\Delta H_{f(s)}$ for 33 energetic salts to their respective experimental values, using the G2 method to calculate the $\Delta H_{f(g)}$ terms for the ions based on their proton or electron affinities. They reported R^2 = 0.983, with a maximum deviation of 158.5 kJmol^{-1}.

Co-crystals are an important development in the field of EMs,[30] and so the ability to predict enthalpies of formation for these materials is also important. Previous attempts have met with limited success. For instance, Zhang *et. al*[31] and Bozkuş *et. al*[32] both used an atomisation energy method[33] which can formally only be used to calculate the heat of formation of gas-phase species. Ma *et. al*[34] used isodesmic equations to calculate $\Delta H_{f(g)}$ for the co-formers of a CL-20/MTNP co-crystal, and then predicted ΔH_{sub} using a relationship based on the melting point of the co-crystal. While this method is promising, its application is limited if the melting point is not known. Gavezzotti developed the PIXEL method to calculate ΔH_L as a sum of Coulombic, polarisation, dispersion and repulsion intermolecular energies in a crystal structure and has been shown to have the correlation R^2 = 0.845 between experimental and calculated ΔH_L for 154 organic crystal structures.[35] The method was recently expanded to include parameterisation for transition metal complexes.[36] Another route to obtaining ΔH_L is through the more computationally demanding

dispersion-corrected density functional theory (DFT-D).[37–40] For the co-crystals considered here, it is uncommon to measure $\Delta H_{f(s)}$ experimentally. Therefore in lieu of comparison to experimental data, formation enthalpies using both PIXEL and DFT-D will be computed and the two methods compared against one another.

In addition to having reliable routes to predict $\Delta H_{f(s)}$, having knowledge of the strengths of the individual bonds within a molecule is also valuable information at the EM molecular design stage, as it can provide information on the first-stage detonation pathway. Historically, intramolecular bond strengths have been calculated through heterolytic bond cleavage reactions, but this proves problematic beyond the first bond breaking reaction, as each subsequent bond breakage reaction is performed on increasingly unstable molecular fragments,[41] or requires a separate bond breaking reaction for each bond to be investigated.[42] This is particularly problematic for ring systems, where breaking one bond introduces additional strain in the remaining bonds, such that isolating one bond becomes an impossible task. Alternatively, computation of the bond force constants offers a direct route to determining the bond strengths of all bonds within a molecule without recourse to molecular fragmentation. However, the normal modes of molecular vibration, from which the force constants are extracted, are commonly a complex mix of bond stretching, angle bending and twisting motions, meaning that pure bond force constants can rarely be obtained. Recent developments by Konkoli and Cremer[43,44,45] have allowed for the mass decoupling of the normal modes of vibration, to recast the eigenvectors onto a new set of modes, termed the local modes of vibration, that correlate directly with individual bond stretches, angle bends etc. Their work has shown that the resulting local mode force constants thus obtained are a direct measure of bond strength.[46] Thus carrying out local mode analysis across a broad range of molecules (both energetic and non-energetic) provides information on the relationship between bond length and bond strength of the most common chemical bonds in EMs, which has the potential to be utilised for molecular design.

Herein, a set of 20 CHNO-containing molecules and a further 31 inorganic molecules was constructed to benchmark the PM7 method against isodesmic equation reactions and the atom equivalence method to calculate $\Delta H_{f(g)}$. Additionally, methods for converting $\Delta H_{f(g)}$ to $\Delta H_{f(s)}$ using the methods proposed by Byrd, Jenkins, and by

the PIXEL method/DFT-D for single-component molecular crystals, salts and co-crystals, respectively, were also pursued for 48 compounds. Local vibrational mode analysis has also been carried out on 30 molecules containing chemical bonds found in energetic molecules, to evaluate bond length/strength relationships and to ascertain the likely weakest bonds in energetic molecules. Finally, both parameters have been highlighted for their potential to be included in a computational screening programme for new energetic materials.

3.2. Computational Methods

All optimisations and vibrational frequency calculations were performed at the B3LYP/6-31G* level, as implemented in Gaussian16.[47]

Gas-phase heat of formation: Isodesmic equations. Equations were devised to ensure the type of chemical bonds were conserved, and that the heats of formation of all other molecules in the equation were known (see Appendix Table 2). The heat of reaction, ΔH_R, is then calculated according to Equation 1.

$$\Delta H_R = \Delta E_0 + \Delta ZPE + \Delta H_T + \Delta nRT \quad \text{(Equation 1)}$$

Where ΔE_0 is the change in energy between the products and reactants, ΔZPE is the change in the zero-point energies between products and reactants, and ΔH_T is the thermal correction from 0 to 298 K. As the number of atoms remain constant in the reaction, ΔnRT equals zero. The calculated heat of reaction is then equated to Equation 2. Assuming the molecule of interest is a reactant in the isodesmic equation then its heat of formation is calculated by subtracting the known heats of formation of the other reactants and products from ΔH_R.

$$\Delta H_R = \sum \Delta H_{f(g)\ \text{products}} - \sum \Delta H_{f(g)\ \text{reactants}} \quad \text{(Equation 2)}$$

Gas-phase heat of formation: Atom equivalence method. Formation energies were determined according to Equation 3, where E is the optimised energy of the molecule, n_j is the number of atoms of type j and e_j is the atom equivalence value of atom j, as determined by Byrd and Rice.[9]

$$\Delta H_{f(g)} = E - \sum n_j e_j \quad \text{(Equation 3)}$$

Gas-phase heat of formation: Semi-empirical PM7 method. The semi-empirical PM7[19] method was utilised as presented in Gaussian 16, using geometries optimised to global minima from the previously mentioned calculations for improved accuracy. For molecules containing 3rd row and higher atoms, the SCF=YQC algorithm was used, as suggested in the PM7 documentation.

Solid-state heat of formation: single-component solids. The solid heat of formation for single component materials were calculated using Equation 4, where $\Delta H_{f(g)}$ was calculated using the PM7 method as described above, and ΔH_{sub} was calculated using the ESP method as described by Equation 5.

$$\Delta H_{f(s)} = \Delta H_{f(g)} - \Delta H_{sub} \text{ (Equation 4)}$$

$$\Delta H_{sub} = a(SA)^2 + b\sqrt{\sigma_{tot}^2 \nu} + c \text{ (Equation 5)}$$

Where a, b and c are semi-empirically deduced fitting parameters proposed by Byrd *et. al.*[12] SA is the surface area of the 0.001 electronbohr^{-3} isosurface of the electrostatic potential of the the molecule, σ_{tot}^2 is the measure of variablity of electronic potential on the surface, and ν is the degree of balance between the positive and negative charges on the isosurface. The latter three parameters were calculated using Multiwfn.[48]

Solid-state heat of formation: salts. For the energetic salts $\Delta H_{f(s)}$ was calculated from Equation 6, where $\Delta H_{f(g)}$ of the cations and anions were calculated using the PM7 method as described above.

$$\Delta H_{f(s)} = \Delta H_{f(g)(cation)} + \Delta H_{f(g)(anion)} - \Delta H_L \quad \text{(Equation 6)}$$

Here, ΔH_L is expressed by Equation 7, as proposed by Jenkins et. al.[28]

$$\Delta H_L = U_{pot} + [p(n_m/2 - 2) + q(n_x/2 - 2)]RT \quad \text{(Equation 7)}$$

Where n_m and n_x are constants that depend on the nature of the ions, and are set to 3 for monoatomic ions, 5 for linear polyatomic ions and 6 for non-linear polyatomic

ions. The variables p and q denote the relative charges of the respective ions. The term U_{pot} denotes the lattice potential energy and in turn is defined by Equation 8.

$$U_{pot} = \alpha(V_m)^{\frac{1}{3}} + \beta \text{ (Equation 8)}$$

Where V_m denotes the molecular volume (V_{cell}/Z), in nm^3, and the remaining coefficients α and β are fitting terms provided by Jenkins *et al*, and which vary depending on the charge ratio of the salt.

Solid-state heat of formation: co-crystals. For lattice enthalpies calculated using PIXEL,[49] calculations were set up using MrPIXEL[50] within the Mercury interface, distributed with the Cambridge Structural Database (CSD).[51,52] Hydrogen atom positions were set to the CSD normalised positions. For DFT-D, geometry optimisation calculations were performed using CASTEP17[53] using the Perdew-Burke-Ernzerhof functional[54] with a plane-wave basis set with a cut-off energy of 900 eV, which demonstrated convergence to 1 $meVatom^{-1}$. Norm-conserving pseudopotentials were used throughout, with a *k*-point spacing of 0.05 $Å^{-1}$. The Tkatchenko-Scheffler dispersion correction scheme was applied. Lattice energies were determined by comparing the optimised energy values for the crystal structure with the energy for individual co-formers, modelled as effectively gas phase by removing all but one of the co-former molecules from the optimised crystal structure and computing a single point energy value using the same computational model as applied to the co-crystal. In cases where a unit cell vector was short, such that interactions with the nearest neighbour replica may occur (taken to be < 5 Å), the smallest unit cell vector was doubled to ensure zero interaction. This was the case for **64**, **70** and **76**. Lattice enthalpies were then calculated using Equation 9.

$$\Delta H_L = \frac{E_{cell}}{Z} - E_{co-former1} - E_{co-fomer2} \text{ (Equation 9)}$$

Where E_{cell} is the energy of the unit cell of the co-crystal and $E_{co\text{-}fomer1/2}$ is the energy of each of the co-formers modelled in the "gas phase" and *Z* is the number of molecular units in the co-crystal. The $\Delta H_{f(g)}$ terms, to convert the ΔH_L terms to $\Delta H_{f(s)}$, were calculated using PM7 as documented above.

Lattice enthalpies of individual co-formers were calculated by adding the thermodynamic correction shown in Equation 10 to the sublimation enthalpies

calculated using the ESP method described above.

$$\Delta H_L = -\Delta H_{sub} - 2RT \text{ (Equation 10)}$$

Local mode force constants. These were calculated using LMODEA,[45] following a geometry optimisation and vibrational frequency calculation, for the 31 CHNO-containing molecules listed in Appendix Table 6.

3.3. Results and Discussion

Calculating gas phase heats of formation.

To test the three different methods for calculating $\Delta H_{f(g)}$ molecules **1**-**20**, (see Figure 3.1 and Appendix Table 1) were considered. Molecules were chosen as they had reliably reported experimental $\Delta H_{f(g)}$ available in the literature, and their less complex nature meant that the construction of isodesmic reaction equations was relatively straightforward (reported in full in Appendix Table 2). As the PM7 method permits inorganic molecules to be studied, a further set of molecules which comprised main group and transition metal elements (**23**-**53**) was also studied. Notably, examples include molecules containing lead, copper and halides, which are commonly found in EMs.

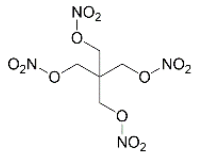

1

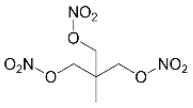

2

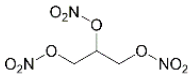

3

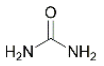

4

5

6

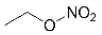

7

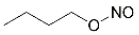

8

9

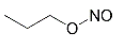

10

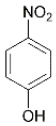

11

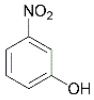

12

13

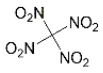

14

15

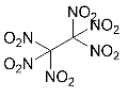

16

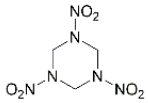

17

18

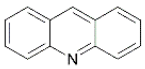

19

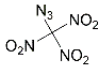

20

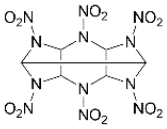

21

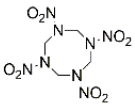

22

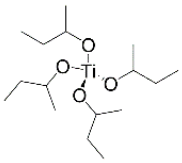

23

24

25

26

27

28

29

30

31

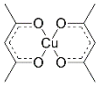

32

33

34

35

36

37

38

39

40

41

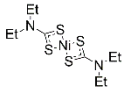

42

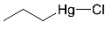

43

44

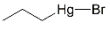

45

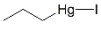

46

47

48

49

50

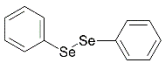

51

52

53

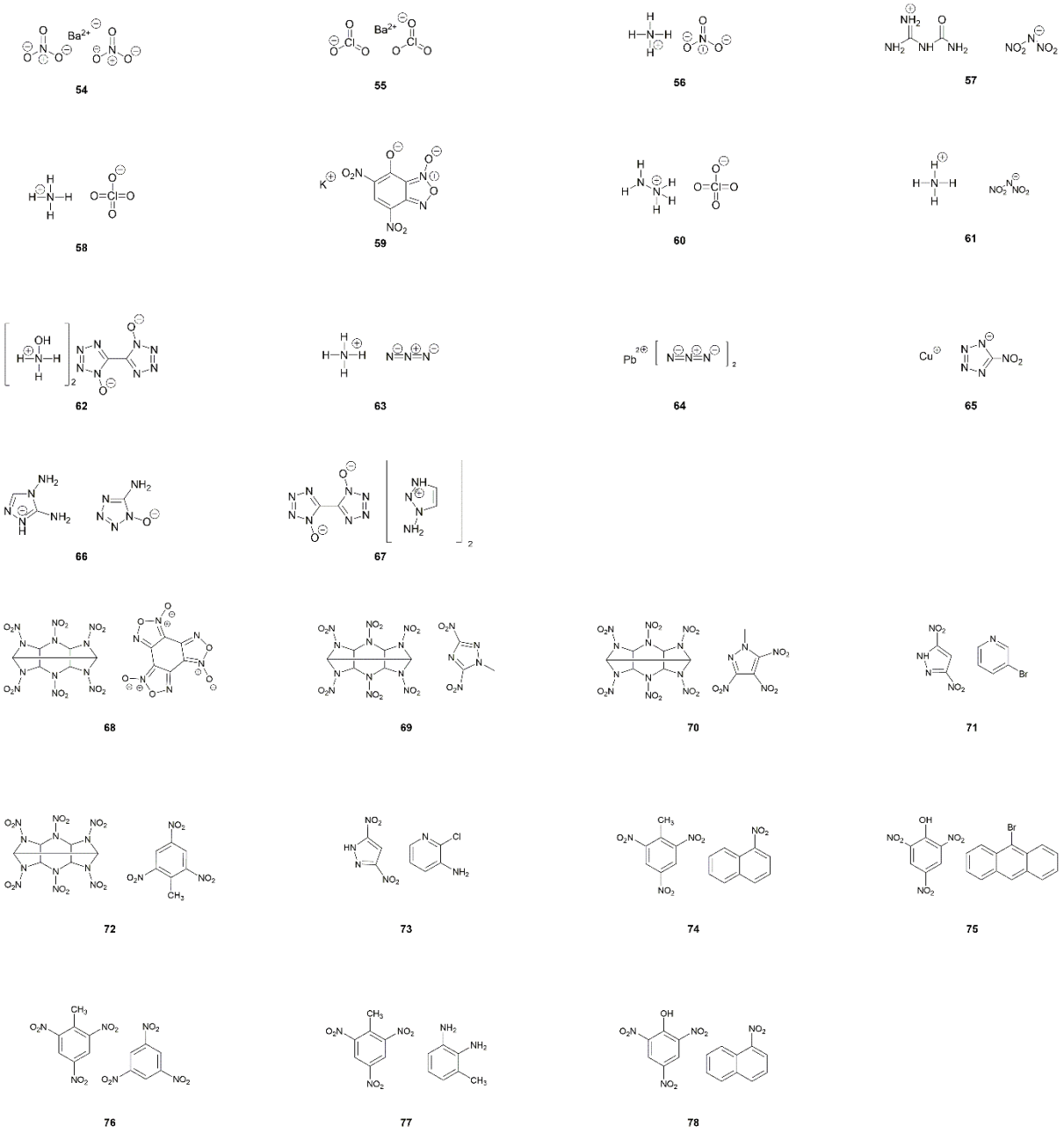

Figure 3.1.: Molecules, salts and co-crystals employed in heat of formation energy calculations.

While the majority of CHNO molecules investigated here have already been reported by Elioff,[21] the process here differs in that all molecules were first optimised at the 6-31G*/B3LYP level, followed by a single-point energy evaluation at PM7. In addition, the data set includes a further 4 molecules, namely **1, 2, 4** and **19**, which incorporates the important EMs PETN(**1**), TMETN(**2**) into the test set. Calculation of $\Delta H_{f(g)}$ for the 31 inorganic molecules (**23-53**) by PM7 has not been reported before.

When calculated $\Delta H_{f(g)}$ are compared against experimental data (Figure 3.2), the two

largest outliers for the isodesmic equation method (Figure 3.2(a) and Appendix Table 3) were PETN and TMETN (**1** and **2** respectively), which deviate from the experimental values by 106.8 and 108.0 kJ mol^{-1}, respectively. Both data points were disregarded when carrying out linear fitting, which otherwise returned an R^2 value of 0.994, and the gradient of the fitted line, m=0.989. The reasons for failure for data points **1** and **2** must rest with either the experimental formation energies and/or the geometry optimisations of PETN and TMETN, or the geometry optimisation and/or experimental formation energy of another molecule defined in their respective isodesmic equations. The atom equivalence method (shown in Figure 3.2(b)) performs considerably better for these two compounds, which suggests that the experimental formation energies and the geometry optimisations, for both PETN and TMETN, are reliable. The isodesmic reactions constructed for these two molecules both include $C(CH_3)_4$, which is absent in all other isodesmic equations constructed for the test set (see Appendix Table 2). Careful checking of the simulated geometry, to ensure the configuration obtained refers to the global minimum, suggests that the error most likely rests with the experimental heat of formation for $C(CH_3)_4$. This highlights a fundamental weakness with the isodesmic equation route, in that any error with any one term in the equation will render the calculated $\Delta H_{f(g)}$ for the target molecule as unreliable.

Using the atom equivalence method, no outliers where identified, showing the strength of this method for CHNO-containing molecules. This yields an R^2 value of 0.994 (m = 0.943), indicating that the atom equivalence method performs just as well as the isodesmic method.

Turning to the PM7 results (Figure 3.2(c)), PETN (**1**) is again the largest deviator, with the semi-empirical method overshooting the experimental value by 91.2 $kJmol^{-1}$. RDX (**17**) also appears to be less reliably calculated by this method, compared to the other two routes. Discarding **1** and **17** from the test set gives a line of best fit with R^2 = 0.993 (m = 1.083), suggesting overall that this method provides a similar level of accuracy compared to the isodesmic reaction and atom equivalence methods. The correlation with experimental data here is better than that reported by Elioff[21] (R^2=0.986) and considering the high overlap of molecules in test sets used, the improvement is likely due to the B3LYP/6-31G* geometry optimisation step, as Elioff et al relied on the PM7 method for structure optimisation as well as energy

calculation. For the inorganic molecule list, **23-53,** which were tackled by PM7 only, the R^2 value increased slightly to 0.995, with the gradient of line of best fit improved considerably (m=0.983; omitting the largest outliers ZrF_4 (**24**) and TeF_6 (**26**), which deviate from experimental values by 186 and 203 kJ mol^{-1}, respectively), suggesting its performance is just as reliable for inorganic molecules as it is for organic molecules. It is unclear why ZrF_4 and TeF_6 deviate so much from the expected values. Other related compounds, **25**, **27-29** and **34**, have been calculated accurately (although **26** is the only Te-containing compound and Zr is represented just twice in the data set). The possibility of experimental inaccuracy also cannot be ruled out.

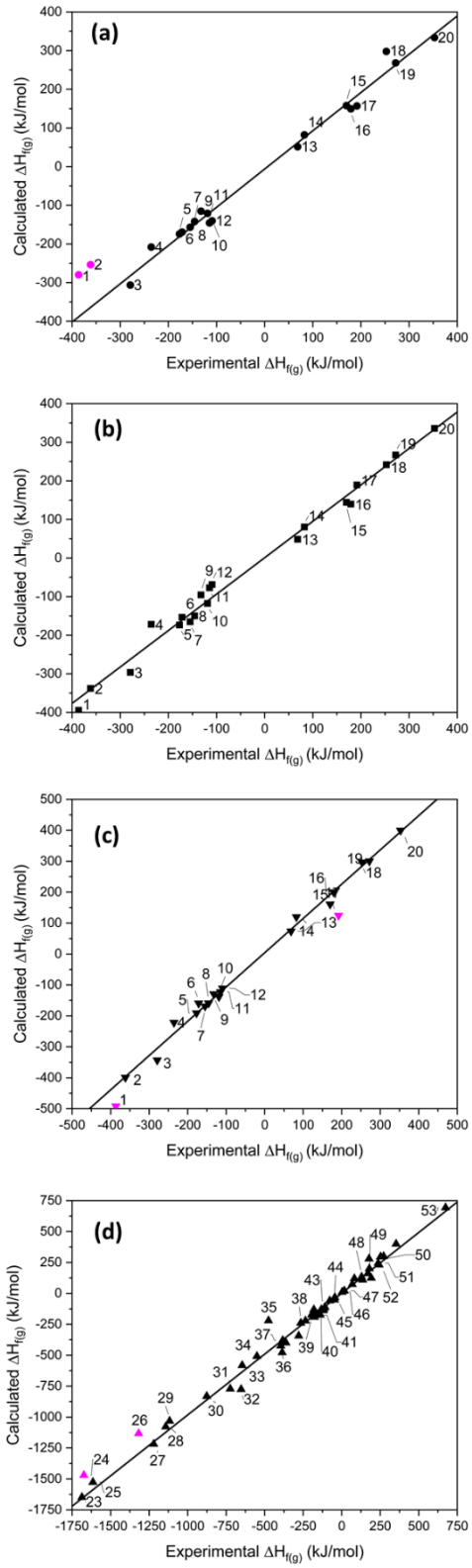

Figure 3.2: Showing calculated vs experimental gas phase heats of formation for the (a) isodesmic, (b) atom equivalence, (c) PM7 for **1**-**20** and (d) PM7 for **23-53**. Data points omitted from the lines of best fit are shown in pink.

Calculating solid heats of formation

To probe the conversion of $\Delta H_{f(g)}$ to $\Delta H_{f(s)}$, 23 of the single-component EMs were selected from the **1**-**53** test set for which experimentally determined $\Delta H_{f(s)}$ were available (see Figure 3.3(a) and Appendix Table 1), and further pursued using the ESP method. This includes 14 CHNO-containing molecules and 9 inorganic compounds. Fourteen salts (**54**-**67** in Figure 3.1) were similarly pursued using Jenkins' method, while 11 co-crystals (**68**-**78** in Figure 3.1) were explored using PIXEL and DFT-D.

For the single-component crystals, $\Delta H_{f(s)}$ calculated using the ESP method offered a line of best fit of R^2 = 0.995, m=1.100 (omitting one point that lay off the line, $Mn(CO)_3Cp$ (**35**) by 220kJmol^{-1}, see Figure 3.3(a)), indicating a good predictive result has been obtained across a broad spectrum of compounds and broad range of energies.

For the EM salts (**54**-**67**), application of Jenkins' method gives a line of best fit through the simulated values (see Figure 3.3(b)) with R^2 = 0.997 (m =0.955), and a maximum deviation from experimental values of 80.5 kJ mol^{-1} for FOX-12 (**55**). This is an improvement in the correlation reported by Gao *et. al*[29] who reported an R^2 of 0.984 for a set of 33 inorganic and CHNO EM salts, of which 19 were inorganic and the remainder CHNO. While acknowledging that the improved result obtained here could be due to the smaller test set employed in this work, it could also indicate that the PM7 method, used to calculate the $\Delta H_{f(g)}$ terms for the constituent ions, offered an improvement over the approach adopted by Gao, who relied on isodesmic equations. This latter approach is likely to be particularly problematic here as experimental formation energies of ions are required. The data set here shares two data points with Gao's (salts **56** and **61**); looking at the predictions for these in more detail, it is noted that both $\Delta H_{f(s)}$ values were more accurately calculated here, with **56** deviating from the experimental values by 17 kJ mol^{-1} (Gao's prediction differed by 24.7 kJ mol^{-1}), while **61** deviated by only 0.9 kJ mol^{-1} (Gao by 63.5 kJ mol^{-1}). This would therefore appear to further support the use of PM7 to calculate the $\Delta H_{f(g)}$ terms. There are two outliers in this fitting – lead azide (**64**) and DBX-1 (**65**), which deviate from their literature values by 222 and 145 kJ mol^{-1}, respectively. Both exist

as extended coordination complexes in the solid state, which may contribute towards their poor prediction by Jenkins' method, which was formally devised for salts.

It should be noted that TKX-50 (**62**) has two values for $\Delta H_{f(s)}$ reported in the literature. The most widely reported is 446.6 kJ mol^{-1},[55] which was calculated value using Jenkins' method, with the $\Delta H_{f(g)}$ values for the constituent ions calculated using the CBS-4M atomisation method. However, Sinditskii *et al*[56] have argued that this value is questionable when compared to the sum of the enthalpies of formation for the individual components of TKX-50 and when compared with typical heats of reaction between acid and bases. They performed bomb calorimetry experiments and determined $\Delta H_{f(s)}$ to be 111 ± 16 kJ mol^{-1}, far lower than the widely reported calculated value. The computed value here, also derived from the Jenkins' method, but utilising PM7 to calculate the $\Delta H_{f(g)}$ values for the ions, is 112.6 kJ mol^{-1}, showing that the earlier result was in error due to computation of the $\Delta H_{f(g)}$ terms for the molecular ions.

For the 11 energetic co-crystals investigated, values were calculated using two different approaches, the quicker PIXEL method, and the more computationally demanding DFT-D method (see Figure 3.3(c) and Appendix Table 6), as no experimental data was available to benchmark the predictions against. From these results, it was readily apparent that the two methods provide comparable results (R^2=0.997, m = 0.964), meaning that both options are viable to calculate $\Delta H_{f(s)}$ for co-crystals as part of a computational screening programme. PIXEL does present some limitations, however, as it is not applicable to structures where the number of molecules in the crystallographic asymmetric unit exceeds 2; for these larger crystal lattices DFT-D is at present the only realistic solution.

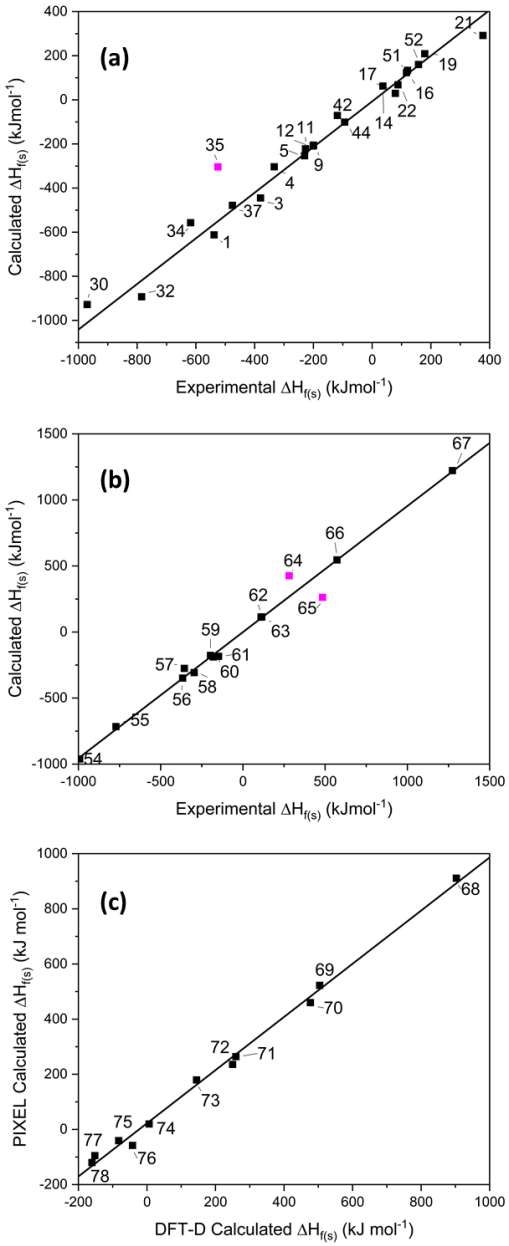

Figure 3.3: Showing the calculated solid heats of formation for (a) single component crystals, (b) salts and (c) co-crystals. Data points omitted from the lines of best fit are shown in pink.

Next, an interesting comparison between the ΔH_L of the co-crystals (from Equation 9) alongside the ΔH_L values for their respective co-formers (from Equations 5 and 10) is presented. This is shown in Figure 3.4 (and Tables S1 and S6), from which it is apparent that the sum of the latter gives a reasonable approximation of the former. This approximation would be particularly useful for co-crystals such as CL-20/HMX, which has a 2:1 ratio of co-formers[57] and thus falls outside the scope of PIXEL calculations. Accordingly, it is estimated that ΔH_L of CL-20/HMX to be *ca*. 600 kJ

mol^{-1} (based on ΔH_L (HMX) + 2 $\times$ ΔH_L(CL-20), see Appendix Table 1). Using DFT-D, the corresponding $\Delta H_{f(s)}$ prediction is 570 kJ mol^{-1}. Note that Zhang *et al*[58] estimated a considerably higher value of 861.9 ± 18.6 kJ mol^{-1}; this was obtained indirectly using a calculated heat of reaction for the formation of solid CL-20/HMX from solid ε-CL-20 and β-HMX, that in turn used a thermochemical cycle based on measured enthalpies of dissolution of all species in acetonitrile, and literature $\Delta H_{f(s)}$ values for ε-CL-20 and β-HMX.

Of course, the deviation in lattice energy for the co-crystal compared to its corresponding co-former states represents the thermodynamic driving force for the co-crystal to form. However, calculating this driving force from first principles requires many expensive simulations[59] prompting us to consider an alternative strategy rooted in comparison of ΔH_L(co-former) vs ΔH_L(solid). All eleven co-crystals investigated are stable, experimentally observed structures, and while in general the predictions correctly show that the lattice energy of the co-crystal does indeed exceed that of the sum of the co-formers, for a few structures (**68** and **78** by PIXEL, **68**, **72** and **76** by DFT-D) the relationship does not hold. This broad success is remarkable given the sum of ΔH_L(co-former) does not include explicitly the enthalpic contributions for co-former interactions and will be considered more broadly in follow up studies. Moreover, it is noted that the energy differences for those rogue data points are amongst the smallest in the data set, and likely point towards the need to include further thermodynamic energy corrections (zero point energy, entropy)[60] to improve the accuracy of the comparison. Such corrections could be obtained from calculating full phonon spectra, but these are time consuming to perform and therefore go against the computational screening philosophy which pervades this paper. Moreover, this argument is centred on thermodynamics only, and this must be tensioned against kinetics, *i.e*. the heights of the barriers separating the global and local minima on the potential energy surface. Thus, the co-crystals with a shortfall in lattice energy may also represent crystal structures that are kinetically-driven and therefore represent readily accessible stable minima that may not represent the lowest energy state.

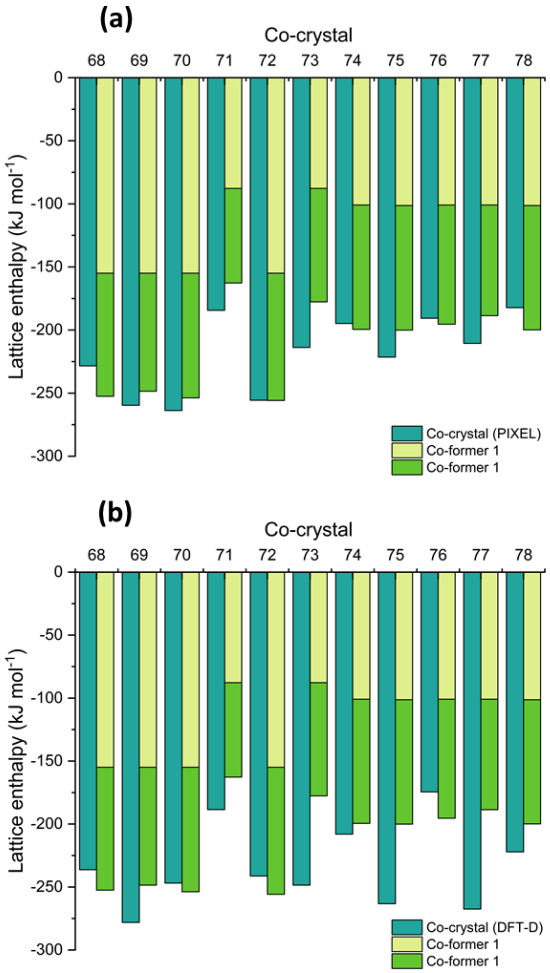

Figure 3.4. Comparison of calculated lattice enthalpies of co-crystals **68**-**78** by (a) PIXEL and (b) DFT-D, alongside constituent co-formers.

In summary, of the three methods tested here for calculating $\Delta H_{f(g)}$, PM7 performs strongest across the board in terms of highest correlation with experimental data and application to the widest range of molecules. Its strength has also been demonstrated when calculating $\Delta H_{f(s)}$ for single component solids and salts, by the ESP and Jenkins methods, respectively, with predicted values showing excellent correlation with experimental $\Delta H_{f(s)}$ values. Finally, two different methods, PIXEL and DFT-D, were compared for calculating ΔH_L terms for co-crystals and found to give comparable results. Comparison of the calculated ΔH_L terms show that, to a first approximation, the lattice enthalpy of the co-crystal is the sum of the lattice enthalpies of the constituent co-formers. This has huge potential in directing co-crystallisation studies to create new products with desired $\Delta H_{f(s)}$ values.

Local force constant calculations.

Local vibrational mode force constants were calculated for all CHNO-containing molecules in the test set, with a further ten EMs added to provide a wider and more comprehensive coverage of bond length values (31 CHNO molecules in total, Appendix Table 7, including the EMs CL-20, RDX, HMX, HNB, NTO, TATB, FOX-7, PETN and nitroglycerin). From this data, a relationship between the bond lengths and force constants of seven different covalent bonding environments can be drawn (see Figure 3.5).

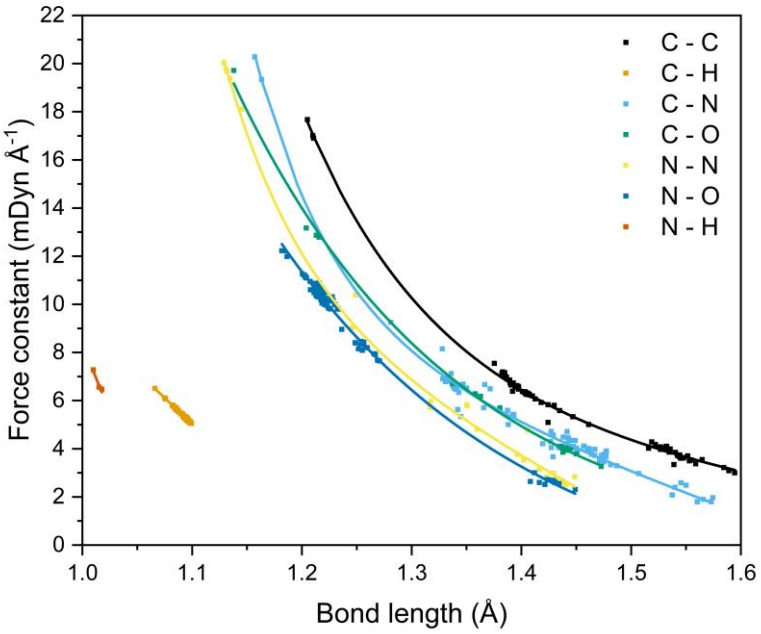

Figure 3.5: Correlation between bond lengths and local vibrational mode force constants for seven covalent bonding environments

The data shown here expands upon the relationship that has been established by Kraka *et. al* for C–C bonds occurring in both gas and solid state geometries.[45] It also mirrors the trends shown by Byler et al[61] and Ladd et al[62] for C–N bonds and C–O bonds, respectively. The studies by Byler and Ladd analysed mainly linear molecules in an effort to reduce the effect of coupling of normal vibrational modes. This limitation is elegantly side-stepped by local vibrational mode analysis through the recasting of the normal modes of vibration into the local modes through mass decoupling.[24,25] Byler *et. al.* reported bond lengths that ranged from 1.122 Å (k = 20.17 mdyn Å^{-1}, $H_3CC–NBCl_3$) to 1.555 Å (k = 3.51 mdyn Å^{-1}, $F_3C–NO$). Their data

sits comfortably on the C–N curve here, highlighting the power of the local mode analysis route to obtaining force constants for more complex molecules. Ladd *et al.* measured the vibrational frequency of the C–O bond stretch for different excited states of carbon monoxide to obtain the relationship between force constant and bond length over the range 1.088 to 1.396 Å. Their data agree quantitatively with the C–O bond curve shown in Figure 3.5 at long bond lengths, but consistently underestimates the force constants at shorter (< 1.2 Å) distances, which suggests that measuring the force constants of only excited states of CO has skewed the relationship between bond length and force constant. McKean made extensive studies of the vibrational frequencies of isolated C–H bond stretches, a property which is directly comparable to the local mode of vibration[29],64 and therefore the force constants, and presented a relationship between C–H bond length and experimentally determined stretching frequencies which mirrors the trend shown here. Cremer *et al*.[41] also calculated C–H force constants of adiabatic internal modes (an earlier name for local vibrational modes), their shortest C–H bond being 1.086 Å with a force constant of 5.58 mdyn $Å^{-1}$. This fits on the line presented in Figure 3.5, which is now further extended to 1.066 Å (and 6.46 mdyn $Å^{-1}$).

A strong correlation of force constant and bond length can be seen for all bond types, and decay functions were used to fit trend lines (Appendix Table 8) that returned R^2 values of *ca.* 0.99 for all bond types, with the exception of C–N (R^2 = 0.98) and N–H (R^2 = 0.92), although the latter corresponds to only four data points and is likely under-represented. Four bond types, C–C, C–N, C–O and N–N, encompass single to triple bond behaviour, and N–O bond types include single and double bonds, as evident from the clustering of data points. The wide range of bond lengths studied give rise to a corresponding wide range of calculated local force constant values, which for the most part follow the sequence C–C > C–N ≈ C–O > N–N ≈ N–O, although the longer distances afforded by single C–N bonds render these interactions on a par with single N–N and N–O bonds. The weakness of the long C–N bond fits with expectation: the rupture of R–NO_2 bonds have been shown to be a critical step in the decomposition of energetic materials.[65–67] The data shown in Figure 3.5 is testament to the great potential offered by the local mode analysis route: it is a quick and straightforward method to compare and contrast the bond strengths of all bonding interactions within a molecule, from which the weakest bond

can be unambiguously identified. The curves shown in Figure 3.5 in essence act as bond length/force constant calibration curves. In the instance of CL-20, a cage nitramine structure consisting of 5, 6 and 7 membered C–N rings (compound **21** in Figure 3.3.1), it has been suggested that the C–N bonds forming the cage can also act as the "trigger linkage,"[68] in addition to the generally weaker N–NO_2 bonds. This is supported here, with the C–N bonds in the more strained 5-membered rings having force constants similar to the stronger N–NO_2 bonds (3.337 vs 3.151 mdyn $Å^{-1}$, respectively). The less strained 6 membered ring contains stronger C–N bonds, with force constants ranging from 4.088-4.486 mdyn $Å^{-1}$, a considerable increase in strength from the C–N bonds present in the 5 membered rings. The relationship between bond length and force constant presented here therefore has the potential to be applied to molecular design, as the weakest bond in a molecule can be tuned by its surrounding molecular environment.

3.4. Conclusion

The reliable determination of gas-phase and solid-state heats of formation are important considerations in energetic materials research. Herein, three different methods (isodesmic reactions, atom equivalence methods and the semi-empirical method PM7) have been tested for calculating $\Delta H_{f(g)}$. All three performed well, with PM7 offering the closest correlation to experimental values overall (R^2 = 0.995 for the CHNO-only data set (**1**-**20**), falling slightly to 0.993 when the whole data set (**1**-**53**) is considered). As limitations exist for the widespread application of the isodesmic reaction and atom equivalence methods beyond CHNO-containing compounds, this work supports the use of the semi-empirical route offered by PM7 to calculating reliable $\Delta H_{f(g)}$ values for molecules beyond CHNO. The data here also suggests that an improvement in PM7 performance can be obtained if geometry optimisation is carried out using a higher level of theory prior to calculation of $\Delta H_{f(g)}$ via single point energy calculation.

Converting $\Delta H_{f(g)}$ to $\Delta H_{f(s)}$ requires consideration of an intermolecular interaction term, as expressed by the sublimation energy, ΔH_{sub}, or the lattice energy, ΔH_L. The use of the ESP method for single-component molecular crystals, and Jenkins' method for salts has been investigated. Both methods performed well for both

CHNO-solids and inorganic solids, returning R^2 values of 0.995 and 0.997, respectively, when compared with experimental data. Additionally, the lattice energies of co-crystals were evaluated using PIXEL and DFT-D, and shown to yield comparable results. Moreover, to a first approximation, it has been demonstrated that ΔH_L (and therefore $\Delta H_{f(s)}$) for co-crystals can be estimated through the sum of the corresponding values for each co-former. Thus it has been shown that reliable routes are available to provide the all-important $\Delta H_{f(s)}$ values for EM research.

In addition to heats of formation, knowledge of the individual bond strengths in molecules is important information in the design of new EMs. Herein, local vibrational mode analysis has been employed to determine the bond length vs. force constant relationships for seven different chemical bonds occurring in CHNO-containing molecules and has confirmed the expected result that a C–N bond in an EM is most susceptible to the surrounding structural environment. The bond length/force constant curves allow rationalisation of steric strain in complex EMs such as CL-20, demonstrating how the local molecular environment creates the weakest bonds most likely to rupture first on the detonation reaction pathway. This has great potential in rationalising EM molecular design.

To conclude, reliable routes to compute $\Delta H_{f(s)}$ and to establish the bond strength hierarchy for EMs has great potential to be incorporated into a computational screening programme, from which much could be learned regarding structure-property relationships for this important class of compounds.

References

1 A. S. Cumming, in *Chemical Rocket Propulsion*, Springer International Publishing, 2017, pp. 727–740.

2 A. A. L. Michalchuk, P. T. Fincham, P. Portius, C. R. Pulham and C. A. Morrison, A Pathway to the Athermal Impact Initiation of Energetic Azides, *J. Phys. Chem. C*, 2018, **122**, 19395–19408.

3 A. A. L. Michalchuk, J. Hemingway and C. A. Morrison, Predicting the impact sensitivities of energetic materials through zone-center phonon up-pumping, *J. Chem. Phys.*, 2021, **154**, 1–11.

4 A. A. L. Michalchuk, S. Rudić, C. R. Pulham and C. A. Morrison, Vibrationally induced metallisation of the energetic azide α-NaN3, *Phys. Chem. Chem. Phys.*, 2018, **20**, 29061–29069.

5 P. Politzer, P. Lane and M. C. Concha, *Computational approaches to heats of formation*, Elsevier B.V., 2003, vol. 12.

6 L. Fried and P. Souers, CHEETAH: A Next Generation Thermochemical Code (Lawrence Livermore National Laboratory), 1995.

7 M. Suceska, in *Proc. of 32nd International Annual Conference of ICT, Karlsruhe, Germany, 2001*, OZM Research, Pardubice, 2001, pp. 110/1-110/13.

8 S. W. Benson and J. H. Buss, Additivity rules for the estimation of thermochemical properties, *Chem. Rev.*, 1958, **69**, 279–324.

9 A. Vatani, M. Mehrpooya and F. Gharagheizi, Prediction of standard enthalpy of formation by a QSPR model, *Int. J. Mol. Sci.*, 2007, **8**, 407–432.

10 D. A. Ponomarev and V. V. Takhistov, What are isodesmic reactions?, *J. Chem. Educ.*, 1997, **74**, 201–203.

11 W. J. Hehre, R. Ditchfield, L. Radom and J. A. Pople, Molecular Orbital Theory of the Electronic Structure of Organic Compounds. V. Molecular Theory of Bond Separation, *J. Am. Chem. Soc.*, 1970, **92**, 4796–4801.

12 E. F. C. Byrd and B. M. Rice, Improved prediction of heats of formation of energetic materials using quantum mechanical calculations, *J. Phys. Chem. A*, 2006, **110**, 1005–1013.

13 C. Cramer, *Essentials of computational chemistry theories and models*, Wiley, Chichester, 2nd edn., 2004.

14 B. Chan, E. Collins and K. Raghavachari, Applications of isodesmic-type reactions for computational thermochemistry, *Wiley Interdiscip. Rev. Comput. Mol. Sci.*, 2020, 1–18.

15 H. J. Singh, S. Gupta and S. K. Sengupta, Computational studies on nitramino derivatives of 1-amino-1,2-azaboriridine as high energetic material, *RSC Adv.*,

2014, **4**, 40534–40541.

16 H. J. Singh, M. K. Upadhyay and S. K. Sengupta, Theoretical studies on benzo[1,2,4]triazine-based high-energy materials, *J. Mol. Model.*, 2014, **20**, 1–10.

17 Q. J. Axthammer, B. Krumm and T. M. Klapötke, Pentaerythritol-based energetic materials related to PETN, *European J. Org. Chem.*, 2015, **2015**, 723–729.

18 D. G. Piercey, D. E. Chavez, B. L. Scott, G. H. Imler and D. A. Parrish, An Energetic Triazolo-1,2,4-Triazine and its N-Oxide, *Angew. Chemie - Int. Ed.*, 2016, **55**, 15315–15318.

19 J. J. P. Stewart, Optimization of parameters for semiempirical methods VI: More modifications to the NDDO approximations and re-optimization of parameters, *J. Mol. Model.*, 2013, **19**, 1–32.

20 Z. Wan, Q. Wang and J. Liang, Accurate prediction of standard enthalpy of formation based on semiempirical quantum chemistry methods with artificial neural network and molecular descriptors, *Int. J. Quantum Chem.*, 2020, **121**, 1–16.

21 M. S. Elioff, J. Hoy and J. A. Bumpus, Calculating Heat of Formation Values of Energetic Compounds: A Comparative Study, *Adv. Phys. Chem.*, 2016, **2016**, 1–11.

22 V. N. Fomin, D. B. Gogol, I. E. Rozhkovoy and D. L. Ponomarev, Quantum chemical and thermodynamic calculations of fulvic and humic copper complexes in reactions of malachite and azurite formation, *Appl. Geochemistry*, 2017, **79**, 9–16.

23 P. Politzer, J. M. Seminario and M. C. Concha, Statitical analysis of the molecular surfae electrostatic potential: an approach to describing noncovalent interactions in condensed phases, *J. Mol. Struct. TheoChem*, 1998, **427**, 123–129.

24 P. Politzer, J. S. Murray, M. E. Edward Grice, M. Desalvo and E. Miller, Calculation of heats of sublimation and solid phase heats of formation, *Mol.*

Phys., 1997, **91**, 923–928.

25 P. Politzer and J. S. Murray, The fundamental nature and role of the electrostatic potential in atoms and molecules, *Theor. Chem. Acc.*, 2002, **108**, 134–142.

26 P. Politzer and J. S. Murray, Relationships between Lattice Energies and Surface Electrostatic Potentials and Areas of Anions, *J. Phys. Chem. A*, 1998, **102**, 1018–1020.

27 H. D. B. Jenkins, H. K. Roobottom, J. Passmore and L. Glasser, Relationships among ionic lattice energies, molecular (formula unit) volumes, and thermochemical radii, *Inorg. Chem.*, 1999, **38**, 3609–3620.

28 H. D. B. Jenkins, D. Tudela and L. Glasser, Lattice potential energy estimation for complex ionic salts from density measurements, *Inorg. Chem.*, 2002, **41**, 2364–2367.

29 H. Gao, C. Ye, C. M. Piekarski and J. M. Shreeve, Computational characterization of energetic salts, *J. Phys. Chem. C*, 2007, **111**, 10718–10731.

30 S. R. Kennedy and C. R. Pulham, in *Co-crystals: Preparation, Characterization and Applications Edited*, eds. B. Aakeroy and A. Sinha, The Royal Society of Chemistry, 2018, pp. 231–264.

31 Z. Bin Zhang, T. Li, L. Yin, X. Yin and J. G. Zhang, A novel insensitive cocrystal explosive BTO/ATZ: Preparation and performance, *RSC Adv.*, 2016, **6**, 76075–76083.

32 S. I. Bozkuş, K. S. Hope, B. Yüksel, N. Atçeken, H. Nazır, O. Atakol and N. Şen, Characterization and properties of a novel energetic Co-crystal formed between 2,4,6-Trinitrophenol and 9-Bromoanthracene, *J. Mol. Struct.*, 2019, **1192**, 145–153.

33 L. A. Curtiss, K. Raghavachari, P. C. Redfern and J. A. Pople, Assessment of Gaussian-2 and density functional theories for the computation of enthalpies of formation, *J. Chem. Phys.*, 1997, **106**, 1063–1079.

34 Q. Ma, T. Jiang, Y. Chi, Y. Chen, J. Wang, J. Huang and F. Nie, A novel multi-

nitrogen 2,4,6,8,10,12-hexanitrohexaazaisowurtzitane-based energetic co-crystal with 1-methyl-3,4,5-trinitropyrazole as a donor: experimental and theoretical investigations of intermolecular interactions, *New J. Chem.*, 2017, **41**, 4165–4172.

35 A. Gavezzotti, Efficient computer modeling of organic materials. the atom-atom, Coulomb-London-Pauli (AA-CLP) model for intermolecular electrostatic-polarization, dispersion and repulsion energies, *New J. Chem.*, 2011, **35**, 1360–1368.

36 A. G. P. Maloney, P. A. Wood and S. Parsons, Intermolecular interaction energies in transition metal coordination compounds, *CrystEngComm*, 2015, **17**, 9300–9310.

37 S. Feng and T. Li, Predicting lattice energy of organic crystals by density functional theory with empirically corrected dispersion energy, *J. Chem. Theory Comput.*, 2006, **2**, 149–156.

38 J. G. Brandenburg, T. Maas and S. Grimme, Benchmarking DFT and semiempirical methods on structures and lattice energies for ten ice polymorphs, *J. Chem. Phys.*, 2015, **142**, 1–11.

39 J. Y. Fan, Z. Y. Zheng, Y. Su and J. J. Zhao, Assessment of dispersion correction methods within density functional theory for energetic materials, *Mol. Simul.*, 2017, **43**, 568–574.

40 C. A. Morrison and M. M. Siddick, Determining the strengths of hydrogen bonds in solid-state ammonia and urea: Insight from periodic DFT calculations, *Chem. - A Eur. J.*, 2003, **9**, 628–634.

41 D. Cremer, A. Wu, A. Larsson and E. Kraka, Some Thoughts about Bond Energies, Bond Lengths and Force Constants, *J. Mol. Model.*, 2000, 396–412.

42 W. Zou, R. Kalescky, E. Kraka and D. Cremer, Relating normal vibrational modes to local vibrational modes with the help of an adiabatic connection scheme, *J. Chem. Phys.*, 2012, **137**, 1–10.

43 Z. Konkoli and D. Cremer, A New Way of Analyzing Vibrational Vibrational Modes in Terms of Internal Vibrational Modes, *Int. J.*, 1998, **67**, 1–9.

44 Z. Konkoli and D. Cremer, A new way of analyzing vibrational spectra. III. Characterization of normal vibrational modes in terms of internal vibrational modes, *Int. J. Quantum Chem.*, 1998, **67**, 29–40.

45 E. Kraka, W. Zou and Y. Tao, Decoding chemical information from vibrational spectroscopy data: Local vibrational mode theory, *Wiley Interdiscip. Rev. Comput. Mol. Sci.*, 2020, **10**, 1–34.

46 E. Kraka and D. Cremer, Dieter Cremer's contribution to the field of theoretical chemistry, *Int. J. Quantum Chem.*, 2019, **119**, 1–28.

47 M. J. Frisch, G. W. Trucks, H. B. Schlegel, G. E. Scuseria, M. A. Robb, J. R. Cheeseman, G. Scalmani, V. Barone, G. A. Petersson, H. Nakatsuji, X. Li, M. Caricato, A. V. Marenich, J. Bloino, B. G. Janesko, R. Gomperts, B. Mennucci, H. P. Hratchian, J. V. Ortiz, A. F. Izmaylov, J. L. Sonnenberg, D. Williams-Young, F. Ding, F. Lipparini, F. Egidi, J. Goings, B. Peng, A. Petrone, T. Henderson, D. Ranasinghe, V. G. Zakrzewski, J. Gao, N. Rega, G. Zheng, W. Liang, M. Hada, M. Ehara, K. Toyota, R. Fukuda, J. Hasegawa, M. Ishida, T. Nakajima, Y. Honda, O. Kitao, H. Nakai, T. Vreven, K. Throssell, J. Montgomery, J. A., J. E. Peralta, F. Ogliaro, M. J. Bearpark, J. J. Heyd, E. N. Brothers, K. N. Kudin, V. N. Staroverov, T. A. Keith, R. Kobayashi, J. Normand, K. Raghavachari, A. P. Rendell, J. C. Burant, S. S. Iyengar, J. Tomasi, M. Cossi, J. M. Millam, M. Klene, C. Adamo, R. Cammi, J. W. Ochterski, R. L. Martin, K. Morokuma, O. Farkas, J. B. Foresman and D. J. Fox, 2016.

48 T. Lu and F. Chen, Multiwfn: A multifunctional wavefunction analyzer, *J. Comput. Chem.*, 2012, **33**, 580–592.

49 A. Gavezzotti, Calculation of lattice energies of organic crystals: The PIXEL integration method in comparison with more traditional methods, *Zeitschrift fur Krist.*, 2005, **220**, 499–510.

50 M. G. Reeves, P. A. Wood and S. Parsons, MrPIXEL: Automated execution of Pixel calculations via the Mercury interface, *J. Appl. Crystallogr.*, 2020, **53**, 1154–1162.

51 C. F. Macrae, I. J. Bruno, J. A. Chisholm, P. R. Edgington, P. Mccabe, E.

Pidcock, L. Rodriguez-monge, R. Taylor, J. Van De Streek and P. A. Wood, Mercury CSD 2.0 – new features for the visualization and investigation of crystal structures, *J. Appl. Cryst.*, 2008, **41**, 466–470.

52 C. R. Groom, I. J. Bruno, M. P. Lightfoot and S. C. Ward, The Cambridge structural database, *Acta Crystallogr. Sect. B Struct. Sci. Cryst. Eng. Mater.*, 2016, **72**, 171–179.

53 S. J. Clark, M. D. Segall, C. J. Pickard, P. J. Hasnip, M. J. Probert, K. Refson and M. C. Payne, First principles methods using CASTEP, *Zeitschrift fuer Krist.*, 2005, **220**, 567–570.

54 J. P. Perdew, K. Burke and M. Ernzerhof, Generalized gradient approximation made simple, *Phys. Rev. Lett.*, 1996, **77**, 3865–3868.

55 J. J. Sabatini and K. D. Oyler, Recent advances in the synthesis of high explosive materials, *Crystals*, 2015, **6**, 1–22.

56 V. P. Sinditskii, S. A. Filatov, V. I. Kolesov, K. O. Kapranov, A. F. Asachenko, M. S. Nechaev, V. V. Lunin and N. I. Shishov, Combustion behavior and physico-chemical properties of dihydroxylammonium 5,5’-bistetrazole-1,1’-diolate (TKX-50), *Thermochim. Acta*, 2015, **614**, 85–92.

57 O. Bolton, L. R. Simke, P. F. Pagoria and A. J. Matzger, High power explosive with good sensitivity: A 2:1 cocrystal of CL-20:HMX, *Cryst. Growth Des.*, 2012, **12**, 4311–4314.

58 S. Zhang, J. Zhang, K. Kou, Q. Jia, Y. Xu, N. Liu and R. Hu, Standard Enthalpy of Formation, Thermal Behavior, and Specific Heat Capacity of 2HNIW·HMX Co-crystals, *J. Chem. Eng. Data*, 2019, **64**, 42–50.

59 C. R. Taylor and G. M. Day, Evaluating the Energetic Driving Force for Cocrystal Formation, *Cryst. Growth Des.*, 2018, **18**, 892–904.

60 J. Nyman and G. M. Day, Static and lattice vibrational energy differences between polymorphs, *CrystEngComm*, 2015, **17**, 5154–5165.

61 D. M. Byler, H. Susi and W. C. Damert, Relation Between Force Constant and Bond length for Carbon-Nitrogen Bonds, *Spectrochim. Acta*, 1987, **43**, 861–863.

62 J. A. Ladd, W. J. Orville-Thomas and B. C. Cox, Molecular parameters and bond structure-III. Carbon-oxygen bonds, *Spectrochim. Acta*, 1964, **20**, 1771–1780.

63 Z. Konkoli, J. A. Larsson and D. Cremer, A new way of analyzing vibrational spectra. IV. Application and testing of adiabatic modes within the concept of the characterization of normal modes, *Int. J. Quantum Chem.*, 1998, **67**, 41–55.

64 J. A. Larsson and D. Cremer, Theoretical verification and extension of the McKean relationship between bond lengths and stretching frequencies, *J. Mol. Struct.*, 1999, **485**, 385–407.

65 F. J. Owens, Calculation of energy barriers for bond rupture in some energetic molecules, *Molecules*, 1996, **370**, 11–16.

66 J. Sharma, W. L. Garrett, F. J. Owens and V. L. Vogel, X-ray photoelectron study of electronic structure and ultraviolet and isothermal decomposition of 1,3,5-triamino-2,4,6-trinitrobenzene, *J. Phys. Chem.*, 1982, **86**, 1657–1661.

67 J. Sharma and F. J. Owens, XPS study of UV and shock decomposed triamino-trinitrobenzene, *Chem. Phys. Lett.*, 1979, **61**, 280–282.

68 K. B. Sun, S. H. Zhang, F. de Ren, Y. P. Hao and S. H. Ba, Theoretical prediction of the trigger linkage, cage strain, and explosive sensitivity of CL-20 in the external electric fields, *J. Mol. Model.*, 2021, **27**, 1–20.

Chapter 4

Tuning energetic properties through co-crystallisation: nitrotriazolone and 4,4'-bipyridine.

4.1. Introduction

A current driver in energetic materials (EMs) research is to utilise co-crystallisation to alter the properties of already known and well-characterised compounds.[1] The potential benefits include finding ways to tune energetic performance and environmental impact by altering mechanical impact sensitivities and reducing water solubility properties, all while retaining or even improving on energetic power by improving on oxygen balance.[2] Tuning the properties of known compounds in this way also reduces the need to synthesise novel EMs, which brings stringent requirements for safety and cost. Thus re-using existing EMs, with existing manufacturing infrastructure, offers a new and accessible design space to explore new materials that will likely exhibit different properties to their parent compounds.

The first report of an EM co-crystal concerned TNT (trinitrotoluene) with CL-20 (hexanitrohexaazaisowurtzitane).[3] CL-20 has a high energy density and high explosive power but has failed to see any widespread use due to its high mechanical sensitivity.[4] In contrast, the 1:1 co-crystal was reported to have a significantly reduced impact sensitivity compared to CL-20. It was also reported that heating the co-crystal above 136 °C resulted in phase separation of the two energetic components, suggesting that the co-crystal represented a safe form for transportation. CL-20 has also been successfully co-crystallised with HMX (1,3,5,7-

tetranitro-1,3,5,7-tetrazocane),[5] and desirable properties were again obtained: the impact sensitivity was comparable to HMX while the detonation performance was predicted to exceed that of HMX. More recently, a perfectly balanced oxygen/fuel EM co-crystal was reported between the oxidiser ammonium dinitramide (ADN) with the fuel-rich pyrazine-1,4-dioxide.[6] Moreover, the impact sensitivity of the co-crystal was reported to be similar to ADN while the detonation performance was superior to ADN. An appreciable number of energetic co-crystals reports have now been prepared and characterised, including with azoles,[6–9] nitrobenzenes,[10–13] acetone peroxides,[12,14] and the field has recently been reviewed.[1]

While many reports concern the co-crystallisation of two EMs, it is also worth considering co-crystallisation of an EM with a non-energetic component. While the immediate drawback is an undeniable loss of energy density, it does pose several advantages. For instance, it provides an accessible route to tuneable intermolecular hydrogen bonds, which is a commonly employed approach in creating pharmaceutical co-crystals.[15] EMs predominantly feature nitro groups, which can act as hydrogen bond acceptors, but often lack other functional groups that provide the hydrogen bond donor moiety. Thus limiting co-crystallisation studies to only EMs likely limits the scope to explore variations in intermolecular interactions which can be employed to form stable co-crystals. Replacing one component with a non-EM hydrogen bond donor moiety lifts this limitation, and the opportunity to explore structure/property relationships is increased.

This work concerns 3-nitro-1,2,4-triazol-5-one (NTO), an insensitive EM with a detonation velocity comparable to RDX.[16] Somewhat unusually, it contains both hydrogen bond donor (N-H) and acceptor (NO_2) functional groups, but the former renders it acidic in nature (pKa= 3.67)[16] and its water solubility presents adverse

effects for aquatic life.[17] These limitations could be addressed through co-crystallisation with an appropriate partner. Its low pK_a value means that that NTO forms salts readily, and numerous metal and amine salts have been reported.[18] In an effort to obtain a co-crystal, the crystallisation propensity of NTO with a relatively strong base, 4,4'-bipyridine (BIPY) was studied, which has a singly-protonated pK_a value of 4.82.[19] According to the ΔpK_a rule,[20] this suggests that a crystal structure formed between the two components could exist as a salt, co-crystal or disordered solid form with partial proton transfer – the location of the acidic proton being dependent upon the specific crystal packing environment. A co-crystal is only expected to be form if it is thermodynamically more stable than the crystals of its components.[21,22] However, being able to predict the formation of a co-crystal versus a salt still remains a challenge when evaluating the thermodynamic properties of a system.[23]

It is now widely recognised that it is important to study the structural response of EMs over a range of operating conditions, as phase transitions have often been reported at temperature and pressure ranges relevant to the initiation pathway.[24] A recent study indicated that the predicted impact sensitivity for 1,1-diamino-2,2-dinitroethane (FOX-7) was polymorph dependent.[25] Exploring the structural response to pressure is particularly pertinent for a crystal formed between NTO and BIPY given its predicted ambiguity between the co-crystal and salt forms, and its likely alteration of material properties.

Herein, a co-component crystal of NTO and 4,4'-bipyridine (NTO.BIPY), synthesised by Dr. Hayleigh Lloyd and characterised by Dr. Xiaojiao Liu at the University of Edinburgh, is studied computationally. Ambient and high pressure single-crystal X-ray diffraction (up to *ca* 6.0 GPa) has been undertaken, supplemented with

computational modelling to track the intermolecular hydrogen bond structural parameters and to account for the change in colour of the molecular crystal at high pressure. In addition, the impact sensitivity of the NTO.BIPY co-crystal will be predicted and compared to that of NTO using our recently published theoretical model that has proven capable of accurately predicting the impact sensitivity of a broad range of EMs.[26–28]

4.2. Computational Methods

Samples of NTO.BIPY were prepared by Dr. Hayleigh Lloyd and characterised through X-ray single crystal diffraction by Dr. Xiaojiao Liu, who also carried out high pressure single crystal diffraction of the samples. These crystal structures were used as the basis for the computational modelling carried out here.

Geometry optimisation. Solid state geometry optimisations were carried out on the ambient pressure and three high pressure structures (1.77, 3.48 and 5.93 GPa) using the X-ray single crystal structures as input geometries. Full optimisation was performed using CASTEP18 with the PBE DFT functional, and Tkatchenko-Scheffler dispersion correction. The basis set was constructed from a linear combination of plane waves expressed at an energy cut-off of 950 eV, which was chosen to ensure an energy convergence of less than 3 meV/atom, along with norm-conserving pseudopotentials. The Brillouin zone was sampled on a Monkhurt-Pack grid of *ca.* 0.05 $Å^{-1}$. Geometry optimisation convergence criteria were as follows: atomic forces < 5.0×10^{-2} eV/Å, change in energy per atom < 2.0×10^{-6} eV/atom, and unit cell stress < 5.0×10^{-3} GPa.

Calculated PES surface scans. Following optimisation of the crystal structure at each external pressure point (0, 1.77, 3.48 and 5.93 GPa), a series of single-point energy calculations were performed for each structure. This was done by manually,

incrementally moving the position of the H along the N1—H bond vector. Single point energy calculations were carried out at each point to obtain the relative energy of each structure. Single point calculations were carried out to because full relaxing the system results in the position of the H atom returning to the minimum along the PES. The resulting potential energy surface scans were then fitted to sixth-order polynomial functions, for which one-dimensional Schrödinger equations were solved to obtain the ground state wavefunctions and expectation values for a deuterium atom residing in each PES surface. In this way a more accurate prediction for the variation in N—D bond lengths could be presented which will eventually be able to be compared to powder neutron diffraction data.

Calculated electronic band structure calculations. These were performed using CRYSTAL17,[29,30] in order to acces the hybrid functional HSE06, which has proven reliable track record in predicting reliable electronic band gaps for molecular materials.[31] The m-6-311G(d) basis set was used with the k-points sampled using a Monkhorst-Pack net of 8 x 8 x 8 grid. Convergence criteria were set on root-mean-square and absolute values for both the graident and estimated atomic displacements at 3×10^{-4} a.u. and 1.2×10^{-3} a.u., respectively ,with the energy convergence between successive cycles required to be below 10^{-7} a.u. In the ambient structures all lattice parameters and atomic poisitions were allowed to relax. For the high pressure structure, as CRYSTAL17 does not permit optimisation in the pressence of an external pressure, the geometry optimisation was performed as atom-only.

Predicted impact sensitivities. Phonon calculations were carried out at the gamma-point only, using density functional perturbation theory (DFTP) as implemented in CASTEP. The acoustic sum rule was applied analytically.

Assignment of Ω_{max} was performed by tracking the displacement of the centre of mass at each eigenvector, which allows for the identification of lattice modes and molecular modes, backed up with a visual study of the calculated eigenvectors for the vibrational modes. When the average CoM displacement fell below 10 % of the maximum CoM displacement, the phonon motion was considered to be more localised than delocalised. This allows the point where the change in behaviour from phonon bath to localised molecular vibrations to be identified. The shock temperature, that is the superheated phonon quasi-temperature which follows immediately after impact is obtained by ratio of the bulk heat capacity to the phonon bath heat capacity, C_{tot}/C_{ph}. To allow direct comparison of the vibrational up-pumping results, normalisation of the phonon DoS by the unit cell volume is carried out, along with the number of vibrational modes in the phonon bath region 6(Z+Y) where Z is the number of molecules in the unit cell and Y is the number of amalgamated modes in the phonon bath, per molecule.

4.3. Results and Discussion

4.3.1. Crystal structure and high pressure behaviour of NTO.BIPY

The crystal structure of NTO.BIPY at ambient pressure condition was solved and refined in the monoclinic space group $P2_1/n$, with unit cell parameters a = 7.931 Å, b = 5.791 Å, c = 27.81 Å, and β = 95.35°. The asymmetric unit comprises a single NTO and BIPY unit, connected via two hydrogen bonds. The first, N1···N3' is associated with the acidic proton on NTO (Figure 4.1(a)). Difference Fourier maps unambiguously assigned this hydrogen atom to the NTO, thereby defining the structure at ambient pressure as a co-crystal. The second, N2-H···N4' leads to the formation of parallel stacks of alternating herringbone planes (Figure 4.1(b)).

(a)

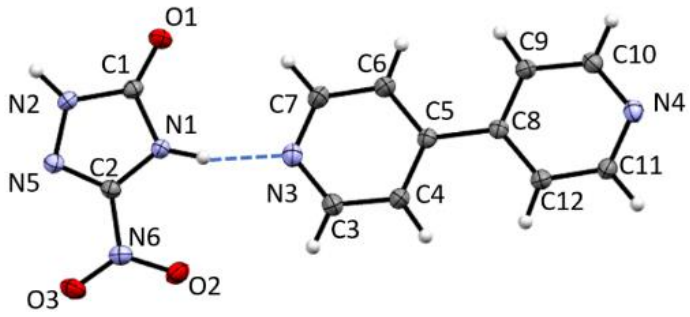

(b)

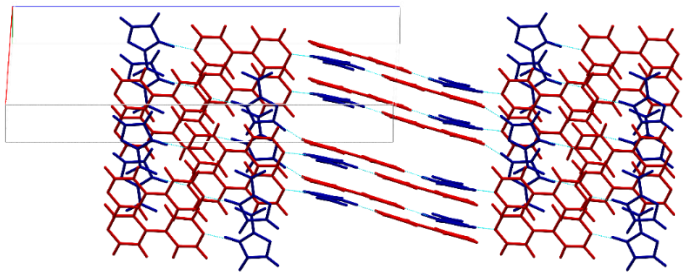

Figure 4.1. (a) The molecular structure of the asymmetric unit and (b) crystal packing of NTO.BIPY (NTO in blue, BIPY in red), as determined at ambient pressure by single crystal X-ray diffraction.

Non-covalent interaction (NCI) plots were obtained, in an effort to quantify the nature of the hydrogen bond interactions formed in NTO.BIPY versus the parent NTO (alpha-polymorph) form (see Figure 4.2). These plots characterise stationary points in the electron density associated with intermolecular (non-contact) interactions, and are typically plotted in two-dimensions as the reduced density gradient vs the sign of the λ_2 parameter of the electron density; values approaching zero in the former indicate the occurrence of a stationary point, and the value of the latter characterises the nature of the interaction associated with that stationary point. It can therefore be seen that the hydrogen bonds formed in NTO.BIPY are considerably stronger (occurring at more negative $\lambda_2\rho$ values, *ca.* -0.65 and -0.55 a.u.) compared to α-NTO

(*ca*. -0.4 and -0.25 a.u.). The pi-pi stacking dispersion interactions (attractive, shown up to *ca*. -0.1 $\lambda_2\rho$ and repulsive, shown up to *ca*. 0.1 $\lambda_2\rho$) appear slightly more pronounced in α-NTO compared to NTO.BIPY. The same information can be portrayed in three dimensions as an isosurface plot (expressed at the reduced electron gradient, *s* = 0.5 a.u., attractive interactions only, *i.e.* negative $\lambda_2\rho$ values), where the stronger N-H···N interactions are readily expressed in NTO.BIPY as dark blue discs (vs teal-coloured discs in α-NTO).

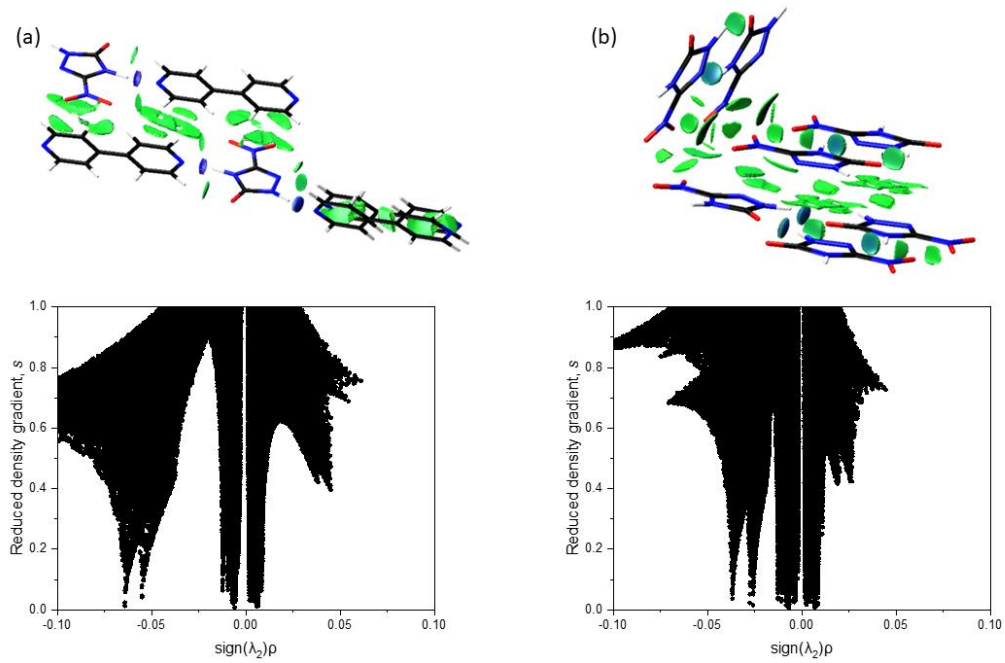

Figure 4.2. 3D and 2D NCI plots of (a) NTO.BIPY and (b) α-NTO, derived from plane-wave DFT generated electron density surfaces. The 3D isosurfaces are expressed at *s* = 0.5 a.u., -0.1 (blue) < ρ < 0 (green) a.u.)

4.3.2. Response to pressure

Single crystal X-ray diffraction shows that upon hydrostatic pressure, a gradual change in crystal colour is observed, from colourless at ambient pressure, to bright yellow at 2.85 GPa, to orange at 7.74 GPa. Here striations are observed on the crystal surface, and the X-ray diffraction pattern shows severe twinning. The

complexity of the data obtained meant that characterisation of this form was unfortunately not possible at the current time. Upon decompression, the crystal reverted to colourless (Figure 4.3).

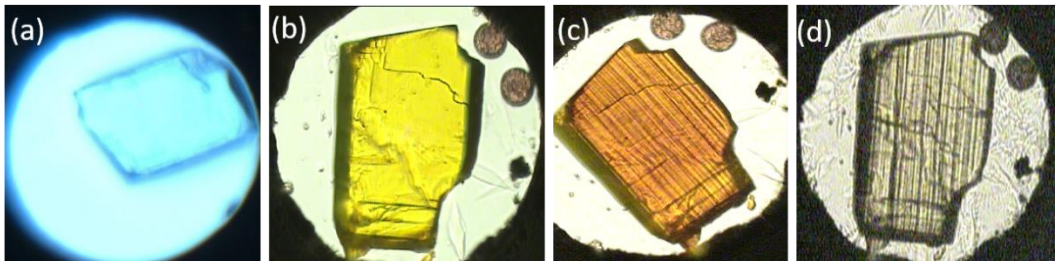

Figure 4.3. Photographs of colour changes of a crystal of NTO.BIPY in the DAC at different pressure conditions: (a) ambient (colourless), (b) 2.85 GPa (yellow), (c) 7.74 GPa (orange), and (d) ambient after decompression (colourless). The ruby spheres, used for pressure calibration, are visible top right.

While a high pressure single crystal X-ray diffraction study cannot inform directly on the position of a hydrogen atom within a hydrogen bond, it can chart the bond compression with respect to the heavy atom positions. This is shown for the two hydrogen bonds in NTO.BIPY in Figure 4.4. It is interesting to note that N1-H···N3 decreases significantly more than N2-H···N4', despite being the shorter of the two interactions. No discontinuities are observed in either trend, suggesting that the colour change observed with the phase transition is not associated with significant changes in hydrogen bond interactions. This is important, as it would otherwise be tempting to attribute the colour changes to single and double proton transfer to BIPY, as similar colour changes were observed in the crystal structure formed between BIPY and squaric acid.[32]

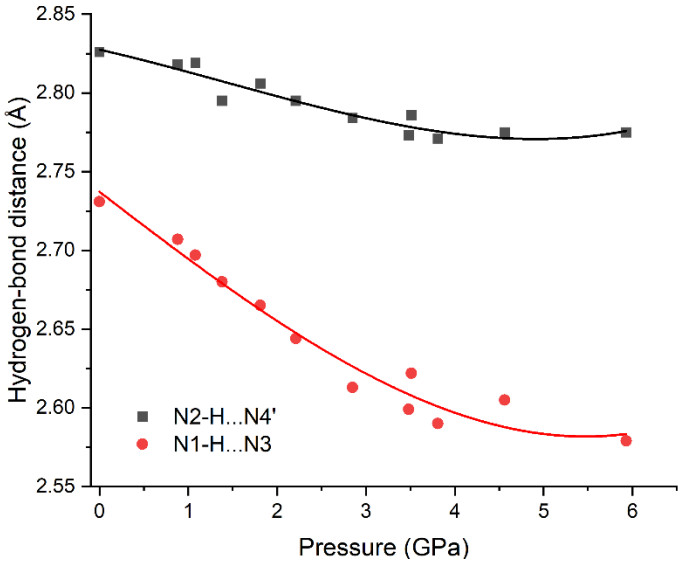

Figure 4.4. Plots of distance of hydrogen bonds upon compression up to 5.93 GPa. Lines are derived from 2nd order polynomial fits.

4.3.3. High pressure computational modelling

Geometry optimisations were performed on the ambient pressure and three high pressure structures (1.77, 3.48 and 5.93 GPa), with input models derived from the experimental single crystal X-ray diffraction crystal structures. For the ambient structure, the hydrogen atom in the N1-H···N3 hydrogen bond remained on the NTO molecule, confirming the ambient pressure X-ray assignment of a co-crystal status. Optimisation of three high pressure structures similarly also showed no proton transfer, suggesting that NTO.BIPY remains as a co-crystal over the pressure range studied.

In an effort to understand the changes in the hydrogen bond potential energy surface in more detail, a series of potential energy surface (PES) scans for the four structures were calculated, with the output shown in Figure 4.5. At lower pressures (0.00 to 3.48 GPa) the PESs present as broad minima at *ca*. 1.1 Å, confirming proton attachment to NTO as the lowest energy structure, while also presenting with a second but diminishingly stable structure at *ca*. 1.55 Å, some 100 kJ mol^{-1} higher in

energy, which corresponds to proton attachment to BIPY. By 5.93 GPa the PES presents as a single well. Note the use of relative energy between structures – all energies are reported as relative to the minimum in the 0.00 GPa structure.

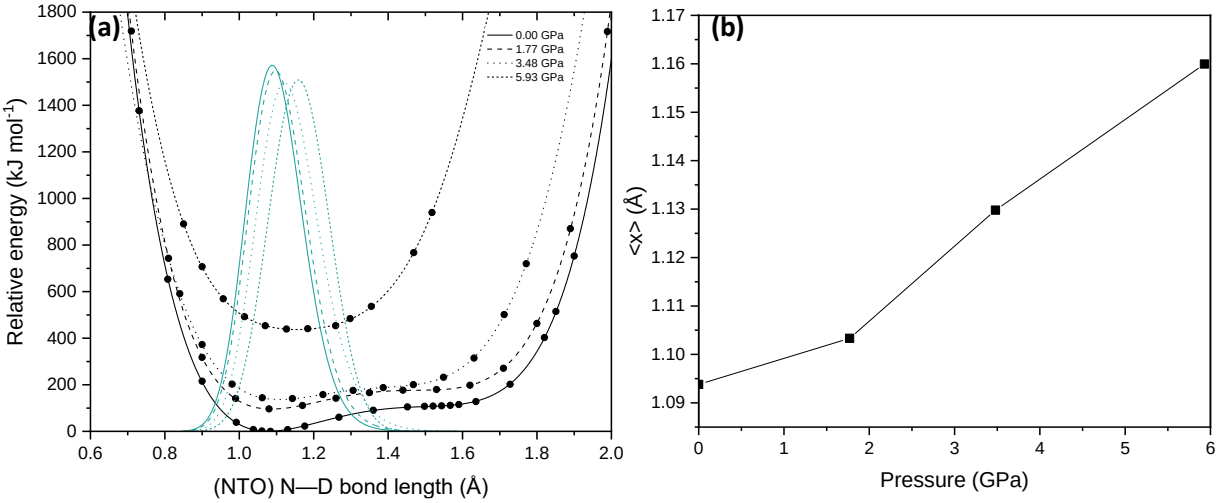

Figure 4.5. (a) Calculated potential energy surfaces for the N1—D···N3 hydrogen bonds in NTO.BIPY as a function of pressure. Data points shown are fitted to a sixth-order polynomial function (black curves), alongside the ground vibrational state expectation values for a deuterium atom located on each PES (cyan curves); (b) N–D expectation values plotted as a function of pressure.

In order to more accurately portray how these PES scans impact on the predicted N–H bond length, calculated single point energies for each surface were fitted to a sixth-order polynomial function and subsequently solved within the one-dimensional Schrödinger equation formalism to locate the ground state wavefunction and associated expectation value for a deuterium atom located on each potential energy surface. Note in this analysis deuterium, instead of hydrogen, was modelled, to present a more comparable prediction for direct comparison against the deuterated sample explored with powder neutron diffraction data. The resulting predicted N–D bond lengths as a function of pressure is shown in Figure 4.5(b) with expectation values of the bonds shown in Table 4.1. With a predicted bond lengthening of ca.

0.07 Å to occupy a position just 0.11 Å away from the mid-point of the N1···N3 bond, NTO.BIPY should be classed as a proton migration system. There are drawbacks to this method, as the movement of the deuterium atom was limited to motion only in the existing 1-dimensional N-D bond vector to simplify the calculations, however in reality at high pressures the movement of the proton could be in up to 3-dimensions. As the movement of the proton was only limited to 1 direction, and calculations were single-point only it is possible that there is an energy minima when the proton lies elsewhere. However, the results presented here still provide sufficient evidence to suggest that at 5.93 GPa there is no possibility of the salt forming, as the PES narrows as such a high pressure. Additionally, work carried out by Mohamed *et.al* [33] suggest that it is unusual for the same close packing of the ions or molecules to be energetically favourable for both a salt and co-crystal. For NTO.BIPY both the experiment ambient and high pressure structures exhibit the same packing and so the assignment of NTO.BIPY as a proton migration system is valid.

Table 4.1 N-H bond length minimum from PES (Fig. 4.6(a)) and expectation values from 1D Schrodinger equation fit to PES at increasing pressures.

Pressure (GPa)	**Xmin (Å)**	**<x> (Å)**	**N…N distance (Å)**
0.00	1.0780	1.0938	2.751
1.77	1.0864	1.1033	2.664
3.48	1.1076	1.1298	2.590
5.93	1.1557	1.1600	2.548

NTO.BIPY is therefore unlikely to ever form a salt unless further phase transitions (at high temperatures, or pressures beyond 6 GPa) induce a more significant change in crystal packing arrangement. The well-investigated proton migration system of urea-phosphoric acid has the proton position moving along a N···O hydrogen bond by 0.03 - 0.05 Å at elevated temperatures, comparable to the changes seen here.[34,35]

With the computational modelling therefore appearing to rule out the possibility of proton transfer with increasing pressure, another factor must be responsible for the clear to yellow colour change observed at high pressure. In order to determine if it can simply be attributed to unit cell compression, electronic band structures were calculated for the ambient and 5.93 GPa structures. The results are presented in Figure 4.6, alongside the partial density of states and associated Brillouin zone k-point paths.

The first point to denote from the electronic band structure plots are the values of the direct (i.e. vertical) band gaps measured at the Γ-point, which reduces from 3.09 eV for the ambient pressure structure to 2.87 eV for the high pressure structure. The ambient pressure band gap for NTO.BIPY is similar to the white pigment ZnO (3.3 eV),[36] while the high pressure band gap is in line with values reported for yellow molecular crystals using the same hybrid DFT functional (2.5-2.8 eV for the yellow forms of the highly polymorphic organic molecule known as 'ROY').[31] Thus it is likely that this colour change can be directly attributed to compression of the unit cell, and an associated electronic transition between the frontier highest occupied crystalline orbitals (HOCOs) and the lowest unoccupied crystalline orbitals (LUCOs), both of which are located on the NTO (as demonstrated by the partial density of states plots in Figure 7). In the 5.93 GPa structure the HOCOs are now dominated by contributions from the nitrogen atoms on the BIPY, while the LUCOs remain on NTO,

unchanged from their ambient pressure character. From the electronic band structure diagrams, it is apparent that the narrowing of the electronic band gap for the high pressure structure arises due to an increase in energy dispersion with respect to the k-point paths $\Gamma \rightarrow$ Z, D $\rightarrow$ B, A $\rightarrow$ E and C $\rightarrow$ Y. These k-point vectors all coincide with the unit cell b-vector, which partially aligns with the herringbone pi-pi stacking direction in both phases of NTO.BIPY.

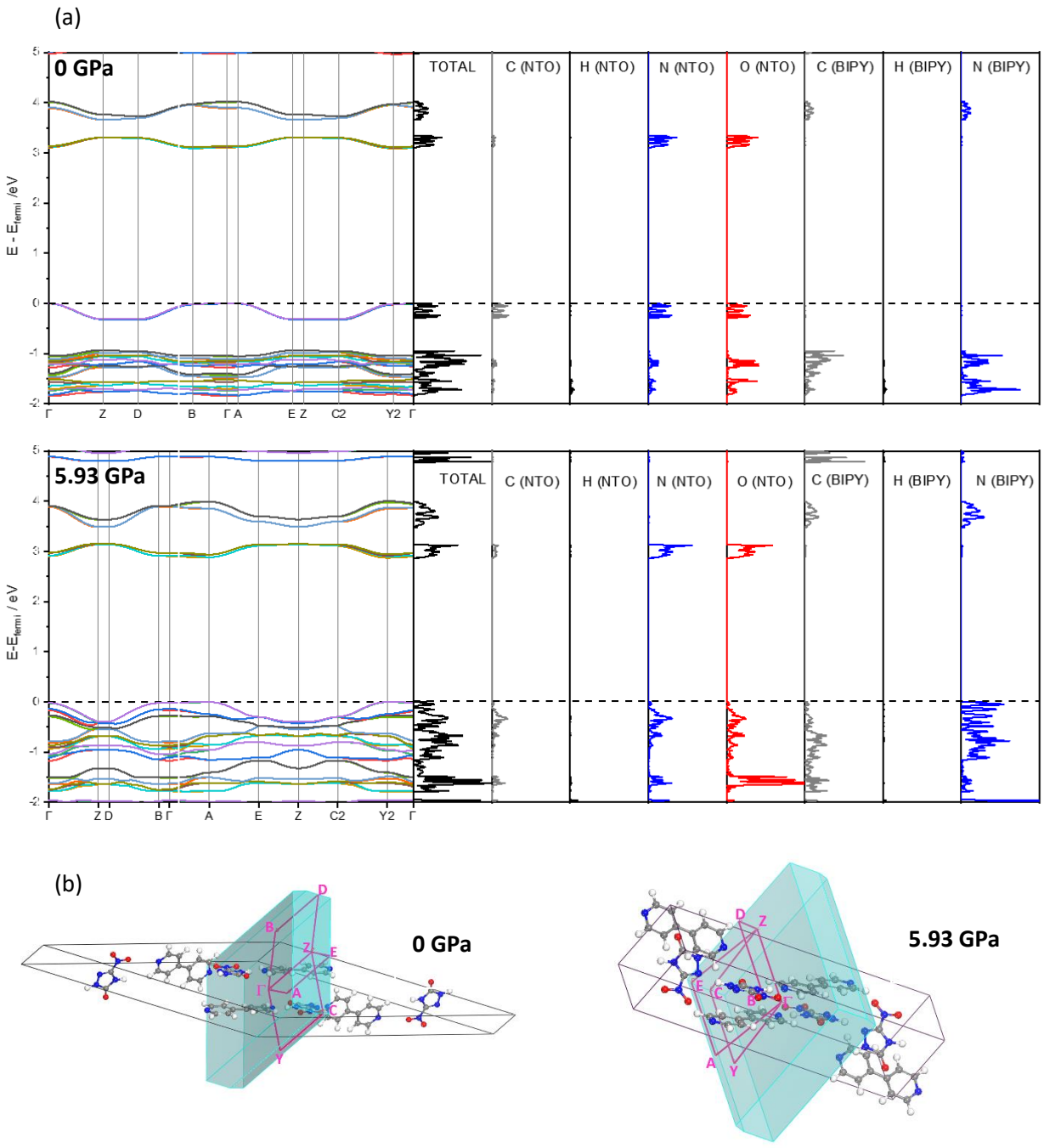

Figure 4.6. (a) Calculated electronic band structures for NTO.BIPY, alongside partial density of states at 0.00 GPa (top) and 5.93 GPa(bottom). The dotted black line shows the Fermi level, set to 0 eV in each case (absolute E_{fermi} values: 0 GPa = -6.02, 5.93 GPa =-5.61 eV. (b) Visualisation of the Brillouin zone paths projected onto the real-space unit cells.

4.3.4. Calculation of detonation parameters

With the structural characterisation of the NTO.BIPY co-crystal complete, it is now possible to consider its predicted energetic properties, alongside those of the parent

energetic NTO, for direct comparison. The heat of formation, ΔH_f (solid), of NTO.BIPY was calculated using the proposed method described in Chapter 3 for co-crystals – with the lattice enthalpy of the co-crystal being calculated using DFT-D and gas phase heat of formation being calculated using PM7 (Table 4.2). Meanwhile ΔH_f (solid) of NTO was calculated using the method adapted by Byrd *et. al* [37] (highlighted in Chapter 3). The heat of formation (solid) of NTO.BIPY is more positive than for NTO, this is due to the introduction of BIPY which has a highly positive gaseous heat of formation, which increases the ΔH_f of NTO.BIPY (Tables 4.2 and 4.3). Detonation pressure, temperature and velocity are key parameters used to assess the performance of EMs. For NTO.BIPY, this drops across the board compared to NTO. This was expected, as the energetic component in the system has essentially been diluted by co-crystallisation with BIPY. Moreover, the crystal density of NTO.BIPY is less than NTO, even in the high pressure polymorph, which further impedes the energetic performance.[38] It should also be noted that the oxygen balance for NTO.BIPY is very low, meaning that successful initiation would require the addition of an oxidiser.

Table 4.2. Parameters used to calculate ΔH_f (solid) of NTO.BIPY and NTO

Structure	$\Delta H_{f\,(gas)}$ **/ kJmol^{-1}**	ΔH_{sub} **/ kJmol^{-1}**	$\Delta H_{Lattice}$ **/ kJmol^{-1}**
NTO	91.3	78.8	-
BIPY	267.9	-	-
NTO.BIPY	-	-	-263.8

Thus for NTO.BIPY, at least, co-crystallisation between an EM/non-EM, while giving rise to an interesting system from a structural chemistry perspective, has severely affected its energetic performance. Detonation performance of NTO.BIPY are comparable to that of unsymmetrical dimethylhydrazine (UDMH), which is used as a

rocket propellant. For comparison UDMH has a detonation pressure = 7.5 GPa, detonation temperature = 1713 K and detonation velocity = 6076 m s^{-1}.[39] EXPLO5 evaluation of the high pressure structure (5.93 GPa) of NTO.BIPY suggest that the detonation pressure and detonation velocity increase when the density of the material increases. This is in accordance with knowing that these parameters scale with density. Interestingly, the predicted detonation temperature high pressure NTO.BIPY is less than it's ambient condition structure. Similar trends in detonation temperature were reported for different densities of pentaerythritol tetranitrate calculated using EXPLO5, showing that detonation temperature does not have the same dependence upon density as detonation pressure or velocity.[40]

Table 4.3. Energetic properties of NTO and NTO.BIPY. ΔH_f (solid) calculated following the procedure described in Chapter 3.

EM	ΔH_f (solid) / kJmol^{-1}	Density / gcm^{-3}	Detonation Pressure / GPa	Detonation Temperature / K	Detonation Velocity /m s^{-1}	Oxygen Balance / %
α-NTO	-55.81	1.91	30.6	3050	8522	-24.6
NTO.BIPY 0.00 GPa	95.37	1.49	10.4	1828	5885	-145
NTO.BIPY 5.93 GPa	95.37	1.89	16.5	1670	6978	-145

4.3.5. Impact sensitivity calculations.

It is now important to consider how introducing BIPY into the crystal lattice affects the propensity for NTO to initiate by mechanical impact. Full details on our impact sensitivity prediction model are available elsewhere,[27,28,41] but are summarised briefly here. The model is based on the principles of vibrational up-pumping,

whereby the shock wave energy following mechanical impact is deposited into the lattice acoustic vibrations. The energy is then rapidly equilibrated across the phonon bath modes, which are defined by an upper limit of Ω_{max}. These low energy modes reach temperatures on the order of thousands of degrees (denoted T_{shock}), and their heightened vibrational excitation creates new higher energy vibrational states, termed the 2phonDoS, through a number of phonon scattering pathways. As a result the shock wave energy is vibrationally up-pumped into the molecular modes lying in the 1-3 Ω_{max} region. Heightened population of these vibrational modes introduces molecular strain,[42] which subsequently leads to initiation of the material. Thus, our impact sensitivity prediction model takes the phonon density of states (DoS), calculated for the optimised crystal structure using PW-DFT, as input data, and generates its corresponding 2phonDoS. Integrating the projection of the 2phonDoS with the underlying DoS curve provides a quantitative prediction of the ability of the vibrational modes inherent in the crystal lattice to trap shock wave energy into the molecular vibrations. This is the metric we report for relative predicted impact sensitivity.

Prior to performing the up-pumping analysis, the calculated DoS for NTO.BIPY was investigated in more detail in order to better understand the nature of the vibrational motions to be included in the impact sensitivity prediction process. For instance, while it is reasonable to expect that the phonon bath modes will be delocalised across both the NTO and BIPY molecules (i.e. inseparable mixed modes, and therefore all included in the up-pumping process) the same may or may not hold across the up-pumping window. To that end, partial DoS plots were constructed, where each eigenvector was interrogated in turn, to assign the mode as either entirely NTO-based, entirely BIPY-based, or mixed (comprising motions from both

molecular entities). The outcome is shown in Figure 4.7, which shows that all modes are either of mixed character or NTO motion only. Therefore, all modes should be included in the generation of the 2PhonDoS.

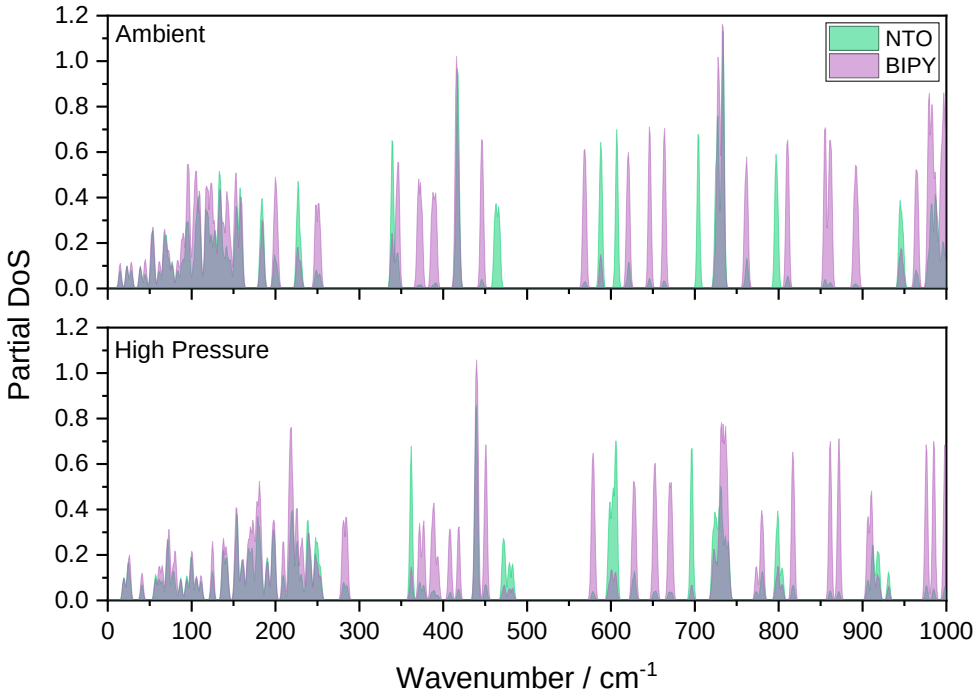

Figure 4.7. Phonon DoS of NTO.BIPY, projected onto the energetic (NTO) and non-energetic (BIPY) components. Overlap of the vibrational modes, i.e. mixed modes are grey.

The top of the phonon bath regions (denoted by Ω_{max}) were assigned in each instance by tracking the change in centre of mass across each of the eigenvectors, with a significant drop indicating the cross over in mode behaviour from delocalised (i.e. mostly translational/rotational based) to localised (i.e. molecular-based) had occurred (Figure 4.8.)

Parameters used to calculate the impact sensitivity of NTO.BIPY are shown in table 4.4 along with the calculated up-pumped density which is the result of integrating the portion of the 2phonDoS which overlaps the underlying DOS in the 1-3Ω_{max} region.

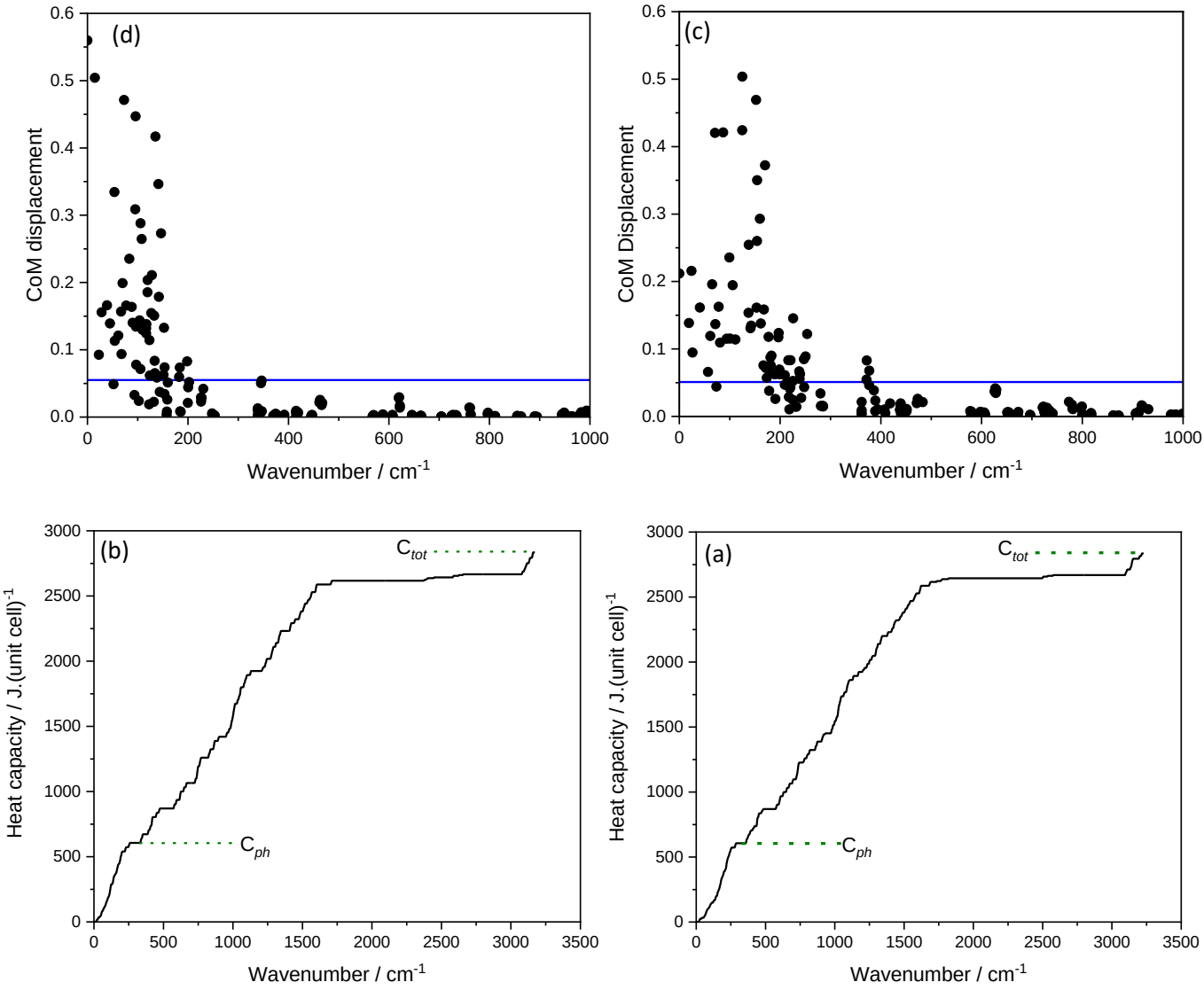

Figure 4.8. Average centre of mass displacement for NTO and BIPY molecules in (a) ambient and (b) 5.93 GPa. Blue horizonal lines denote 10% of maximum displacement. (c-d) show the cumulative heat capacities of the NTO.BIPY ambient and at 5.93 GPa respectively. . Values of C_{ph} and C_{tot} are marked by horizontal dashed lines.

Considering α-NTO first, the 2phonDoS/DoS projection yields 11.2 arb units, which has previously been demonstated to correctly place α-NTO in the following impact sensitivity order series: HNB > ε-CL-20 > β-HMX > o-TNT > α-FOX-7 > α-NTO > TATB.

Energetic Material	Ω_{max} / cm^{-1}	Z(6+Y)	T_{shock} / K	Up-pumped density ($x10^3$/Z a.u.)
α-NTO	204	64	2642	11.2
NTO.BIPY (0.00 GPa)	266	72	3066	42.6
NTO.BIPY (5.93 GPa)	294	72	3066	68.8

Table 4.4. Parameters used to calculate the impact sensitivities of NTO and NTO.BIPY.

The 2phonDoS/DoS projection of ambient NTO.BIPY gives 42.6 arb units, meaning that NTO.BIPY is predicted to be more senstive than NTO. Likewise, the high pressure compressed form gives an up-pumped metric of 68.8 arb units, indicating greater senstivity still.

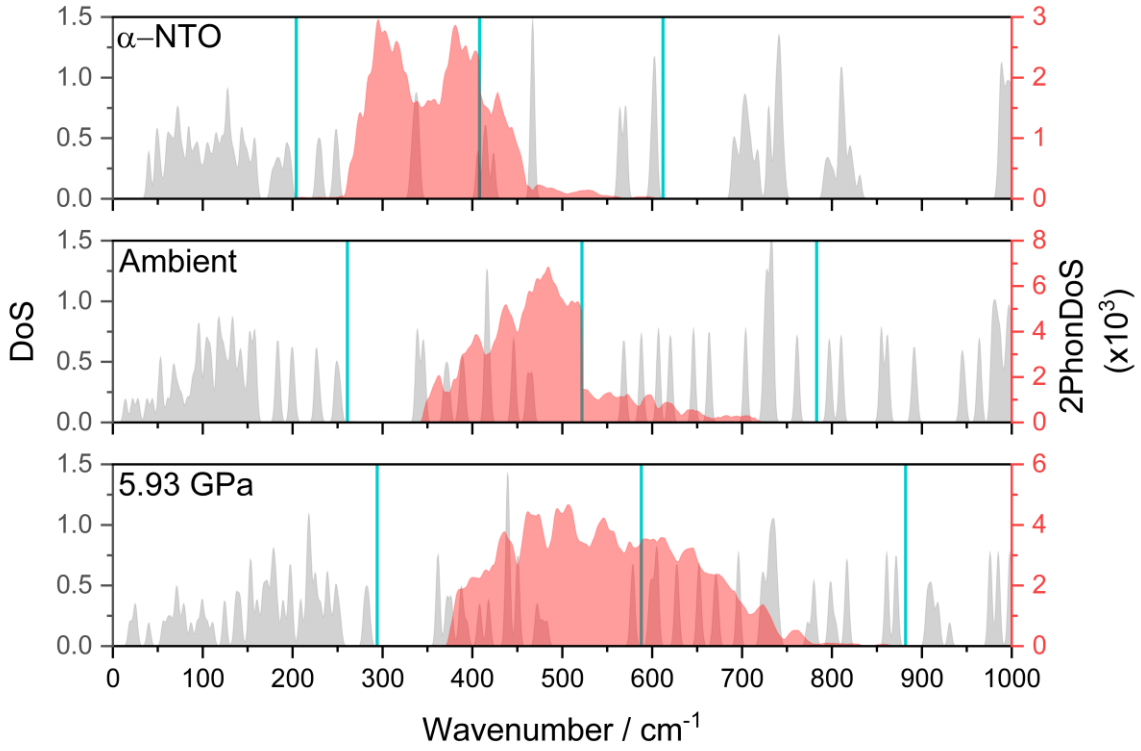

Figure 4.9. Phonon DoS (grey) calculated by PW-DFT, and corresponding 2phonDoS (red) for NTO (top), NTO.BIPY at ambient conditions and at 5.93 GPa (bottom).The blue vertical lines represent the 1-3 Ω_{max} boundaries.

The predicted impact sensitivity ordering is shown graphically in Figure 4.10. Noting the absence of any experimental impact sensitivity testing means that the data points have been positioned to follow the prediction curve; in this way it is predicted that co-crystalising NTO with BIPY sensitisies NTO to mechanical initiation, presenting an impact sensitivity more akin to TNT. Under compression it is predicted that the response to impact to increase, but not to such a large amount that the high pressure structure is more comparable to another EM.

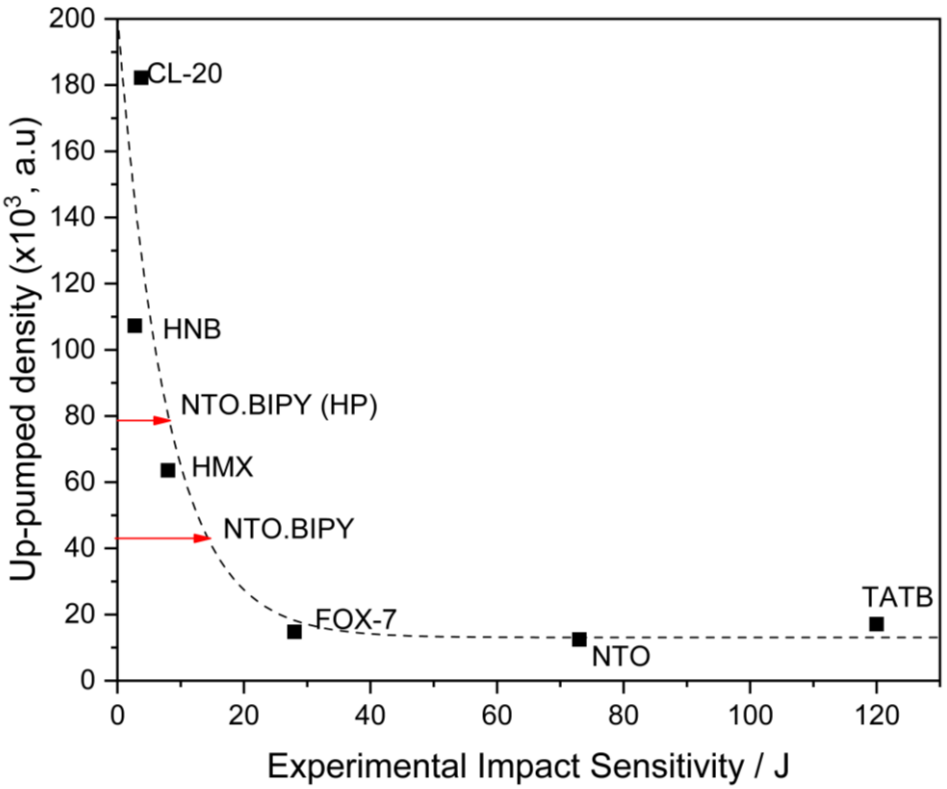

Figure 4.10. Predicted up-pumped density of characterised EMs vs. their experiemental impact sensitivities, calculated using the same computational model.[28] Red arrows show the predicted positions of NTO.BIPY and the high pressure species, NTO.BIPY(HP).

With the up-pumping model suggesting that the NTO.BIPY is more sensitive to mechanical impact than the parent NTO molecule, the next step is to understand better why this occurs. For this we turn back to the DoS/2PhonDoS plots presented

in Figure 4.9. In particular, there are two regions of the DoS plot that require further investigation. The first is the phonon bath region, which can be quantified according to

$$Phonon\ bath\ DoS = {g(\omega)_{ph}}\Big/{(g(\omega)_T \times \Omega_{max})}$$

Where $g(\omega)_{ph}$ is the integral of the DoS up to Ω_{max} and $g(\omega)_T$ is the integration across the total DoS plot. This yields values of 1.15, 0.743 and 0.668 $\times$ 10^{-3} arb units for NTO, NTO.BIPY (ambient P) and NTO.BIPY (high P), respectively which doesn't show any correlation between the density of phonon bath modes and predicted impact sensitivity. For the compressed form the phonon bath region entends ca. 30 cm^{-1} beyond that of the ambient pressure structure, although visual inspection of the eigenvectors at the top of the phonon bath for both structures confirm that the same modes are present for each structure. The blue-shift in wavenumbers for the compressed structure can therefore be attributed to a mode hardening effect. The resulting increase in Ω_{max} also creates the broader doorway region, which can similarly be quantified according to:

$$Doorway\ DoS = {g(\omega)_D}\Big/{(g(\omega)_T \times \Omega_{max})}$$

Where $g(\omega)_D$ is the integral of the DoS between 1-2 Ω_{max} and $g(\omega)_T$ is the integration across the total DoS plot. This results in values of 3.00, 3.26 and 3.30 $\times$ 10^{-4} arb units for NTO, NTO.BIPY (ambient P) and NTO.BIPY (high P), respectively, which follows the trend in overall predicted IS. The doorway states increase the available scattering pathways for phonon-phonon scattering, as well as providing more states to capture the 2PhonDoS, and so it directly follows that more doorway modes should correlate directly with an increase in sensitivity to mechanical impact

and has an overall bigger effect on predicted impact sensitivity than the density of phonon bath modes. Finally, it should be noted that the compressed structure presents a broader up-pumping window, with more of the 2PhonDoS being captured by higher wavenumber vibrations.

4.4. Conclusions

A co-crystal of energetic NTO and non-energetic 4,4’-bipyridine (BIPY) has been synthesised. Upon formation of the co-crystal, the strength of the hydrogen bonds involving NTO increase. High pressure single X-ray driffraction studies show that NTO.BIPY undergoes colour change from colourless to yellow. To further understand the structure of the material upon phase change, 1D Schrodinger equations were fit to the potential energy surface along the N-H···N vector which confirm that the system is a proton migration system. Band gap calculations also show that the colour change is due to narrowing of the band gap due to compression of the material. Finally, the energetic performance of NTO.BIPY was compared to NTO. Our vibrational up-pumping model was used to predict the relative impact sensitivity, and shows that the sensitivity to impact of NTO.BIPY is increased when compared to NTO as more vibrational pathways to initiation are introduced to the crystal lattice through the introduction of BIPY. This is the second instance of a co-crystal of an energetic and energetic resulting in a material which is more sensitive than its parent EM.

One key area for future work for investigating this co-crystal and its performance at high pressures is to carry out neutron diffraction characterisation on the structure. This will ensure the confirmation of the co-crystal acting as a proton migration system at high pressures

References

1 J. C. Bennion and A. J. Matzger, Development and Evolution of Energetic Cocrystals, *Acc. Chem. Res.*, 2021, **54**, 1699–1710.

2 S. R. Kennedy and C. R. Pulham, in *Co-crystals: Preparation, Characterization and Applications Edited*, eds. B. Aakeroy and A. Sinha, The Royal Society of Chemistry, 2018, pp. 231–264.

3 O. Bolton and A. J. Matzger, Improved Stability and Smart-Material Functionality Realized in an Energetic Cocrystal, *Angew. Chemie*, 2011, **123**, 9122–9125.

4 U. R. Nair, R. Sivabalan, G. M. Gore, M. Geetha, S. N. Asthana and H. Singh, Hexanitrohexaazaisowurtzitane (CL-20) and CL-20-Based Formulations (Review), *Transl. from Fiz. Goreniya i Vzryva*, 2005, **41**, 3–16.

5 O. Bolton, L. R. Simke, P. F. Pagoria and A. J. Matzger, High power explosive with good sensitivity: A 2:1 cocrystal of CL-20:HMX, *Cryst. Growth Des.*, 2012, **12**, 4311–4314.

6 M. K. Bellas and A. J. Matzger, Achieving Balanced Energetics through Cocrystallization, *Angew. Chem. Int. Ed. Engl.*, 2019, **58**, 17185–17188.

7 J. C. Bennion, A. McBain, S. F. Son and A. J. Matzger, Design and synthesis of a series of nitrogen-rich energetic cocrystals of 5,5′-dinitro-2 H,2 H′-3,3′-bi-1,2,4-triazole (DNBT), *Cryst. Growth Des.*, 2015, **15**, 2545–2549.

8 S. R. Anderson, P. Dubé, M. Krawiec, J. S. Salan, D. J. a. Ende and P. Samuels, Promising CL-20-Based Energetic Material by Cocrystallization, *Propellants, Explos. Pyrotech.*, 2016, **41**, 783–788.

9 J. C. Bennion, Z. R. Siddiqi and A. J. Matzger, A melt castable energetic cocrystal, *Chem. Commun.*, 2017, **53**, 6065–6068.

10 Y. Wang, Z. Yang, H. Li, X. Zhou, Q. Zhang, J. Wang and Y. Liu, A Novel Cocrystal Explosive of HNIW with Good Comprehensive Properties, *Propellants, Explos. Pyrotech.*, 2014, **39**, 590–596.

11 J. C. Bennion, L. Vogt, M. E. Tuckerman and A. J. Matzger, Isostructural Cocrystals of 1,3,5-Trinitrobenzene Assembled by Halogen Bonding, *Cryst. Growth Des.*, 2016, **16**, 4688–4693.

12 K. B. Landenberger, O. Bolton and A. J. Matzger, Two Isostructural Explosive Cocrystals with Significantly Different Thermodynamic Stabilities, *Angew. Chemie Int. Ed.*, 2013, **52**, 6468–6471.

13 S. I. Bozkuş, K. S. Hope, B. Yüksel, N. Atçeken, H. Nazır, O. Atakol and N. Şen, Characterization and properties of a novel energetic Co-crystal formed between 2,4,6-Trinitrophenol and 9-Bromoanthracene, *J. Mol. Struct.*, 2019, **1192**, 145–153.

14 K. B. Landenberger, O. Bolton and A. J. Matzger, Energetic-energetic cocrystals of diacetone diperoxide (DADP): Dramatic and divergent sensitivity modifications via cocrystallization, *J. Am. Chem. Soc.*, 2015, **137**, 5074–5079.

15 N. Qiao, M. Li, W. Schlindwein, N. Malek, A. Davies and G. Trappitt, Pharmaceutical cocrystals: An overview, *Int. J. Pharm.*, 2011, **419**, 1–11.

16 K. Lee, L. B. Chapman and M. D. Cobura, 3-Nitro-1,2,4-triazol-5-one, a less sensitive explosive, *J. Energ. Mater.*, 1987, **5**, 27–33.

17 D. A. Pillard, W. S. Eck, M. S. Johnson and S. Packard, Effects of 3-Nitro-1,2,4-triazol-5-one on Survival, Growth and Metamorphosis in the Northern Leopard Frog, Lithobates pipiens, *Ecotoxicology*, 2017, **26**, 1170–1180.

18 G. Singh and S. Prem Felix, Studies on energetic compounds: 25. An overview of preparation, thermolysis and applications of the salts of 5-nitro-2,4-dihydro-3H-1,2,4-triazol-3-one (NTO), *J. Hazard. Mater.*, 2002, **90**, 1–17.

19 J. G. Speight, *Lange's Handbook of Chemistry, 17th Edition*, New York: McGraw-Hill Education, 2017.

20 A. J. Cruz-Cabeza, Acid–base crystalline complexes and the pKa rule, *CrystEngComm*, 2012, **14**, 6362–6365.

21 N. Issa, P. G. Karamertzanis, G. W. A. Welch and S. L. Price, Can the formation of pharmaceutical cocrystals be computationally predicted? I. Comparison of lattice energies, *Cryst. Growth Des.*, 2009, **9**, 442–453.

22 C. R. Taylor and G. M. Day, Evaluating the Energetic Driving Force for Cocrystal Formation, *Cryst. Growth Des.*, 2018, **18**, 892–904.

23 S. Mohamed, D. A. Tocher, M. Vickers, P. G. Karamertzanis and S. L. Price, Salt or cocrystal? A new series of crystal structures formed from simple pyridines and carboxylic acids, *Cryst. Growth Des.*, 2009, **9**, 2881–2889.

24 F. P. A. Fabbiani and C. R. Pulham, High-pressure studies of pharmaceutical compounds and energetic materials, *Chem. Soc. Rev.*, 2006, **35**, 932–942.

25 A. A. L. Michalchuk, S. Rudić, C. R. Pulham and C. A. Morrison, Predicting the

impact sensitivity of a polymorphic high explosive: the curious case of FOX-7, *Chem. Commun.*, 2021, **57**, 11213–11216.

26 A. A. L. Michalchuk, P. T. Fincham, P. Portius, C. R. Pulham and C. A. Morrison, A Pathway to the Athermal Impact Initiation of Energetic Azides, *J. Phys. Chem. C*, 2018, **122**, 19395–19408.

27 A. A. L. Michalchuk, M. Trestman, S. Rudić, P. Portius, P. T. Fincham, C. R. Pulham and C. A. Morrison, Predicting the reactivity of energetic materials: An: ab initio multi-phonon approach, *J. Mater. Chem. A*, 2019, **7**, 19539–19553.

28 A. A. L. Michalchuk, J. Hemingway and C. A. Morrison, Predicting the impact sensitivities of energetic materials through zone-center phonon up-pumping, *J. Chem. Phys.*, 2021, **154**, 1–11.

29 R. Dovesi, V. R. Saunders, C. Roetti, R. Orlando, C. M. Zicovich-Wilson, F. Pascale, B. Civalleri, K. Doll, N. M. Harrison, I. J. Bush, P. D'Arco, M. Llunell, M. Causa, Y. Noel, L. Maschio, A. Erba, M. Rerat and S. Casassa, CRYSTAL17 User's Manual (University of Torino, Torino, 2017).

30 R. Dovesi, A. Erba, R. Orlando, C. M. Zicovich-Wilson, B. Civalleri, L. Maschio, M. Rérat, S. Casassa, J. Baima, S. Salustro and B. Kirtman, Quantum-mechanical condensed matter simulations with CRYSTAL, *Wiley Interdiscip. Rev. Comput. Mol. Sci.*, 2018, **8**, 1–36.

31 L. R. Warren, E. McGowan, M. Renton, C. A. Morrison and N. P. Funnell, Direct evidence for distinct colour origins in ROY polymorphs, *Chem. Sci.*, 2021, **12**, 12711–12718.

32 D. M. S. Martins, D. S. Middlemiss, C. R. Pulham, C. C. Wilson, M. T. Weller,

P. F. Henry, N. Shankland, K. Shankland, W. G. Marshall, R. M. Ibberson, K. Knight, S. Moggach, M. Brunelli and C. A. Morrison, Temperature- and pressure-induced proton transfer in the 1:1 adduct formed between squaric acid and 4,4-bipyridine, *J. Am. Chem. Soc.*, 2009, **131**, 3884–3893.

33 S. Mohamed, D. A. Tocher and S. L. Price, Computational prediction of salt and cocrystal structures—Does a proton position matter?, *Int. J. Pharm.*, 2011, **418**, 187–198.

34 C. C. Wilson, Migration of the proton in the strong O—H...O hydrogen bond in urea-phosphoric acid (1/1), *Acta Crystallogr. Sect. B*, 2001, **57**, 435–439.

35 C. A. Morrison, M. M. Siddick, P. J. Camp and C. C. Wilson, Toward Understanding Mobile Proton Behavior from First Principles Calculation: The Short Hydrogen Bond in Crystalline Urea-Phosphoric Acid, *J. Am. Chem. Soc.*, 2005, **127**, 4042–4048.

36 V. Srikant and D. R. Clarke, On the optical band gap of zinc oxide, *J. Appl. Phys.*, 1998, **83**, 5447.

37 E. F. C. Byrd and B. M. Rice, Improved prediction of heats of formation of energetic materials using quantum mechanical calculations, *J. Phys. Chem. A*, 2006, **110**, 1005–1013.

38 J. P. Agrawal, in *High Energy Materials: Propellants, Explosives and Pyrotechnics*, John Wiley & Sons, Ltd, 2010, pp. 1–67.

39 T. M. Klapötke, *Energetic Materials Encyclopedia*, Berlin, Boston: De Gruyter, 2018.

40 M. Sućeska, Calculation of detonation parameters by EXPLO5 computer

program, *Mater. Sci. Forum*, 2004, **465**–**466**, 325–330.

41 D. Herweyer, J. L. Brusso and M. Murugesu, Modern trends in “Green” primary energetic materials, *New J. Chem.*, 2021, **45**, 10150–10159.

42 A. A. L. Michalchuk, S. Rudić, C. R. Pulham and C. A. Morrison, Vibrationally induced metallisation of the energetic azide α-NaN3, *Phys. Chem. Chem. Phys.*, 2018, **20**, 29061–29069.

Chapter 5. Predicting the impact sensitivity of polymorphs

5.1 Introduction

Polymorphism is the phenomena by which a crystalline material can exist in more than one form.[1] An oft-quoted saying by McCrone states that “The number of forms known for a given compound is proportional to the time and money spent in research on that compound”.[2] The implications of polymorphism are important for any materials chemistry application, as any change to the crystal packing environment has the potential to radically alter the resulting material properties. And while the effects have been profoundly appreciated by the pharmaceutical industry,[3] with the variable bioavailability of the HIV-1 drug ritonavir with polymorphic forms being a particularly high profile example,[4] the same claim cannot be levied at the energetics community. However, it is particularly pertinent to this field as new polymorphic forms for compounds are often found when the external variables of temperature and pressure are varied;[4,5] these are highly relevant criteria to consider during the manufacture, handling and deployment of energetic materials. Typically, the difference in lattice energies of polymorphs vary by less than 10 kJ mol^{-1},[5] thus different polymorphic forms are readily accessible at varying conditions.

Polymorphs of the same chemical species typically have different physical properties, including solubility, density, melting point and chemical stability.[3] These properties can all affect performance and can even have legal ramifications.[6] For EMs in particular, the occurrence of polymorphs can be critical in the processing of melt-cast munitions, where the material is melted, poured and subsequently cooled;[7] these are conditions that are ripe for generating new polymorphic forms. Additionally, any defects or cracks that may form during a solid phase change could affect impact sensitivity, as cracks have been shown to aid with the formation of hot-spots which are believed to form in the detonation mechanism of EMs.[8]

To-date the effect that polymorphism has on impact sensitivity (IS) has not been studied in any great detail. While multiple polymorphs have been reported for the

most well characterised EMs, including CL-20,[9,10] HMX,[11–13] NTO,[14,15] FOX-7,[16,17] RDX,[18–21] TNT,[22] DNAN and TATB,[23] less is known about how the performance of these polymorphs differ from one another. The lack of research into the properties of EM polymorphs can be attributed to either metastability issues under testing conditions (as is the case with high pressure/temperature polymorphs) or may be simply due to a lack of urgency, or understanding, from an industrial standpoint. Of note, differences in IS of the β- and δ-polymorphs of HMX have been reported, with the d-polymorph reported as being more sensitive to impact than the β-form.[24] The change in impact sensitivity has been hypothesised to be related to an increase in void space in the δ-polymorph, where molecules adopt a boat conformation, compared to the β-form, where molecules are in a chair conformation. This study highlights that molecular conformational differences and crystal packing differences lead to changes in material properties. Moreover, a recent computational and experimental study of FOX-7 by Michalchuk *et. al.*[25] further highlights the importance of considering polymorphism when carrying out measurements on EMs. Using the same vibrational up-pumping method used in this thesis they predicted that the sensitivity of α-FOX-7 was greater than that of γ-FOX-7. However, subsequent BAM hammer fall tests indicated that the sensitivity of both polymorphic forms was the same. Upon further scrutiny they showed via *ex situ* powder X-ray diffraction measurements that γ-FOX-7 appears to undergo a phase change to α-FOX-7 at mechanical impact values just below that required for initiation. This sets the precedent for further scrutinising the experimental procedures that are used to assess the performance and safety criteria for EMs.

These studies on HMX and FOX-7 show that there is an important relationship between polymorphism and impact sensitivity which has until now been under-researched. Undoubtedly, one of the biggest barriers to furthering the exploration of structure/property relationships of EMs is that many of the polymorphic forms are not stable for testing under the ambient conditions typically deployed in e.g. a BAM fall hammer test. However, that is not to say that these polymorphs will not exist in practical applications of EMs; indeed the explosions caused by EMs can induce shock waves which induce pressures of over 50 GPa and temperatures up to 5500K,[26] which defines a large window on phase-space for relevant polymorphs to be located. Moreover, as shock waves pass through materials at the speed of sound,

this is comparable to the time-scales required to induce first-order phase transitions in solid state materials; for example it has been shown that shock induced detonation occurs on a picosecond timescale[27] while solid phase transitions have been known to occur on a similar timescale.[28] Thus the scenario is presented that EMs may transition to other polymorphic forms on-route to initiation, and those forms may have significantly different energetic and safety metrics. Here, computational modelling has an obvious, and imperative important role to play.

When it comes to the development of a fully computational screening programme for new EMs, there is one glaring gap. From the starting point of a molecular structure, the heat of formation and therefore energetic performance of a material can be predicted, using the method described in Chapter 3. However, to predict the impact sensitivity using the vibrational up-pumping method, a crystal structure is required. To avoid the need to turn to material synthesis and structural characterisation, this gap can now be bridged by implementing crystal structure prediction (CSP).[29–31] Accurate CSP of organic molecular crystals, which typically explores and ranks a large pool of potential crystal structures according to their lattice energies, typically generates a significant list of possible structures that vary in energy by just a few kJ mol^{-1}. More often than not the 'right answer' is somewhere in that list, which pays huge testimony to the enormous challenges presented by structure prediction. However, in terms of predicting the properties of materials, the realistic utilisation of CSP necessitates a workflow where multiple predicted low energy structures must be taken forward.

Within this chapter, the IS of a selection of experimentally characterised polymorphs of the EMs RDX, DNAN, TNT and NTO are predicted using the vibrational up-pumping method, in order to determined how this important performance and safety measure depends upon polymorphic form. This work provides valuable insight into the relationship between structure and property and will highlight how important the consideration of polymorphism is to the EM community.

5.2. Computational Methods

For condensed matter calculations, unless otherwise stated, input geometries were taken from the Cambridge Structural Database.[32] Full geometry optimisation was performed using CASTEP v18[34] with the PBE DFT functional, and Tkatchenko-

Scheffler dispersion correction.[35] The basis set was constructed from a linear combination of plane waves expressed at an energy cut-off of 950 eV, which was chosen to ensure an energy convergence of less than 3 meV/atom, along with norm-conserving pseudopotentials. The Brillouin zone was sampled on a Monkhurt-Pack grid of *ca.* 0.05 $Å^{-1}$. Geometry optimisation convergence criteria were as follows: atomic forces < 1.0×10^{-2} eV/Å, change in energy per atom < 2.0×10^{-6} eV/atom, and unit cell stress < 5.0×10^{-3} GPa and maximum atomic displacement 5×10^{-4} Å. For polymorphs identified at high pressures, hydrostatic pressure was applied during modelling equal to the pressure at which the structure was identified at. The experimental structure for DNAN-II (CSD code: FESNEW12) exhibited disorder across the oxygen atoms of both nitro groups. Before geometry optimisation, two oxygen atoms per nitro group were therefore manually deleted from the input structure in such a way as to retain the overall space group setting.

Non-covalent interaction (NCI) plots shown in section 5.3.2 were produced by generating charge density cube files following geometry optimisation. These were then used to generate the NCI plots using the CRITIC2 code.[36,37]

Phonon calculations were carried out at the gamma-point only, using density functional perturbation theory (DFTP)[38] as implemented in CASTEPV18. The acoustic sum rule was applied analytically. Relative impact sensitivities of the polymorphs were calculated using the method described in Chapter 2.4. Initially Gaussian smearing of 5 cm^{-1} was applied in the generation of the phonon DoS to create a continuous spectrum. Assignment of Ω_{max} was performed by tracking the displacement of the centre of mass for each eigenvector, which allows for the identification of lattice modes and molecular modes, backed up with a visual study of the calculated eigenvectors for the vibrational modes. When the average CoM displacement fell below 10 % of the maximum CoM displacement, the phonon motion was considered to be more localised in nature than delocalised. The shock temperature, that is the superheated phonon quasi-temperature which follows immediately after impact, is obtained from the ratio of the bulk heat capacity to the phonon bath heat capacity, C_{tot}/C_{ph}. To allow direct comparison of the vibrational up-pumping results, normalisation of the phonon DoS by the unit cell volume is carried out, along with the number of vibrational modes in the phonon bath region 6(Z+Y)

where Z is the number of molecules in the unit cell and Y is the number of amalgamated modes in the phonon bath, per molecule.

The results from the geometry optimisation calculations (unit cell parameters) are shown in Table 5.1. Unit cell volume do not change is by more than 5% of experimental values, which has been shown to be a reliable calculation.[39]

Table 5.1. Comparison of the experimental and optimised unit cell parameters of the polymorphs studied in this chapter.

EM	**a / Å**	**b / Å**	**c / Å**	**α / °**	**β / °**	**γ / °**	**V / Å^3**	**ΔV %**
α-RDX (Exp)	11.4425(3)	10.6106(3)	13.1558(4)	90	90	90	1619.18	
α-RDX (Calc)	11.6124	10.8685	13.5028	90	90	90	1704.19	+6.69
α-RDX (Calc)*	10.9414	10.1205	12.9049	90	90	90	1429.01	
β-RDX (Exp)	15.1267(11)	7.4563(6)	14.3719(11)	90	90	90	1643.12	+6.41
β-RDX (Calc)	15.4375	7.6571	14.5923	90	90	90	1724.89	
γ-RDX (Exp)	12.5650(19)	9.4769(6)	10.9297(9)	90	90	90	1301.48	+5.62
γ-RDX (Calc)*	12.8616	9.5927	11.1448	90	90	90	1375.02	
ε-RDX(Exp)	7.5191(41)	11.6430(49)	9.1765(39)	90	90	90	803.35	+4.52
ε-RDX (Calc)	7.6827	12.044	9.0929	90	90	90	841.40	
DNAN-I (Exp)	8.772(2)	12.645(2)	15.429(4)	90	81.89(2)	90	1694.30	-0.59
DNAN-I (Calc)	8.614	12.782	12.404	90	83.30	90	1684.36	
DNAN-I (Calc)†	7.421	12.898	14.309	90	90.31	90	1369.80	
DNAN-II (Exp)	3.980(2)	13.759(7)	15.461(8)	90	90.994(8)	90	846.53	-3.51
DNAN-II (Calc)	3.758	14.126	15.534	90	97.868	90	816.85	
DNAN-III (Exp)	3.908(2)	13.78(1)	15.42(1)	90	95.310(6)	90	826.84	-1.94
DNAN-III (Calc)	3.782	13.886	15.532	90	97.597	90	810.76	
DNAN-VI (Exp)	10.836	17.706	3.460	90	87.55	90	663.30	+1.48
DNAN-VI (Calc)†	10.899	17.733	3.486	90	87.45	90	673.15	
o-TNT(Exp)	14.910(2)	6.0341(18)	19.680(4)	90	90	90	1770.58	
o-TNT (Calc)	15.136	6.0391	20.088	90	90	90	1836.25	+3.71
m-TNT (Exp)	14.9113(1)	6.0340(1)	20.8815(3)	90	110.365(1)	90	1761.37	
m-TNT (Calc)	15.152	6.0394	21.3423	90	109.968	90	1835.64	+4.22
α-NTO (Exp)	5.1233(8)	10.3140(16)	17.998(3)	106.610(2)	97.810(2)	90.130(2)	902.06	
α-NTO (Calc)	5.2437	10.4534	18.1350	106.728	97.810	90.130	942.26	+4.46
β-NTO (Exp)	9.3129(4)	5.4458(2)	9.0261(3)	90	101.464(1)	90	448.637	
β-NTO (Calc)	9.2658	5.5696	9.1873	90	99.8914	90	467.084	+4.41

*Optimised with 3.9 GPa external pressure
†Optimised with 4.5 GPa external pressure

5.3. Results and Discussion

5.3.1. 1,3,5trinito-1,3,5-triazinane (RDX)

1,3,5-trinitro-1,3,5-triazinane, commonly known as hexogen or simply RDX is one of the most commonly used EMs, especially in polymer bonded explosives (PBXs).[40] In addition, RDX is often used as a standard reference material to calibrate drop tower tests.[41] However, a recent report by Doherty *et. al*.[42] highlighted that the experimental determination of IS for RDX gives worryingly variable results. In Doherty's study, seven different laboratories were tasked with measuring the IS for seven different samples of RDX, as purchased from suppliers. The study concluded that the range of reported values for RDX varied from 7 to 20 J.

RDX has four polymorphs logged in the CSD, of which three, α,[43] β[19] and ε[21] have been characterised at ambient conditions, while γ-RDX was obtained through compression of a single crystal and characterised at 3.9 GPa (Figure 5.1).[20] A fifth polymorph, δ, has also been identified by high pressure Raman spectroscopy measurements, but the crystal structure has not yet been characterised.[44] α-RDX is considered to be the stable polymorph which is widely assumed to be present in commercially available RDX.

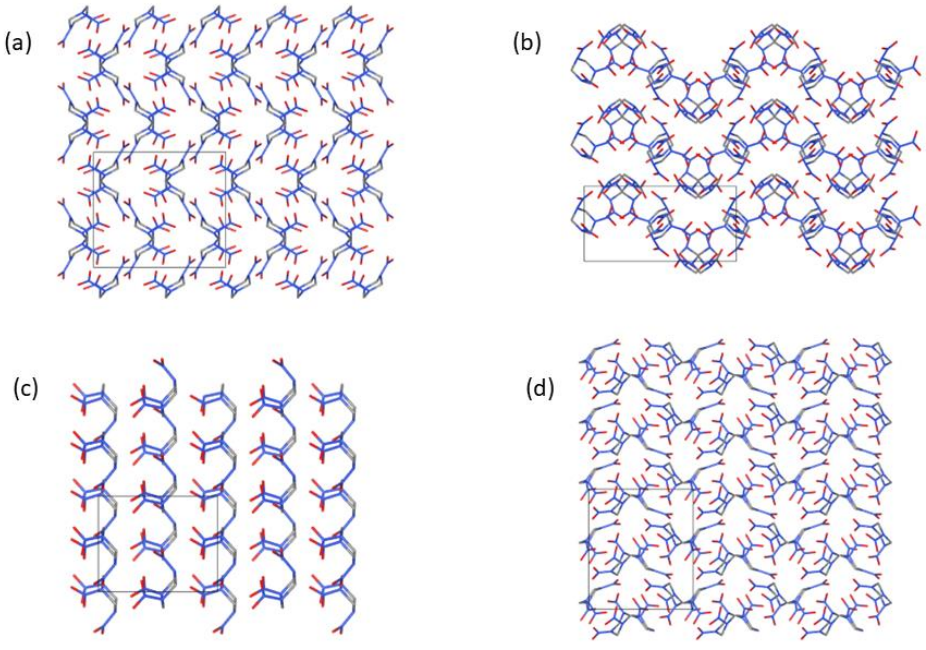

Figure 5.1. Showing the crystal packing of the (a) alpha (b) beta (c) eta and (d) gamma polymorphs of RDX

The polymorphs of RDX do not differ by molecular packing alone; they also present different molecular conformations. In the crystal structures, all molecules present with the triazine ring in a chair conformation and vary in their orientation of the three pendant nitro groups (see Figure 5.2). These groups can either adopt a pseudo-axial or a pseudo-equatorial position. In the α-RDX polymorph, two nitro groups adopt the axial position with one in the equatorial position, thus being termed the AAE conformation. For the β- and ε- forms, all molecules conform to AAA (i.e. all nitro groups are in the axial position). In γ-RDX, the asymmetric unit contains one molecule in the AAA conformation, and another in what is described as an AAI conformation, which is an intermediate state between AAE and AAA. Given the importance of vibrational motions associated with nitro groups presenting as amalgamated modes (i.e. molecular vibrations that get consumed into the top of the phonon bath region) it is likely that any conformational changes in the positions of these groups will alter the associated DoS plots, and thus potentially their predicted IS values.

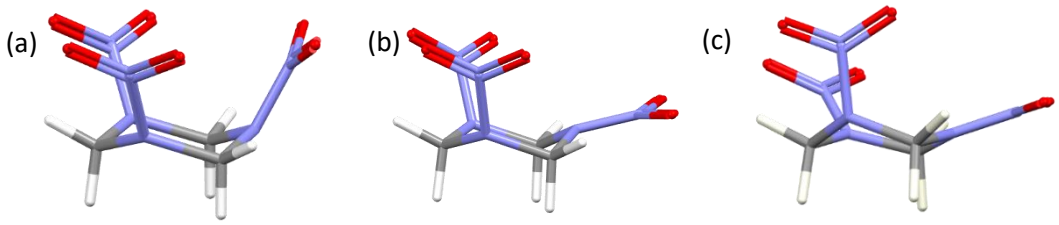

Figure 5.2. Showing (a) AAA (b) AAE and (c) AAI conformation of RDX

To identify the position of Ω_{max} a centre of mass (CoM) analysis was carried out for each of the calculated eigenvectors, for each of the four polymorphs of RDX (Figure 5.3). This gives a quick visual guide of the eigenvector where the vibrational motion transitions from being overwhelmingly delocalised (i.e. related to intermolecular motion) to localised (i.e. internal molecular motion) motion. The top of the phonon bath, Ω_{max} is thus located when the CoM displacement falls below an arbitrary cut off of 10 %, and is often associated with a short gap before the onset of the molecular vibrations. The results are presented in Table 5.3, alongside a count of the number of molecules in the unit cell (Z) and the number of amalgamated modes (Y), such that the total number of modes in the phonon bath can be represented as Z(6+Y).

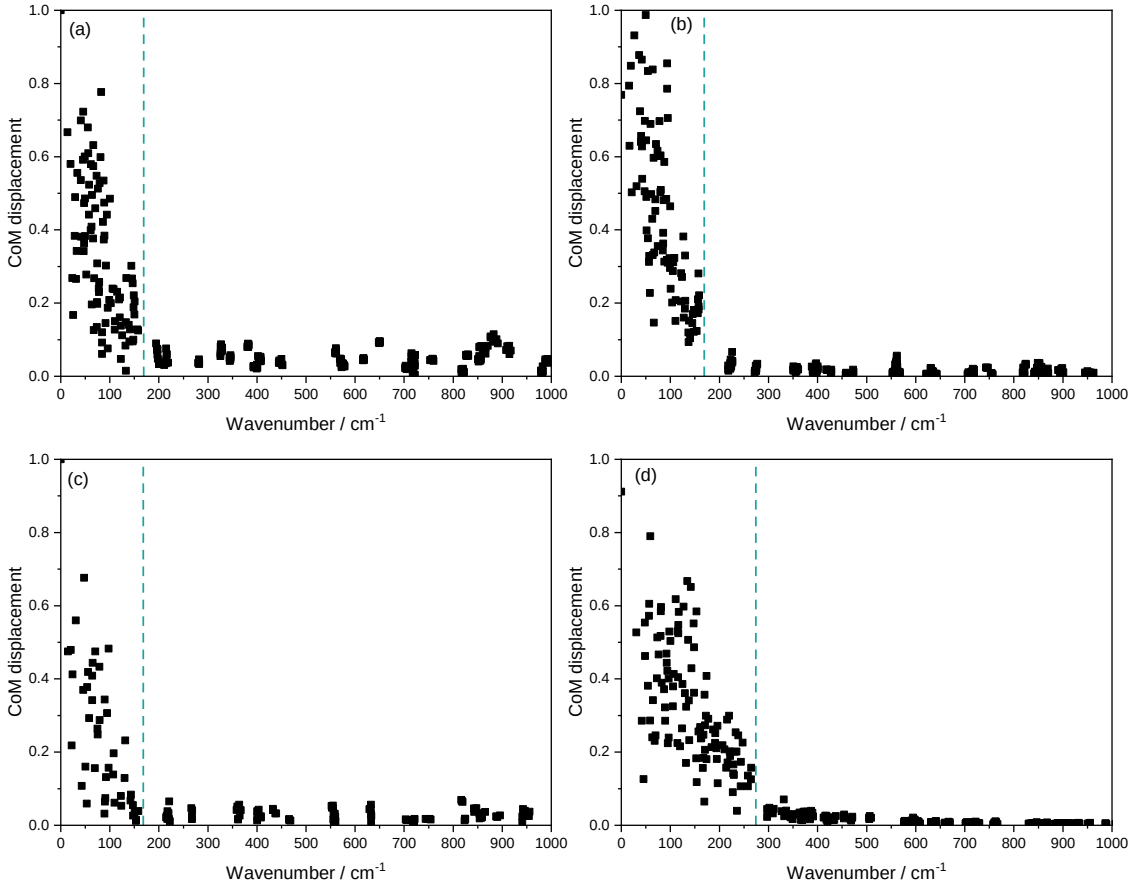

Figure 5.3. CoM displacement for (a) α-RDX (b) β-RDX (c) ε-RDX and (d) γ-RDX

The shock temperature, *i.e*. the temperature assumed for the phonon bath modes upon absorbing the shock wave, is determined from the ratio of the bulk and phonon cumulative heat capacities, C_{tot}/C_{ph}, with a value of 655.5 K assigned for a ratio of 1:1, based on previous work. The cumulative heat capacity graphs are shown in Figure 5.4.

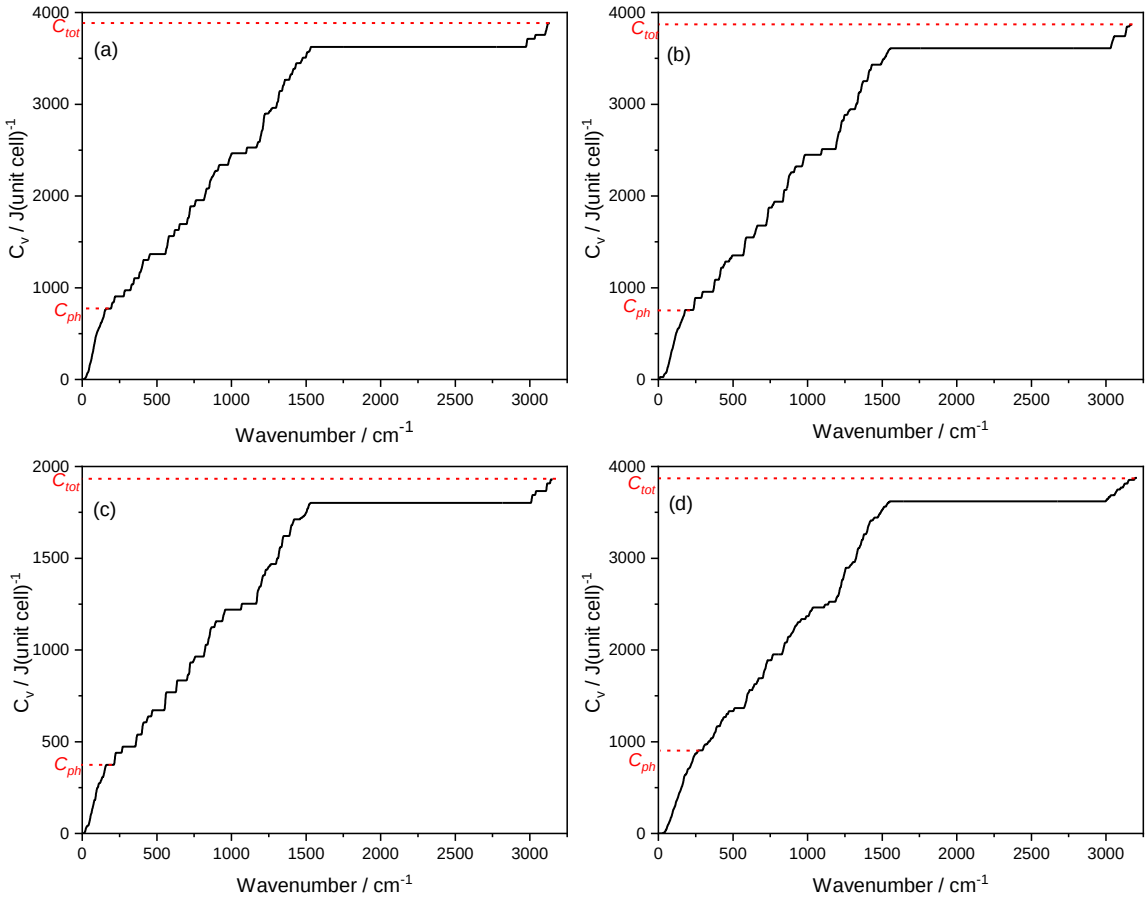

Figure 5.4. Cumulative heat capacities of the RDX polymorphs (a) α-RDX (b) β-RDX (c) ε-RDX and (d) γ-RDX. Values of C_{ph} and C_{tot} are marked by horizontal lines

The DoS and resulting up-pumped 2PhonDoS plots for the four polymorphs of RDX are presented in Figure 5.5 and Table 5.3. From this it is clear that γ-RDX is predicted to be much more sensitive to mechanical impact than the three other polymorphs. This is readily apparent from the 2PhonDoS plots, where the broader phonon bath creates a correspondingly broader up-pumped intensity which is captured by more localised vibrational modes.

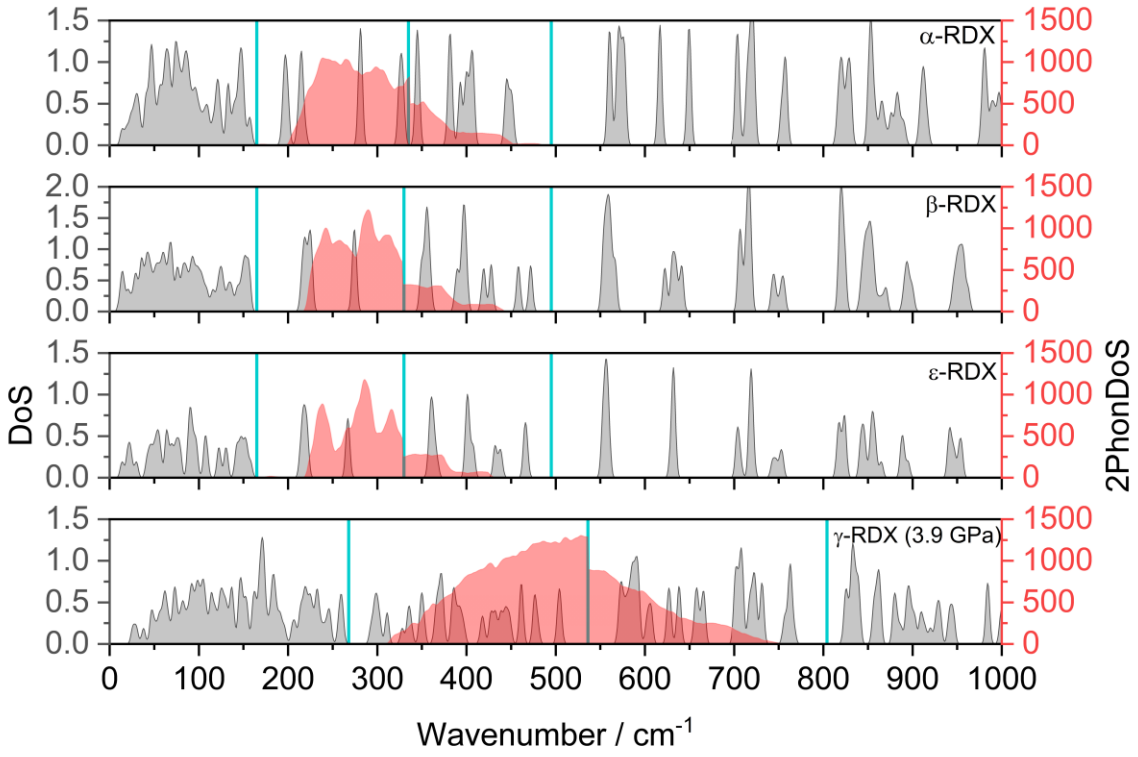

Figure 5.5. Density of states (grey) of the RDX polymorphs with the overlayed 2phonDoS (red), vertical blue lines represent sequential multiples of Ω_{max}

In an effort to more fully understand the variation in 2PhonDoS behaviour, the underlying DoS plots have been studied in more detail. In particular, the density of the phonon bath states (DOPBS, i.e. 0-1 Ω_{max}, Eq. 5.1) and the density of doorway modes (DOPS, i.e. 1-2 Ω_{max}, Eq. 5.2) have both been calculated, according to:

$$Phonon\ bath\ DoS = {g(\omega)_{ph}}\Big/{(g(\omega)_T \times \Omega_{max})} \qquad \text{Equation 5.1}$$

$$Doorway\ DoS = {g(\omega)_D}\Big/{(g(\omega)_T \times \Omega_{max})} \qquad \text{Equation 5.2}$$

Where $g(\omega)_{ph}$ is the integral of the DoS up to Ω_{max}, $g(\omega)_D$is the integral of the DoS in the doorway region and $g(\omega)_T$ is the integration across the total DoS plot. The DOPS in particular is important to calculate because the doorway modes used both in the generation of the 2PhonDoS and to capture the 2PhonDoS. A higher value of DOPS is a way to quickly asses how efficiently impact energy can be vibrationally up-pumped through a system.

Table 5.2. Parameters used to calculate the relative impact sensitivity of polymorphs of RDX, alongside the resulting up-pumped density.

Polymorph	CSD code	Ω_{max}	Z	Z(6+Y)	T_{shock} / K	Up-pumped density/Z/x 10^3 A.U.
α	CTMTNA11	164	8	96	3265	48.1
β	CTMTNA04	164	8	96	3390	26.7
γ	CTMTNA02	268	8	112	2820	176.2
ε	CTMTNA06	164	4	48	3395	15.9

Results are shown in Tables 5.2 and 5.3, from which it is clear that it is the enhanced population of the doorway state region which is responsible for driving up the predicted IS value. This makes sense, as the doorway states in effect provide additional scattering pathways for phonon-phonon collisions, while also providing more vibrational states to capture the 2PhonDoS. Therefore, it should follow that the density of doorway states correlates with predicted impact sensitivity. This suggested trend was also seen with the polymorphs of FOX-7.[25] However, the RDX polymorph series does not completely follow the expected trend, as the ε-RDX polymorph presents the highest doorway density count while only being predicted as the second most impact sensitive polymorph. This suggests therefore that the doorway density count is a rather crude measure, and more work is required to study the composition and distribution of modes contained within the early part of the up-pumping window. The density of the phonon bath states is also shown to have no influence on the predicted impact sensitivity; indeed γ-RDX, predicted to be the most sensitive to impact, has the lowest density of phonon bath states. While the density of the modes in the phonon bath does not correlate with the predicted IS, the larger phonon bath which extends to 274 cm^{-1} (compared to 169 cm^{-1} for the other three polymorphs) does. This is because it not only presents more phonon bath modes to contribute to the 2PhonDoS plots (see Table 5.3) it also increases the values of 2 and $3\Omega_{max}$ and therefore increases the number of modes which can be captured by the 2PhonDoS. Overall, the 2PhonDoS envelope for γ-RDX is significantly broader, compared to the up-pumped distributions for the other three polymorphs.

Table 5.3. Density of phonon bath (DOPBS) and doorway modes (DOPS) for the RDX polymorphs.

Polymorph	DOPBS x 10^{-4}	DOPS x 10^{-5}
α	1.37	3.54
β	1.31	3.56
γ	0.993	5.10
ε	2.69	7.17

The results of predicted IS suggest that the β- and ε-forms behave similarly, with α-RDX being more sensitive and γ-RDX more sensitive still. The differences suggest that the molecular conformation of RDX is incredibly important to the IS. Maintaining the AAA conformation and varying the crystal packing, as seen with β- and ε-polymorphs has little effect. Meanwhile, switching to the AAE molecular conformation presents more vibrational states in the doorway region to boost and trap the up-pumped energy. The same observation holds for γ-RDX, which contains molecules in the AAA and AAI conformation – where there are even more vibrational modes in the up-pumping region.

The question is then, why does Ω_{max} extend so high compared to the three other RDX polymorphs? It could be expected that the conformational changes of the RDX molecules in γ-RDX led to this increase in the phonon bath modes. Animation of the vibrational modes in the 150-250 cm^{-1} range in Jmol[45] shows that these vibrations are amalgamated modes, in that they consist of molecular and lattice vibrations. In this region the majority of the vibrational motion is due to the "wagging" motion of the nitro groups. Using LModeA-nano[46] the force constants of the N—NO_2 bonds in γ-RDX were calculated. This shows that the strongest bond is that in the intermediate position in the AAI conformation (Figure 5.6), and thus vibrational modes involving the motion of this bond will vibrate at a higher frequency than the axial positioned groups. .

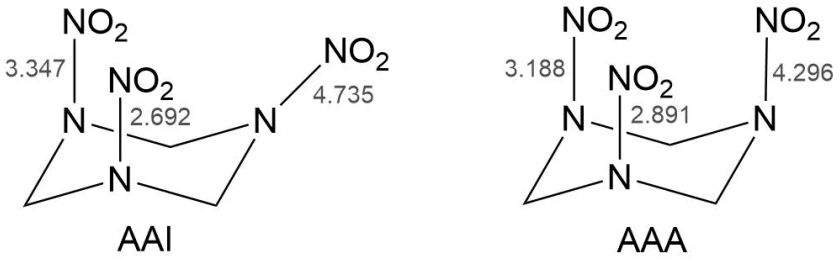

Figure 5.6. Conformations of the molecules in γ-RDX, with the force constants (mDyn $Å^{-1}$) of the N—NO_2 bonds shown.

This was explored further by calculating the adiabatic connection scheme (ACS) of the individual RDX molecules in different conformations (Figure 5.7). An ACS shows how local modes of vibration (i.e. those which are pure vibrational motion of a single bond stretch or angle bend in a molecule) contribute to the normal modes of vibration in an isolated molecule and is calculated using LModeA.[47] In this case the N—N bond to the NO_2 group in the I or E position is highlighted.

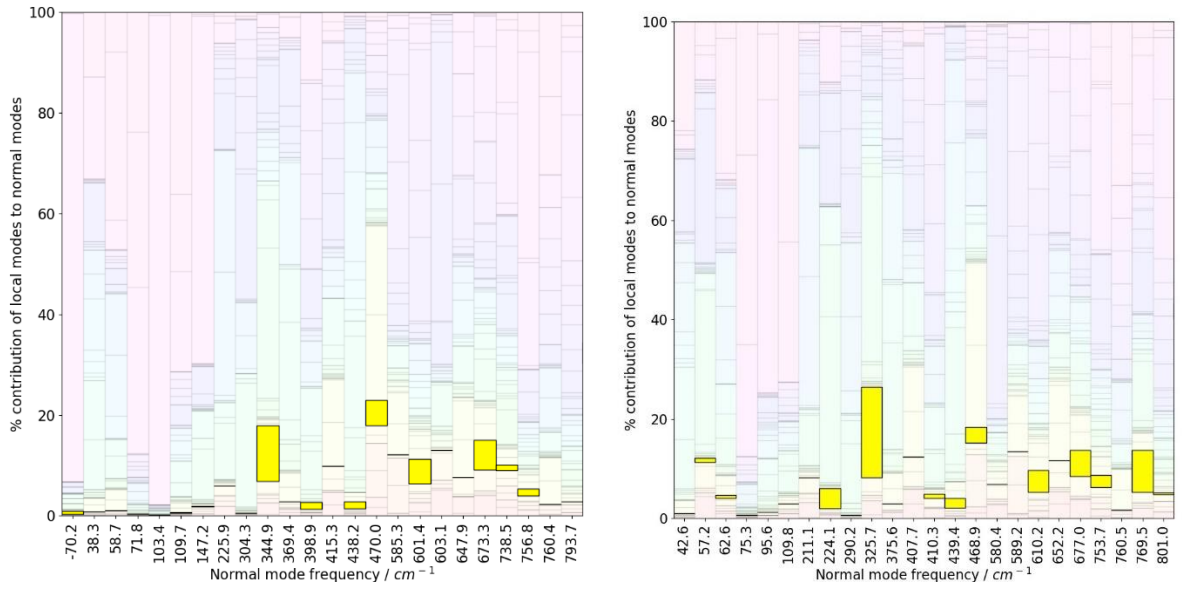

Figure 5.7. Adiabatic Connection Schemes for RDX in the AAI position (left) and AAE position (right). Yellow bars highlight the N—NO_2 bond.

The N-N bond stretch contribution from either the I or E position is highlighted in yellow. In the isolated molecules, there is no clear indication of “mode hardening” of the N—N bond stretch between the different conformations, and as seen in Figure 5.7 there is no significant bond stretching motion in what would be the phonon bath

region in a condensed phase system, estimated to be between 0-300 cm^{-1}. Therefore, there must be another reason for in the increased value of Ω_{max}.

It should be noted that the DoS calculated for γ-RDX was obtained at high pressure, and as such the modes of vibration are likely to have 'hardened' (shifted to higher wavenumber) as a direct result of application of the external pressure. It has been noted that pressures of up to ca. 5 GPa, as in this work, can be expected to produce blue-shift in vibrational frequencies on the order of 5-20 cm^{-1}.[48]

In an attempt to directly quantify the effect of the external pressure, the optimisation for γ-RDX was repeated in the absence of the external pressure. This unfortunately resulted in the unit cell expanding by over 30%, which does not provide a realistic representation of the high-pressure phase. An alternative investigation is to optimise α-RDX in the presence of 3.9 GPa external pressure. (Figure 5.8) to observe how this changes the vibrational spectrum and subsequent calculated up-pumped density changes. The unit cell of α-RDX decreased to 1382.01 $Å^3$ which is comparable to that of γ-RDX which has a unit cell volume of 1357.6 $Å^3$. To note is the stark increase in the region over which the phonon bath exists- in the 3.9 GPa structure Ω_{max} reaches 257 cm^{-1} while external modes of vibration have experienced blue-shift by approx. 5-10 cm^{-1}. This brings the value of Ω_{max} in line with that of γ-RDX. Therefore, it is most likely that it is simply the direct compression of the structure which leads to closer, and therefore stronger, intermolecular interactions is the cause of the increase of the upper limit of the phonon bath modes in γ-RDX.

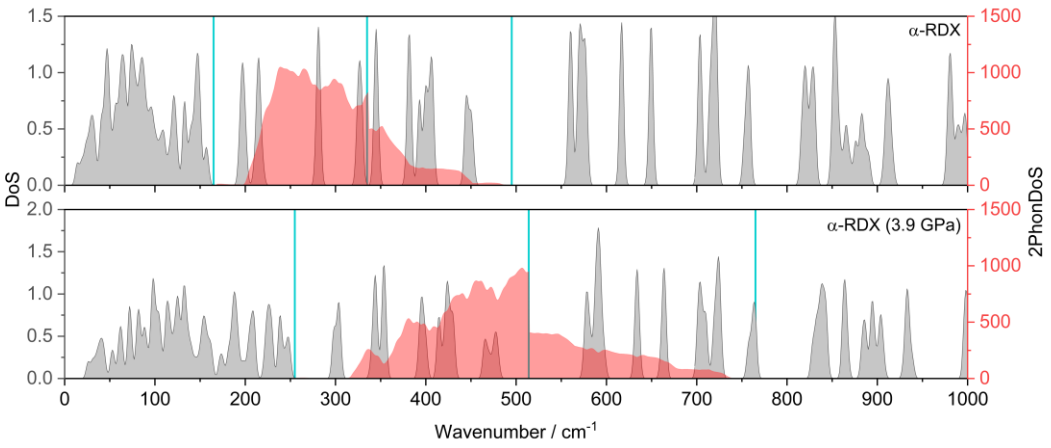

Figure 5.8. Spectra for α-RDX (a) and (b) α-RDX optimised at 3.9 GPa. Ω_{max} and its multiples are shown by blue vertical lines.

Comparing the DOPBS of the two α-RDX forms, it actually decreases in the high pressure structure 1.01 vs 1.37, due to the normalisation by the size of the phonon bath this is understandable. The number of amalgamated modes Z(6+Y) increases in the higher pressure system 112 up from 96. Indeed, at increased pressure the DoS/2PhonDoS overlays for α-RDX and γ-RDX look similar. However, the predicted up-pumped density of α-RDX at 3.9 GPa is less than γ-RDX; 67.0 vs 176.2. As mentioned, the unit cell of γ-RDX has Z'=2, due to having two different conformations of the RDX molecule. This breaks the degeneracy of the system, leading to a splitting in the vibrational peaks between 320 – 400 cm^{-1} in γ-RDX. Constructing the partial DoS for γ-RDX with respect to each conformation of molecule is shown in Figure 5.9 and highlights how the vibrational modes in this region have vibrational motion attributed to molecules in the pseudo-AAI conformation.

This analysis shows that peaks in the 330-360 cm^{-1}, which are attributed to the AAI conformation alone, help to populate the doorway region. These eigenvectors are best characterised (visually) as N—NO_2 bond stretching and ring deformation modes. The analogous vibrations for the AA conformation fall into the 360-390 cm^{-1} region, where the other AAI ring deformation modes fall. Similar eigenvectors are observed for the AAA conformer at 350-360 cm^{-1} in β-RDX and 360-370 cm^{-1} in ε-RDX, while those associated with the AAE conformer in α-RDX at 340-350 cm^{-1}. These modes therefore fall outside the doorway regions for all phases bar γ-RDX.

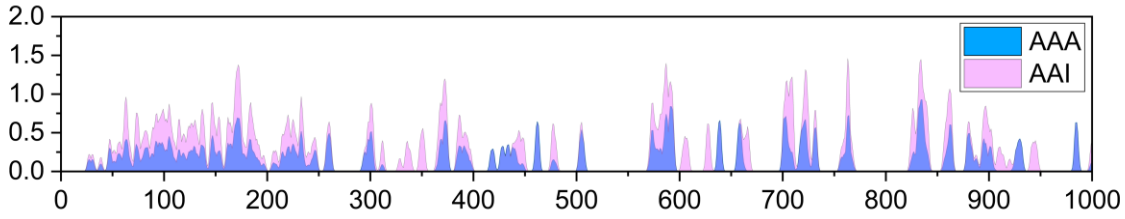

Figure 5.9. Partial density of states for γ-RDX showing the contributions to the vibrational modes with conformers AAI and AAA.

It's apparent therefore that there are two separate factors which are responsible for the increased predicted IS of γ-RDX. First, the direct compression of the material leads to shorter and stronger intermolecular interactions which influences the makeup of the phonon bath region of the density of states. Secondly, there are changes in the

molecular conformation which alters the distribution of the molecular vibrations that fall within the up-pumping window.

As the predicted IS values for the different polymorphs of RDX are relative values, it is possible to then rank their predictions alongside that of other EMs that have been subjected to the same up-pumping model. This is presented in Figure 5.10, from which a clear inverse relationship is drawn – the more sensitive a material is to impact (i.e. the lower the amount of impact energy required to initiate a material), the higher the calculated up-pumped density. From the data presented, assuming an experimental IS value for RDX is 13 J and that this corresponds to the α-polymorph, it can be seen that the predicted impact sensitivity sits close to the curve. As there are no known experimental values for the other polymorphs, the corresponding data points have been plotted at the same value on the x-axis. β-RDX sits below the trend-curve and ε-RDX sits lower still. However, the prediction for γ-RDX, the high pressure polymorph, lies on the established trend line between experimental and prediction and has a predicted value sitting closer to ε-CL-20. This raises the important questions as to the behaviour of RDX under shock-wave conditions. It has been previously reported that a phase change occurs in samples of α-RDX under shock compression,[49] with Patterson *et. al.* reporting Raman spectra of RDX samples shocked between 3 and 5.5 GPa which show similar spectral changes in static pressure measurements commensurate with the α to γ transition. With this easily achievable phase transition being known, questioning whether the same process occurs during the BAM hammer fall tests is legitimate. Thus, this work suggests further issues exist with the experimental impact sensitivity measurements beyond those already documented. The simulations here raise the possibility that if the α to γ transition could be supressed, then the shock sensitivity of RDX could be improved. This could be achieved by doping α-RDX with an additive that increases the α to γ transition pressure, therefore supressing the formation of the sensitive γ polymorph. It also highlights the power of the vibrational up-pumping prediction method to give new insight into important performance and safety metrics for this important EM that have, effectively, been misunderstood.

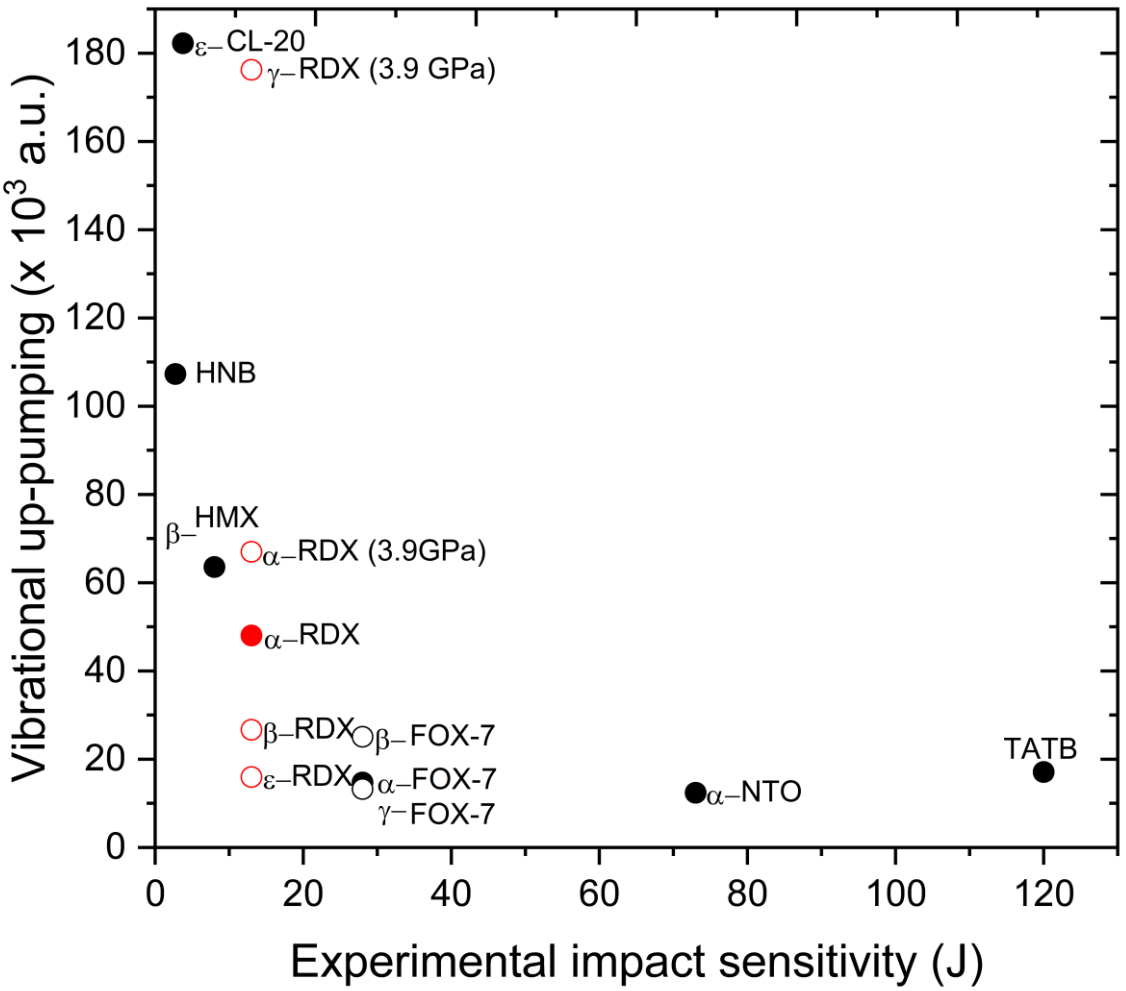

Figure 5.10. Experimental impact sensitivity of known energetics plotted against the calculated up-pumped density. The results of RDX are all plotted against the widely reported IS of RDX - 7 J.[50]

These results are also important as they show that even a slight conformational change can lead to a considerable change in the sensitivity of a material. This shows how important it is to incorporate computational methods with experimental methods to further the understanding of detonation pathways. This can provide the catalyst for further research into understanding how EMs behave under testing conditions, and stress the importance of giving due consideration to the effect of polymorphism on understanding the physical responses of EMs.

5.3.2. 2,4-dinitroanisole (DNAN)

2,4-dinitroanisole (DNAN), Figure 5.11, has been proposed as a replacement for TNT in melt-cast formulations.[7,51] It is reported to have a lower IS than TNT (the IS

of TNT = 24 J)[52] but there is wide variability in the reports, with e.g. one reported figure of insensitivity (FOI) from a Rotter apparatus of > 220 cm,[53] another report with H_{50} = 117.5 cm (5 kg mass, giving 57 J) [54] while a BAM fall hammer apparatus reports > 24 J.[55] In addition, although two DNAN polymorphs have been characterised and recovered to ambient conditions,[56] no clarification has been given as to which polymorph has been used for impact sensitivity testing, although based on the reported stabilities, it can be assumed to be DNAN-I.

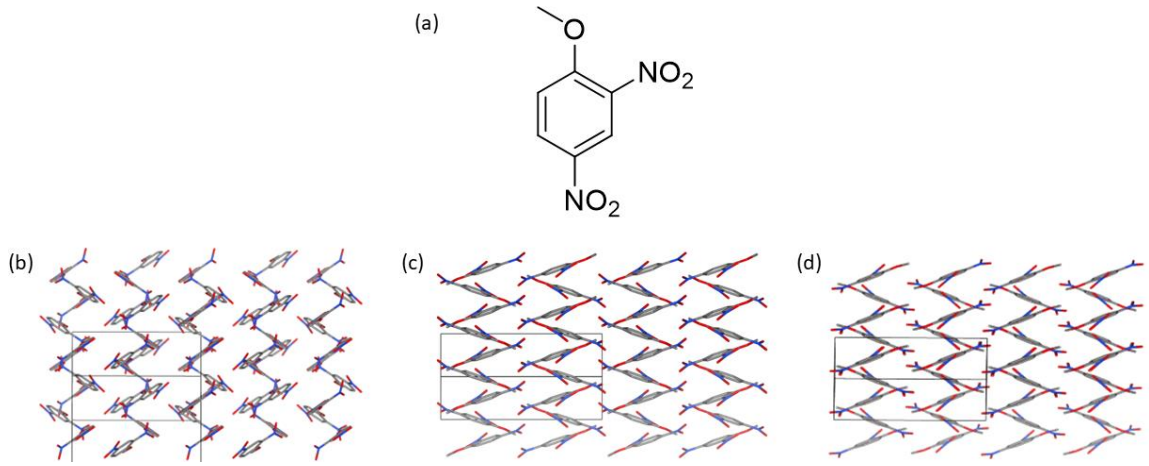

Figure 5.11. (a) Molecular structure of DNAN, and crystal packing of (b) DNAN-I, (c) DNAN-II and (d) DNAN-III

Considering that DNAN is used as a melt-cast EM, it is important to consider any polymorphic phase transitions that may arise under non-ambient conditions, as changes in crystal packing may lead to cracks and defects forming in the material, which can result in an unpredictable EM formulation. Currently five polymorphs have been reported; DNAN-I and DNAN-II (also known as α-DNAN and β-DNAN, respectively, see Figures 5.11 and 5.12) are both obtained at ambient conditions. Takahashi *et al*[56] showed that upon cooling DNAN-II appears to undergo a low temperature phase transition at 264.5 K, with the b angle increasing from 90.190 ^{o} (at 298 K) to 96.716 ^{o} (at 100 K); this phase was referred to as DNAN-III by Coster *et al*.[57] Coster also reports that DNAN-III transforms at high pressures (ca. 2.9 GPa) to DNAN-IV, while high pressure neutron powder diffraction has identified a fifth polymorph, DNAN-V, accessible through direct compression of DNAN-I. However, the crystal structures of DNAN-IV and –V have not yet been solved. The relationship between the known polymorphs is shown in Figure 5.12.

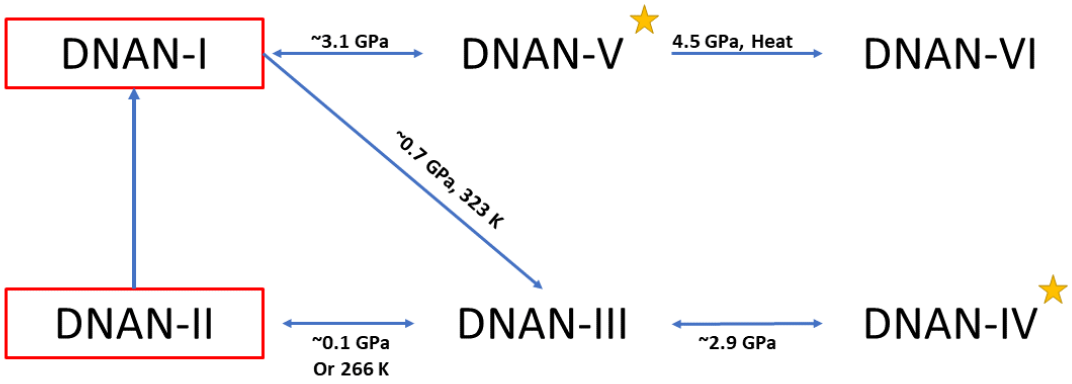

Figure 5.12. Showing the relationship between the polymorphs of DNAN. A red box shows ambient condition polymorphs, while yellow stars highlight polymorphs for which crystal structures are not yet reported in the literature

This therefore leaves three structures (I, II and III) suitable for IS prediction studies. Within this work the IS of a further polymorph, known as DNAN-VI, is also calculated. This was obtained and characterised in-house by Paul Coster by direct compression and heating of DNAN-I to pressures above 4.5 GPa. The crystal packing of this high pressure polymorph is shown in Figure 5.13.

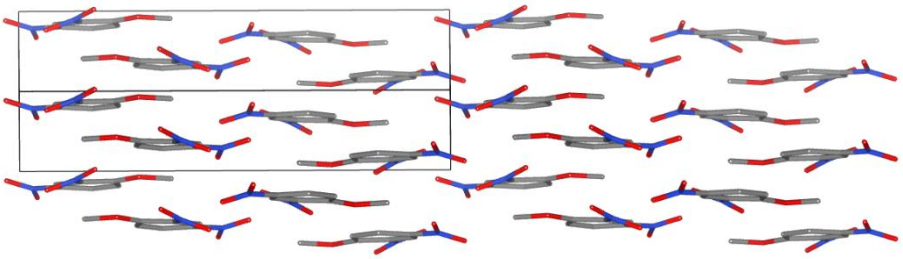

Figure 5.13. Showing the crystal packing of DNAN-VI polymorph

Through visual inspection of the crystal structures alone, it could be assumed that DNAN-VI would be less sensitive to mechanical impact than the other three polymorphs, as the crystal packing conforms to a more layered structure; this is typically thought to result in a reduction in IS due to the layers being better able to dissipate mechanochemical energy via slippage of the layers.[58,59] This layering is absent in DNAN-I, II and III, which exhibit herringbone structures.

As with the RDX study, values for Ω_{max} for the DNAN polymorphs were determined from a centre of mass analysis of the computed eigenvectors, along with the

appearance of gap in the wavenumber distribution, before the on-set of the molecular-based vibrations. This analysis is shown in Figure 5.14, resulting in the phonon bath mode count given in Table 5.5.

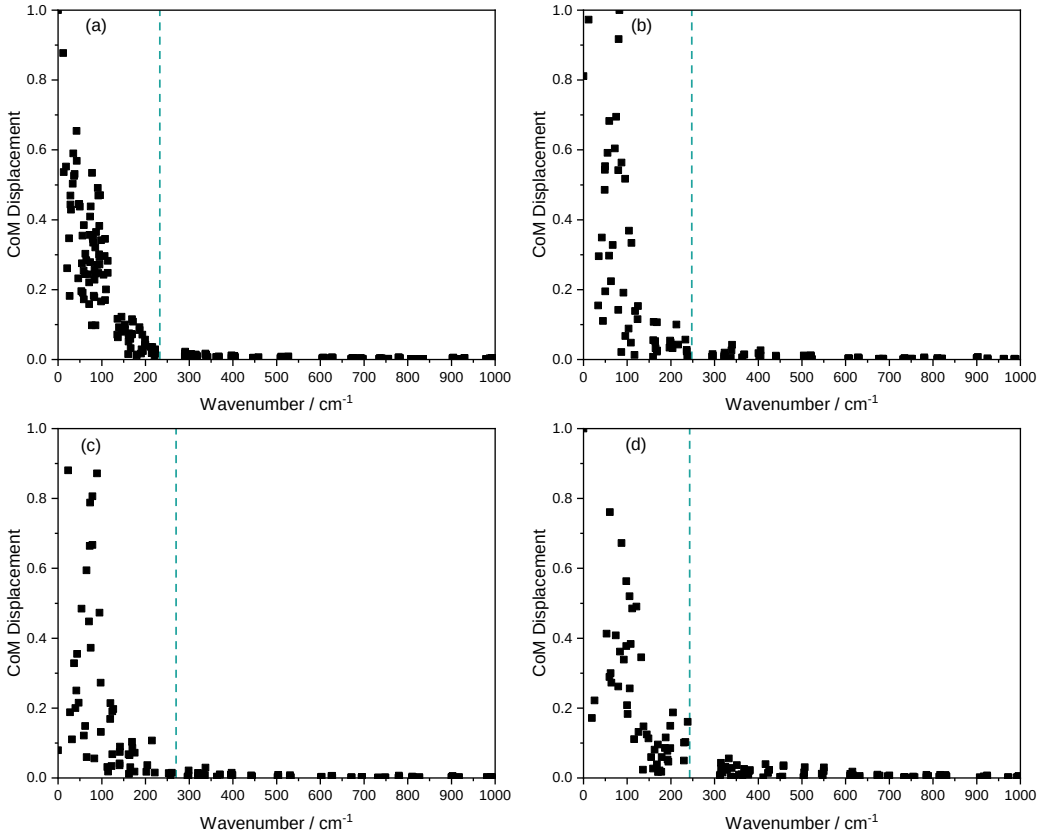

Figure 5.14. Centre of Mass displacement analysis for the (a) DNAN-I (b) DNAN-II (c) DNAN-III and (d) DNAN-VI polymorphs. Ω_{max} is marked by the vertical dotted line

The shock temperatures are calculated based on the ratio of the bulk and phonon cumulative heat capacities, C_{tot}/C_{ph}, with a value of 550 K assigned for a ratio of 1:1, based on previous work. The cumulative heat capacity graphs are shown in Figure 5.15.

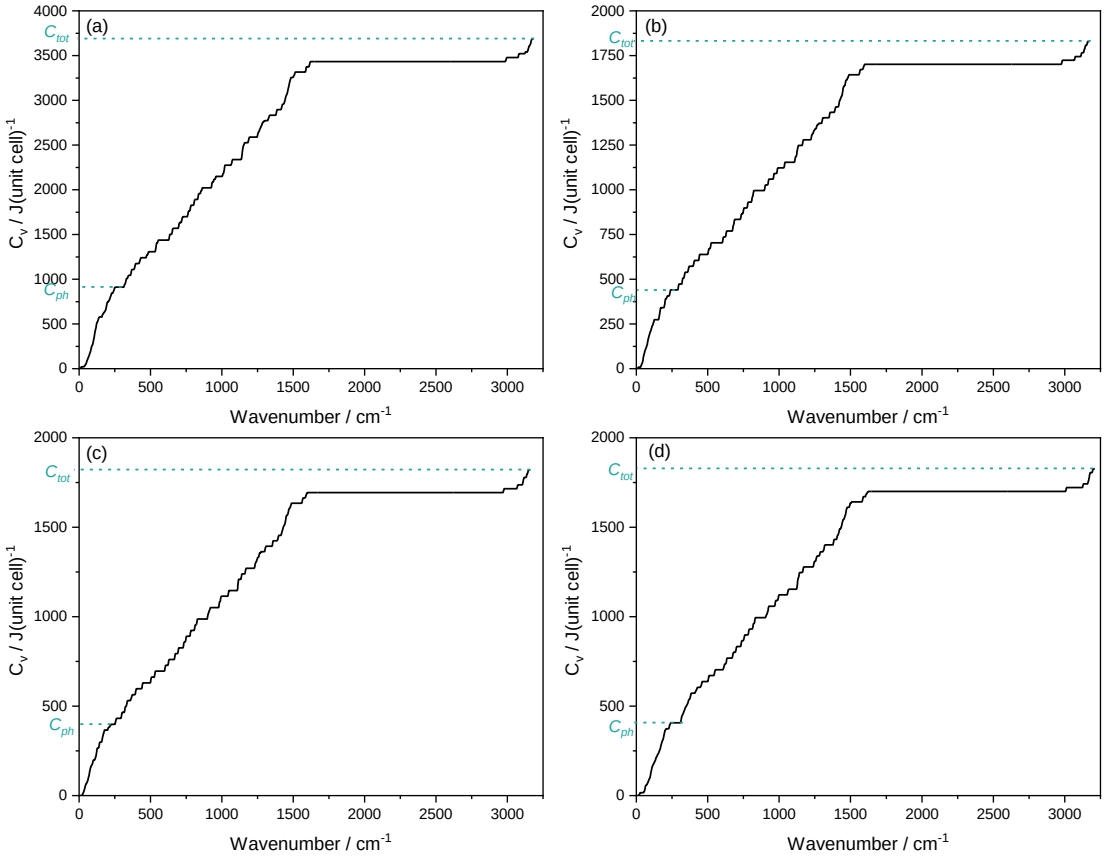

Figure 5.15. Cumulative heat capacities for the (a) DNAN-I (b) DNAN-II (c) DNAN-III and (d) DNAN-VI polymorphs. The values of C_{ph} and C_{tot} are marked by horizonal lines

The calculated DoS of the four polymorphs are shown in Figure 5.16, along with their respective 2PhonDoS up-pumping envelopes. DNAN-I, II and III show similar vibrational modes above 300 cm^{-1}, while DNAN-VI presents a broader continuum of vibrational modes between 300 and 400 cm^{-1}. For all structures, Ω_{max} falls in a similar region (between 231 and 270 cm^{-1}), and the same number of amalgamated vibrational modes (Y) present in the phonon bath for all polymorphs (Table 5.5.). The most surprising aspect of the calculated DoS is that the upper limit of the phonon bath modes for -VI is on par with the other ambient pressure polymorphs, a phenomenon that has not been seen with other high-pressure EMs in this thesis (RDX and NTO.BIPY). It is possible that the compression of the material does not lead to a blue-shift in vibrational modes, due to the crystal packing of DNAN-VI differing significantly from other DNAN polymorphs – with molecules arranged in flat layers (further validation of this would have to be achieved through additional calculations EMs which show molecules in layers).

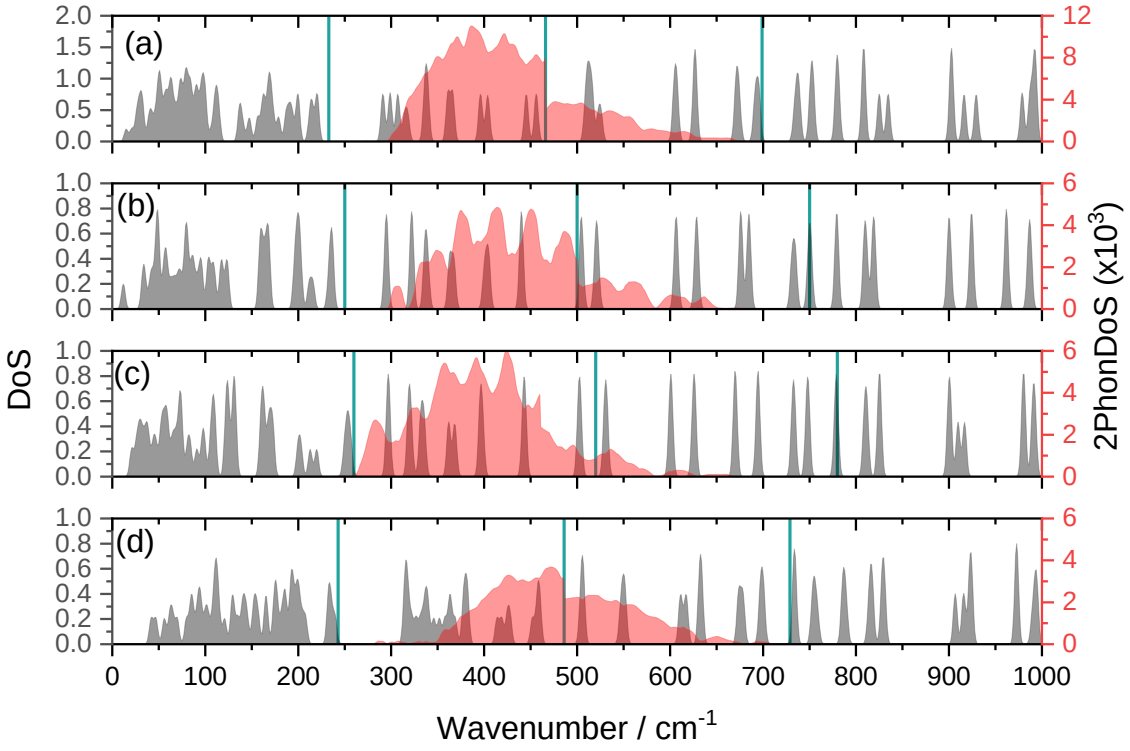

Figure 5.16. Calculated density of states (grey) for the four polymorphs of DNAN (a) -I, (b) -II, (c) -III, (d) -VI (calculated at 4.5 GPa). Blue vertical lines represent sequential multiples of Ω_{max}. Red plots show the resulting two phonon density of states.

The relative impact sensitivity of the four characterised polymorphs, I, II, III and VI have been calculated (Table 5.4) in the usual way. This analysis shows that DNAN-I is predicted to be the most sensitive to mechanical impact, which is attributed to the low DOPS which highlights the fewer pathways available to up-pump impact energy through the system. The predicted impact sensitivities of the II and III polymorphs are very similar, with calculated up-pumped density of 60.4 and 73.0 for DNAN-II and III respectively. These results can be expected given the similarities in their crystal structures (Table 5.4 and Figure 5.11), with only a change in the β angle being indicative of phase change. Although DNAN-VI is a polymorph which exists at high pressure (a fact which greatly increases the predicted IS for γ-RDX) here the predicted IS of the high pressure polymorph sits in the middle of the DNAN series. DNAN-VI does not have the lowest sensitivity, as would be expected for solids which exhibit molecules in flat layers.

Table 5.4. Features of the polymorphs of DNAN that were used to predict their impact sensitivities, and the predicted sensitivities. Z denotes the number of molecules present in reach unit cell, such that the total phonon mode count equates Z(6+Y), where Y denotes the number of amalgamated modes.

DNAN polymorph	CSD Code	Ω_{max}	Z	Z(6+Y)	T_{shock} / K	Up-pumped density/Z/x10^3 a.u.
I	FESNEW	233	8	112	2658	100.6
II	FESNEW12	250	4	56	2724	60.4
III	FESNEW15	270	4	56	2763	73.1
VI	-	243	4	56	2944	63.2

Animation of the vibrational modes of the DNAN polymorphs II, III and IV confirm that the modes around 350 cm^{-1} show significant twisting motion of the methoxy groups. This is in contrast with DNAN-I, where analogous motion occurred at *ca.* 230 cm^{-1} which is in the phonon bath region which would correspondingly increase the magnitude of the 2PhonDoS in DNAN-I. Given this information, the differences in molecular conformation were looked into – as this was the driving factor in the sensitivity differences of RDX polymorphs. However, the differences observed in the molecular structures between the four phases is small, with the $–OCH_3$ group deviating from the plane of the aromatic ring by 3.2 and 10.7° in DNAN-I (where Z = 2 for the asymmetric unit), compared to 0.5° for DNAN-II, 1.2° for DNAN-III and 2.9° for DNAN-VI. It is possible that this change in conformation in DNAN-I leads to significantly higher sensitivity of this polymorph.

Effect of crystal packing

In an effort, therefore, to ascertain whether the changes in vibrational mode distribution are related to crystal packing, non-covalent interaction (NCI) plots were generated for all DNAN polymorphs. These plots characterise stationary points in the electron density associated with non-covalent (intermolecular) interactions. Figures 5.17 (a-d) show the reduced density gradient plotted against the sign of the λ_2 parameter of the electron density. Points on the graphs where the reduced density gradient approaches 0 suggests a minima in the electron density of the system,

therefore showing the occurrence of an interaction, while the value of $(\lambda_2)\rho$ characterises the nature of that interaction. The NCI plots for DNAN-I, II and III are largely symmetrical about the *x*-axis, with the numerical range indicative of weak dispersion interactions. The broader extension into negative $\text{sign}(\lambda_2)\rho$ values (which denote attractive interactions) outweighs the narrower extension into positive $\text{sign}(\lambda_2)\rho$ values (which denote repulsive interactions). In DNAN-I, -II and -III the strongest interactions occur at circa -0.015 a.u., which are represented as the bluest features on the 3D isosurface plot in Figure 5.17(e)-(g). These are assigned to C-H…O non-classical hydrogen bonds. The NCI plot for DNAN-VI suggests a structure dominated by stronger dispersion interactions (Figure 5.17(d) at ca. -0.025 a.u., which are presented as strongly coloured dark blue discs on the 3D isosurface plot (Figure 5.17(h)). These indicate that significantly strong methyl C-H…ONO non-classical hydrogen bond interactions are present in the high pressure phase, which are directional in two dimensions due to the layered crystal packing. These stronger interactions are likely to 'pin' the OCH_3 groups in place. This would likely reduce the structural flexibility of this side-chain, and thus 'mode harden' the low energy vibrations associated with this torsional twisting motion – as noted earlier this vibrational motion occurs in the ~350 cm^{-1} region for DNAN-VI which is not excited fully by the 2PhonDoS (Figure 5.16). Therefore, the predicted sensitivity of the DNAN-VI is lower than the other, ambient, polymorphs which suggests that any effect of on IS by external pressure has been outweighed by crystal packing.

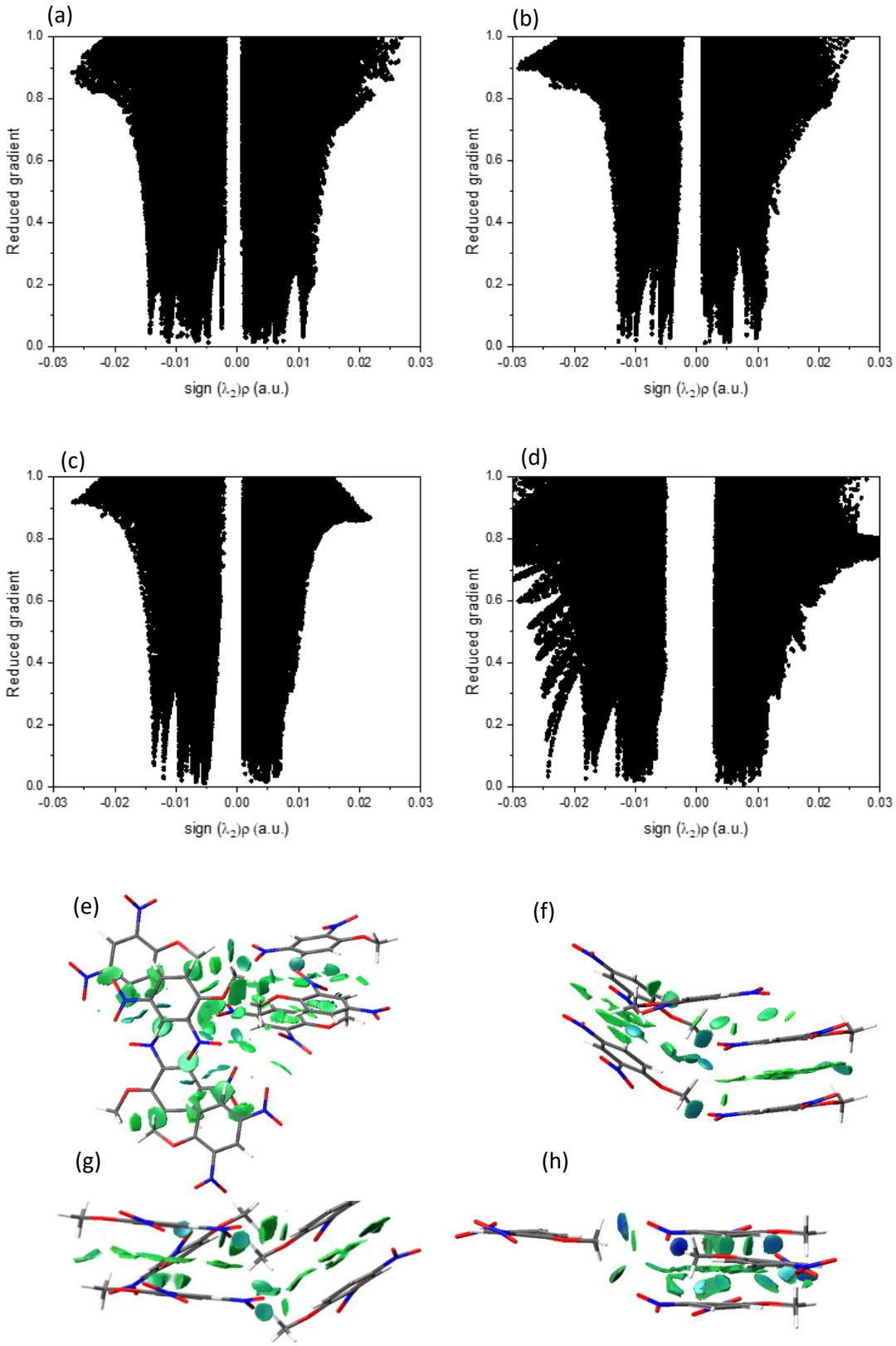

Figure 5.17. Non-covalent interaction plots presented in 2D form for (a) DNAN-I and (b) DNAN-II (c) DNAN-III and (d) DNAN-VI, and 3D from in (e) to (h), respectively. 3D plots are shown at isosuface value 0.5 a.u.

Effect of pressure

The vibrational spectrum of DNAN-VI was obtained by optimising the structure under the experimental pressure the structure was characterised at (4.5 GPa). It is important to understand that comparing the results of DNAN-I and II to DNAN-VI is a valid approach, as the computational modelling differs. With the case of RDX, it was seen that the high pressure polymorph far exceeded the other polymorphs with respect to predicted IS. In order to see how external pressure affects the computational model, external pressure (4.5 GPa) was applied during the optimisation of DNAN-I. The results of this, in the form of the DoS/2PhonDoS overlay are shown in Figure 5.18.

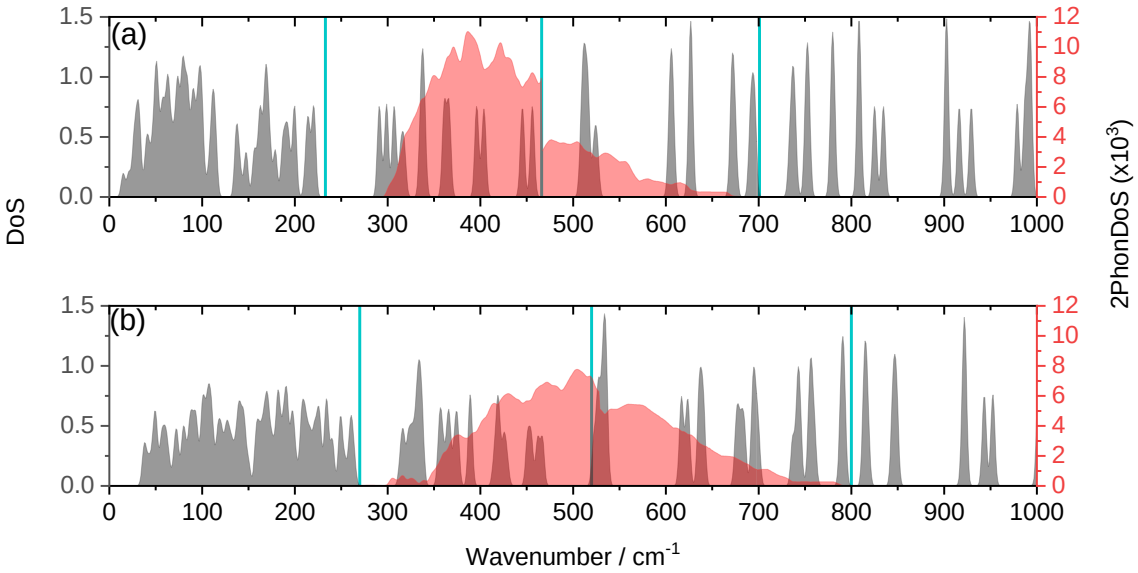

Figure 5.18. DNAN-I optimised at (a) ambient conditions and (b) at 4.5 GPa.

The optimisation of DNAN-I at 4.5 GPa shows that slight mode hardening does occur, with vibrational modes blue shifting and the top of the phonon bath increases from 233 to 274 cm^{-1}, which increases the size of the doorway region. The twisting motion of the -OCH_3 group experiences mode hardening by ~ 5 cm^{-1}. It is highly probable then that the effect of increasing pressure during optimisation of the system is not enough to alter the -OCH_3 motion which is most likely to be responsible for increased predicted IS. The predicted IS of DNAN-I at 4.5 GPa is marginally less than what is seen of DNAN-I at ambient conditions with calculated up-pumped density of 96 vs. 100 (84 vs 87 when C—N vibrational motion is not included in the integration – see below), however this decrease is not akin to the IS prediction of

DNAN-VI. Therefore, it can be concluded that optimising structures with an external pressure does alter the predicted sensitivity, but does not necessarily always increase the predicted IS (as was seen with RDX polymorphs). Therefore, using a different pressure to optimise DNAN-VI is an acceptable approach in this instance. It also likely therefore, that the change in crystal packing is the driving factor in the change in predicted IS for DNAN-VI, rather than any influences on the computational model when optimised at non-ambient pressures.

The calculated IS values for the DNAN polymorphic series are presented assuming an experimental IS of 60J (Figure 5.19). The DNAN polymorphs seem to buck the exponential trend of the established EMs in that they do not lie on the expected trendline. And for all polymorphs except DNAN-I, the IS is predicted to be lower than that of TNT, for which there is no experimental verification. DNAN-II and DNAN-VI most closely fits the trend line between the calculated up-pumped density and experimental impact sensitivity. DNAN is reported to be less sensitive than o-TNT, and here it can be seen that the predicted IS of o-TNT falls in the middle of the range of the predicted IS of the four DNAN polymorphs. This is unexpected, as all experimental measurements point towards DNAN being less prone to mechanical initiation than TNT, given the additional data point of m-TNT (see Chapter 5.3.3), DNAN-I still exceeds both polymorphs of TNT in terms of predicted IS.

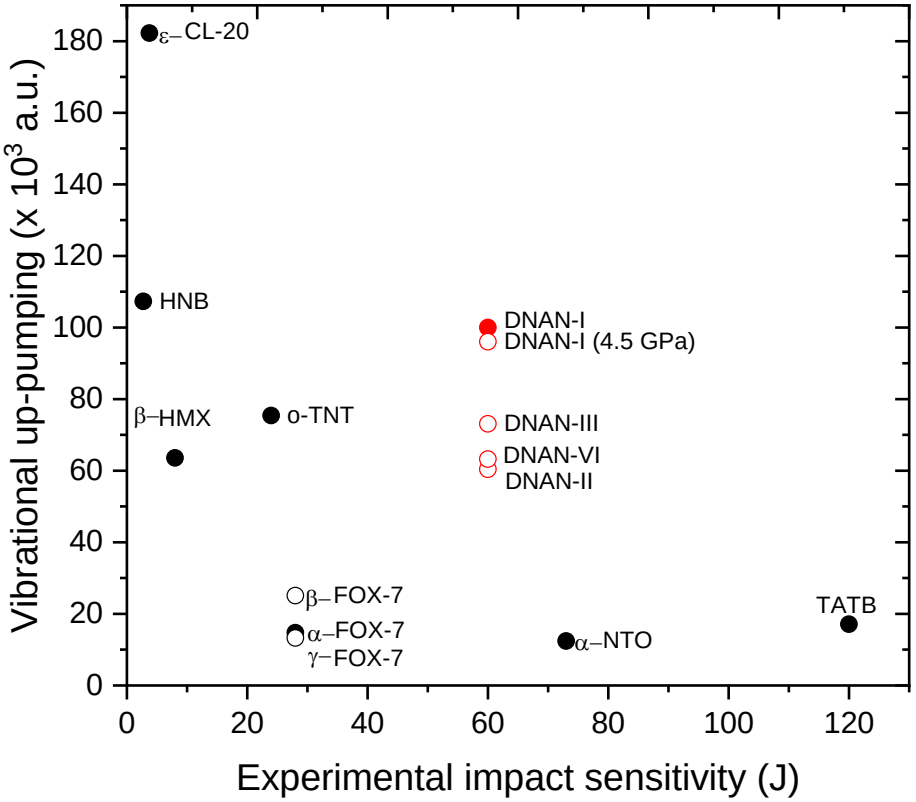

Figure 5.19. Predicted IS of DNAN polymorphs (red) plotted against the known sensitivity of 60 J.[62] Shown alongside the experimental impact sensitivities for known EMs (black), calculated in other work.[61] Experimental IS of values are shown as solid symbols. Open circles are theoretical predictions.

All DNAN polymorphs have been over predicted with respect to sensitivity, therefore it is possible that adjustments to the vibrational up-pumping method could be made. Studies suggest that trigger bonds could be the most important part of energetic molecules, as these are the weakest bond in a molecule.[60] These weakest bonds are typically R—NO_2 bonds and in the case of DNAN, this is C—NO_2. One proposed modification to the vibrational up-pumping method is to only integrate the 2PhonDoS over the portion of the DoS in which there is motion by the trigger linkage. The reasoning for this is that any capturing of the 2PhonDoS by vibrational modes which arise from motion of non-energetic portions of the molecule would not result in the initiation of the EM. Therefore, the IS of EMs could be over-predicted if they contain functional groups which are not typically energetic components.

Partial DoS were constructed with respect to the C—NO_2 eigenvectors for all of the polymorphs. Any eigenvector which consisted of any C—NO_2 motion were included

in the integration portion of the vibrational up-pumping calculation, as excitation of these modes will lead to the excitation of the C—NO_2 bonds. Figure 5.20 shows the modes pertaining to this trigger bond motion. The only polymorph which this has a significant impact upon is DNAN-I, with eigenvectors in the 280 – 322 cm^{-1} region not having any significant movement of the C—NO_2 bonds. Exclusion of this motion from the integration groups would result in a closer grouping of the DNAN polymorphs in Figure 5.19, Table 5.5.

Table 5.5. Predicted up-pumped density of DNAN polymorphs.

DNAN	**Up-pumped density/Z/x10^3 a.u.**	**Up-pumped density/Z/x10^3 a.u. (C–NO_2 only)**
DNAN-I	100.6	87.5
DNAN-II	60.4	59.9
DNAN-III	73.1	72.0
DNAN-VI	63.2	59.8
DNAN-I (4.5 GPa)	96.1	84.3

Note that this exclusion has only been carried out for polymorphs of DNAN and has not been extended to other polymorphs in this work. However, this does open the door for further work and is a way to possibly improve the reliability of the vibrational up-pumping method.

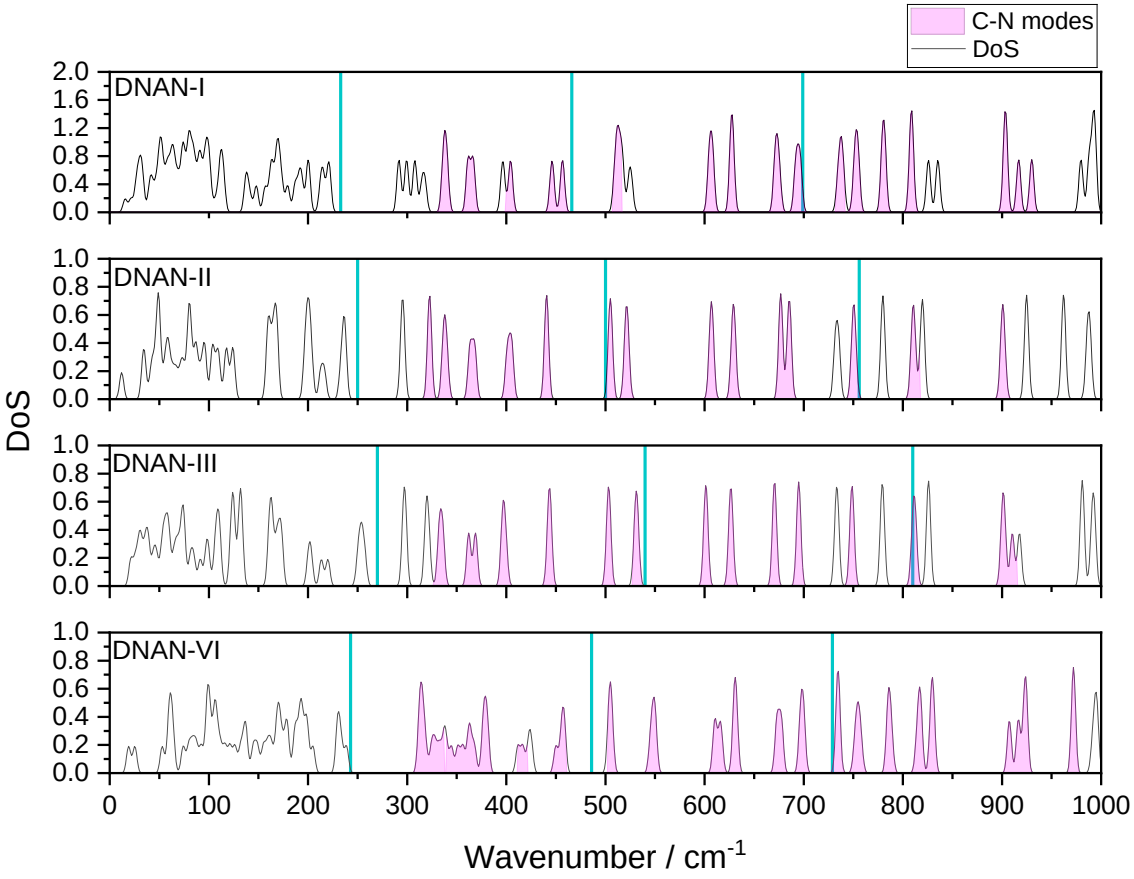

Figure 5.20. DoS of DNAN polymorphs, with partial DoS attributed to C-N vibrational modes highlighted. Vertical blue lines highlight Ω_{max} and its multiples.

If the up-pumping method is correctly predicting IS for this polymorphic series, this would suggest that, unlike as observed for RDX earlier in this chapter, DNAN does not transition to the high pressure form upon exposure to mechanical force. This may be linked to the complex phase diagram that is thought to exist for this highly polymorphic material (see Figure 5.13).

Although DNAN-VI contains a layered motif of molecules in the crystal structure it cannot be expected that this would be a more insensitive polymorph. One important example to consider which highlights the sensitivity of layered EMs are those of triaminotrinitrobenzene (TATB) and hexanitrobenzene (HNB), two structurally similar molecules which both exhibit layered crystal packing.[63] TATB is highly insensitive to impact, with an impact sensitivity > 120 J, and HNB is sensitive to impact, with an impact sensitivity of 2.75 J. Here the up-pumping model points towards their differences in mechanical impact response lies with the fact that the alternating

amino and nitro groups in TATB form internal hydrogen bonds which lock these functional groups in the plane of the molecule. In HNB the molecule is less rigid, with the doorway region dominated by wagging of the neighbouring -NO_2 groups, which enables the impact energy to be more efficiently transferred into the higher frequency regions, thus rendering HNB as far more sensitive to impact than TATB.[63] Therefore, in DNAN-VI it can be assumed that the change in crystal packing is the driving force in altering the predicted IS. The NCI plots show a startlingly stronger intermolecular interaction in DNAN-VI than when compared to the other DNAN polymorphs. This suggests that the sensitivity of DNAN-VI might follow a similar rationale to TATB – the rigidity of the molecules held within the high pressure polymorph inhibits the up-pumping of the mechanical shock energy.

It can be concluded that the high prediction of the sensitivity of DNAN-I is due to the additional motion related to the non-energetic methoxy group of the molecules of DNAN-I. NCI plots did not suggest any stronger intermolecular interactions which could alter the phonon bath region between the ambient DNAN polymorphs – therefore crystal packing alone cannot account for the increased predicted IS of DNAN-I. It has been shown that DNAN-I experienced the largest reduction in predicted IS when only C-NO_2 motion was considered in the integration portion of the vibrational up-pumping model. An important aspect of future research would be therefore be researching how the vibrational up-pumping method could be optimised to consider vibrational motion only containing a trigger-linkage.

The other important conclusion is that the high-pressure polymorph, DNAN-VI, does not have a significantly increased predicted sensitivity (as was seen with γ-RDX). This is concluded to be due to the layered molecules in the high-pressure structure which are held more tightly in place *via* stronger intermolecular interactions, as highlighted by the results of the NCI plots. To further support this finding, the IS of a theoretical DNAN-I structure optimised at 4.5 GPa did not show any increase in predicted IS (indeed, a slight decrease was seen). Therefore, it is unlikely that that this reduced sensitivity, high-pressure polymorph can be accessed through the compression experienced by a material when it undergoes shock testing.

Overall, the IS of DNAN-I is predicted to be slightly more sensitive to mechanical impact than o-TNT, which is counter to experimental expectation, and may point

towards an under sampling of the DoS by restricting the calculation to Γ-point modes only. This point aside, the variation in predicted IS with polymorphic form suggest that, unlike RDX, the higher pressure polymorphs of DNAN are not accessed during BAM fallhammer testing, which may be associated with the complex polymorphic landscape presented by this structure. Overall, this system further highlights the importance of considering polymorphism in relation to understanding and rationalising the impact sensitivities of new materials, and also opens the door to further experimental testing in order to validate the results presented here.

5.3.3. 1,3,5-trinitrotoluene (TNT)

Although DNAN (above) has been proposed as a replacement for trinitrotoluene, investigating the differences of predicted IS of polymorphs of TNT is imperative to understanding structure- property relationships. Unlike what has been shown with RDX and DNAN so far, the polymorphism of TNT is only orientational rather than conformational. Indeed, Vrcelj *et.al.*[22] report that the two polymorphs are effectively large-scale polytypes, that is their crystal structures differ in only one dimension of the unit cell. The two polymorphs known of TNT are o-TNT (orthorhombic) and m-TNT (monoclinic).

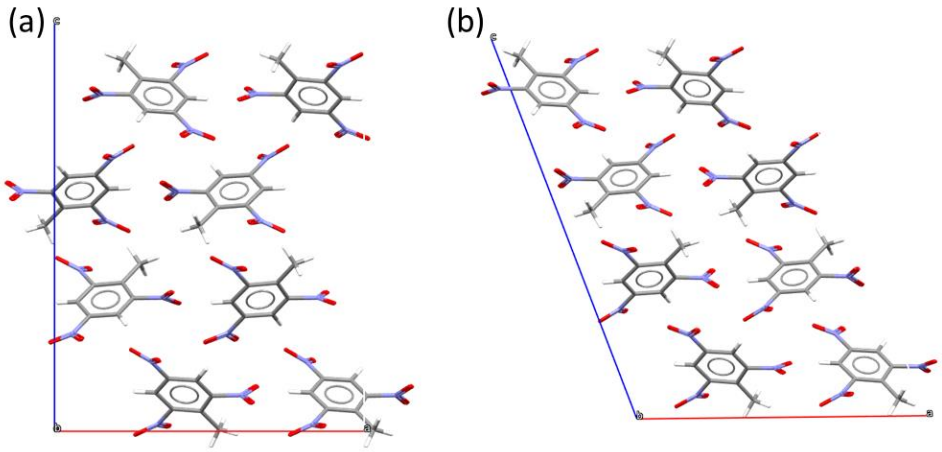

Figure 5.21. The crystal packing of (a) o-TNT and (b) m-TNT

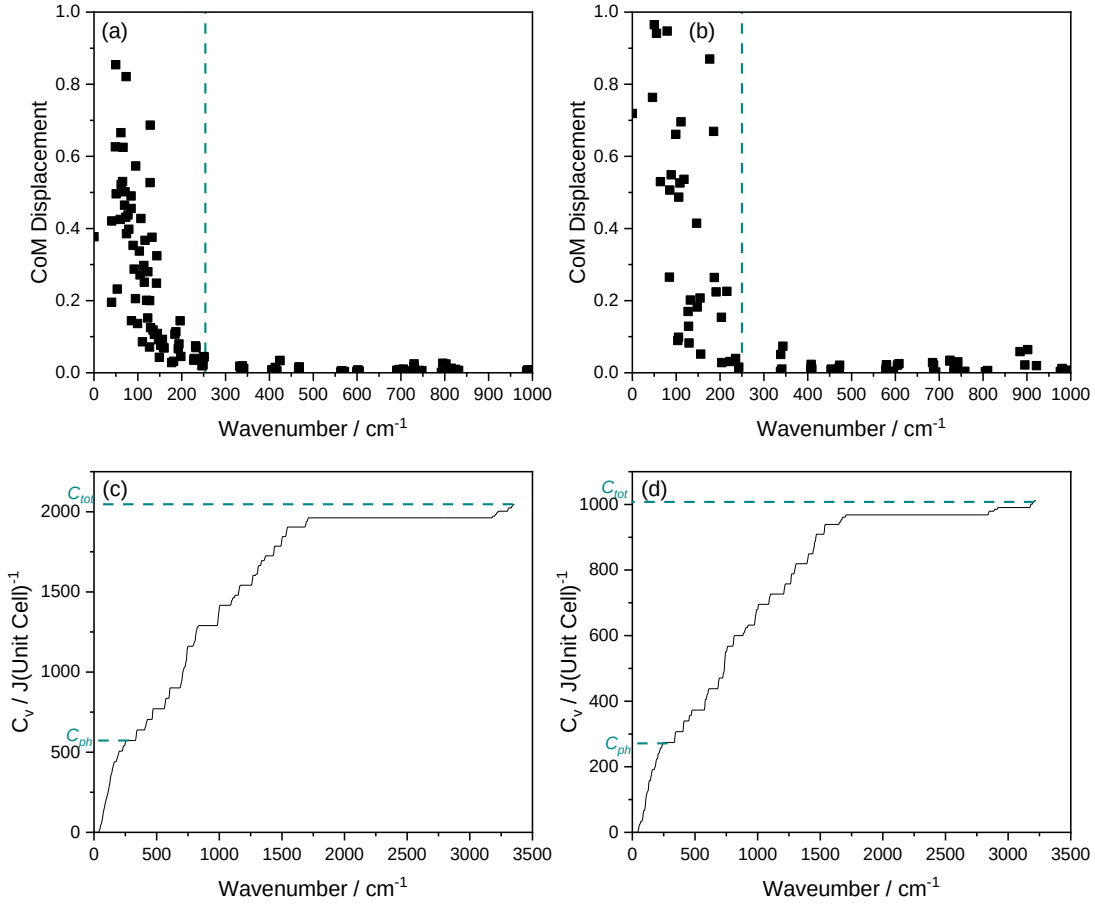

Figure 5.22. CoM displacement of (a) m-TNT and (b) o-TNT. Cumulative heat capacities of the DoS of (c) m-TNT and (d) o-TNT.

It is widely accepted that the commonly occurring polymorph is m-TNT as it is thermodynamically more stable, therefore the reported sensitivity of 24 J is attributed to m-TNT. To carry out vibrational up-pumping analysis, cumulative heat capacities (Figure 5.21) were calculated alongside CoM analysis of the phonon density of states was calculated (Figure 5.22). The value of Ω_{max} varies by 12 cm^{-1} between the two polymorphic forms.

Table 5.6. Values used to calculate the IS of TNT polymorphs

Polymorph	**Ω_{max}**	**Z**	**Y(Z+6)**	**T_{shock} /K**	**Up-pumped density / Z / $\times 10^3$**	**DOPS**
m-TNT	202	8	120	2641	70.1	2.901
o-TNT	226	8	120	2786	64.3	2.699

Due to the similarities in the crystal structures of the two polymorphs, it is unsurprising that the predicted IS of m-TNT is very close to what was predicted for o-TNT. The 2PhonDoS/DoS overlay which is shown in Figure 5.23 shows that both polymorphs show a similar pattern – the peak at *ca.* 250 cm^{-1} is not captured by the up-pumped energy. These results are reassuring as they suggest that both polymorphs would exhibit similar impact sensitivities.

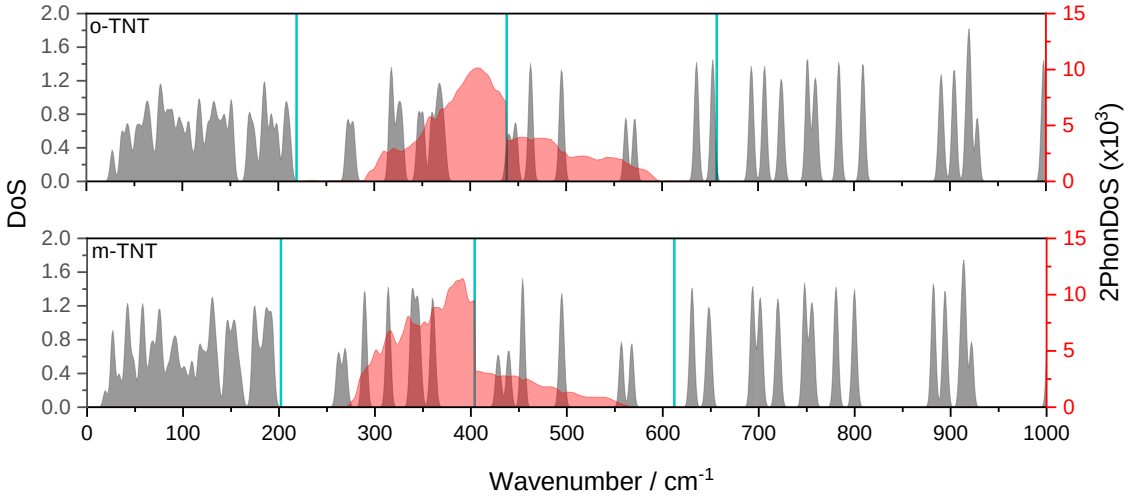

Figure 5.23. 2Phondos (red) and DoS (grey) overlay of o-TNT and m-TNT

Due to the fact that TNT is one of the most well-known EMs, and that both polymorphs have been isolated at ambient conditions, it is initially somewhat surprising that the experimental IS of m-TNT has not been reported. However, the results here suggest that there is a negligible difference between the two polymorphs which is no doubt reassuring to the energetics community.

5.3.4. Nitrotriazalone (NTO)

Nitrotriazalone, as previously highlighted in Chapter 4, is commonly used in insensitive munition formulations. As a well characterised explosive, the α-form of the material has been used to emphasise the reliability of the vibrational up-pumping method to determine impact sensitivity.[61,63] The β-form is known to be metastable at ambient conditions,[14] due to this constraint there is no experimental IS known of β-NTO, however the IS of α-NTO is reported to be 73 J which places α-NTO into the insensitive category. Due to the planar nature of the molecule, there is only orientational polymorphism, as is the case with TNT. (Figure 5.24)

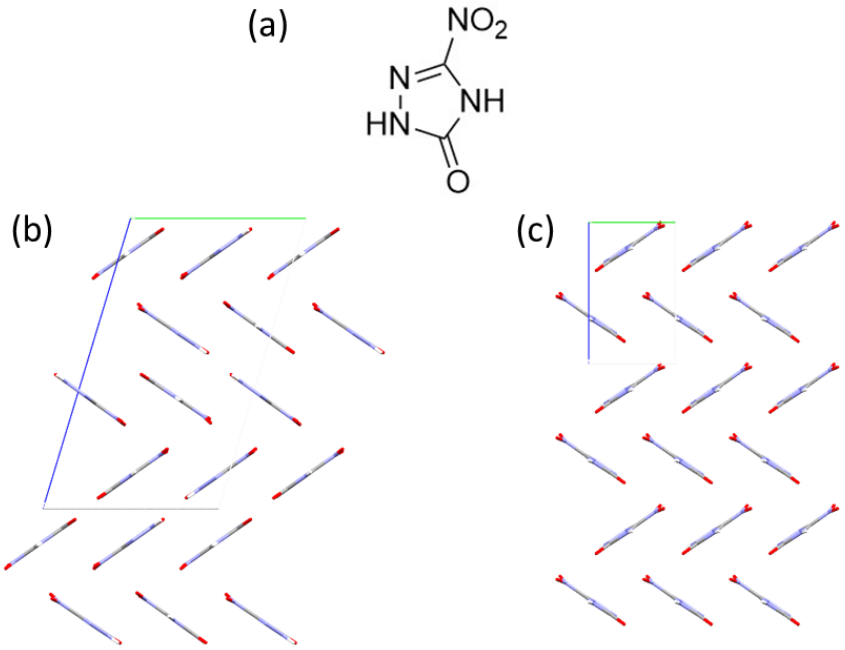

Figure 5.24. showing (a) the molecular structure and crystal packing of (b) α-NTO and (c) β-NTO

In order to calculate the predicted IS, CoM analysis of the phonon DoS was calculated, along with cumulative heat capacities to calculate the shock temperature. (Figure 5.25, Table 5.7)

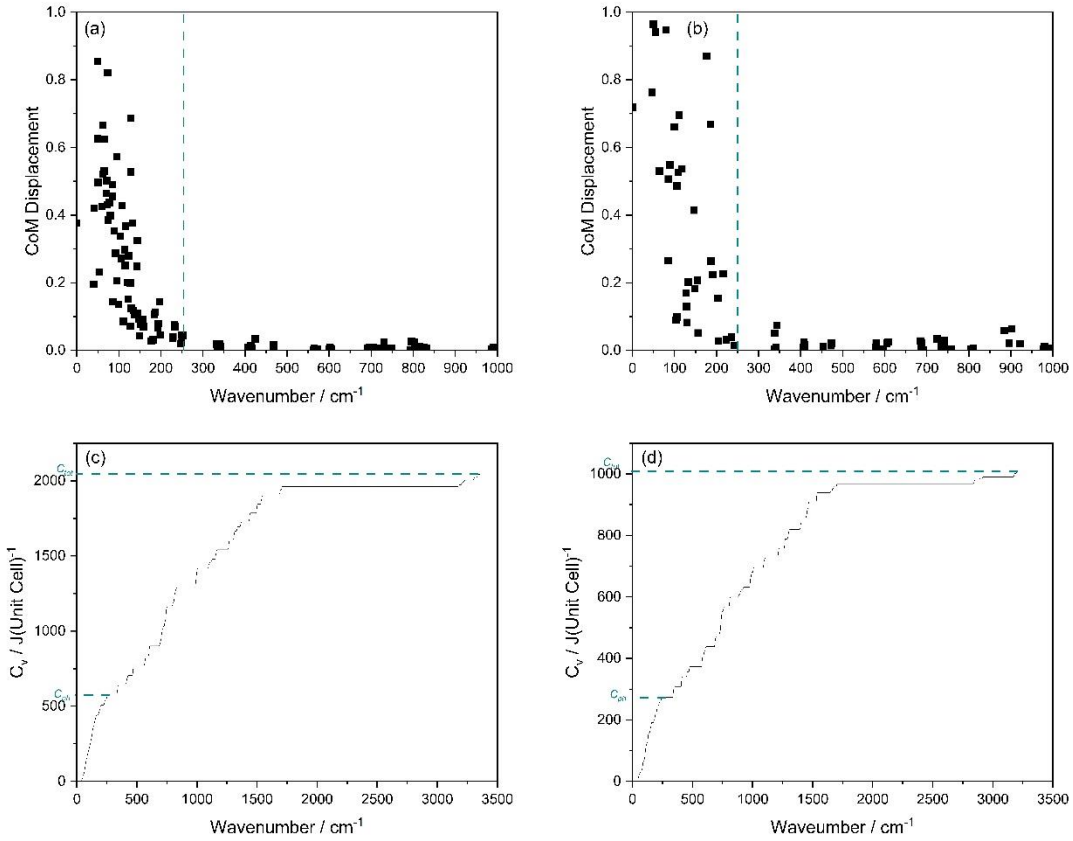

Figure 5.25. CoM displacement for (a) α-NTO and (b) β-NTO and cumulative heat capacity of (c) α-NTO and (d) β-NTO

The cut-off for Ω_{max} is clear cut in this instance for both polymorphs, the displacement dropping significantly beyond *ca* 250 cm^{-1} for both polymorphs. The impact sensitivities of both polymorphs were calculated and give similar predicted sensitivities for both polymorphs. The Phonon DoS/2PDoS overlay is shown in figure. The comparison of the DoS above Ω_{max} is similar. Noting that the scales in Figure 5.26a is twice that of 5.26b, this is due to α-NTO having twice the number of molecules per unit cell. Visual comparison of the two figures shows that projected up-pumped energy does not capture the entirety of the underlying mode at 400 cm^{-1} of β-NTO which is possibly contributing to the lower predicted IS of that polymorph.

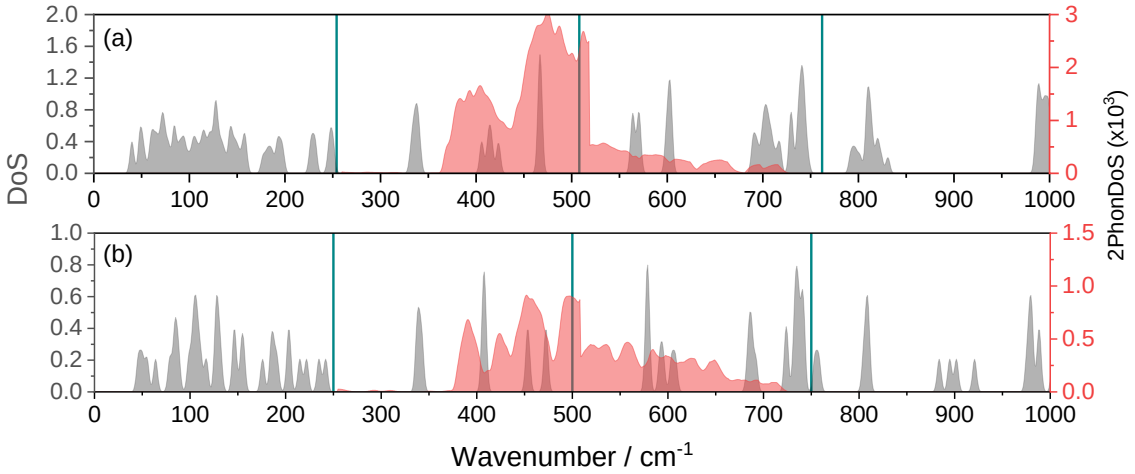

Figure 5.26. DoS (grey) /2PhonDoS (red) overlay of (a) α-NTO and (b) β-NTO

By plotting both results for NTO against experimental sensitivity it shows that β-NTO is expected to be less sensitive to impact than α-NTO. Packing motifs for both polymorphs show a herringbone-like arrangement of the molecules. The small difference in predicted IS between the polymorphic forms follows a similar trend to what has been seen with DNAN and TNT above. Molecules which exhibit less molecular flexibility and therefore are less likely to have more variable lower vibration phonon modes between polymorphs. This "phonon bath region" appears to be a large influence on the predicted IS as it dictates the phonon pathways available for vibrational energy to be up-pumped.

Table 5.7. Features of the polymorphs of NTO that were used to predict their impact sensitivities, and the predicted sensitivities

Polymorph	Ω_{max}	Z	Y(Z+6)	T_{shock} /K	Up-pumped density/Z / $\times 10^3$
α-NTO	250	8	72	2336	12.4
β-NTO	254	4	36	2418	8.66

These results for NTO are important as they show that both polymorphs are expected to be insensitive to impact, a fact which was already established for α-NTO. The nature of this computational method ensured that the sensitivity of materials can be verified without taking potentially dangerous experimental steps. And as is the case with TNT and NTO (Figure 5.27) there is less concern with which

polymorph might be present in a sample, as different polymorphs of the same EM are expected to have similar sensitivities.

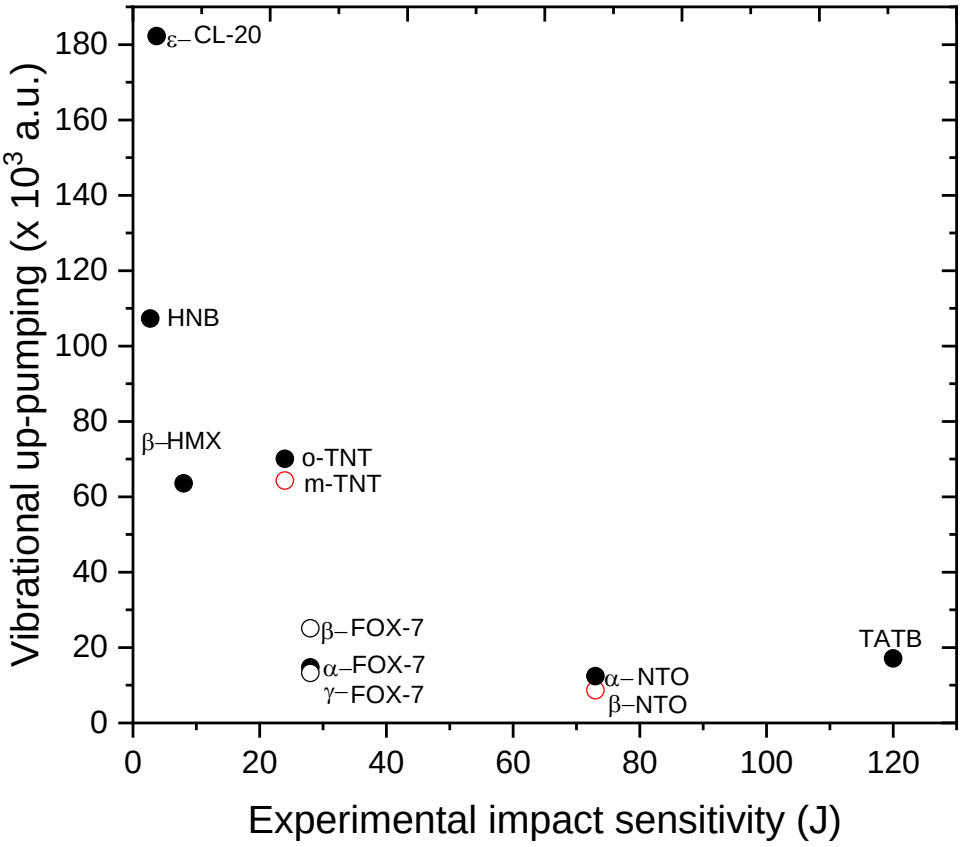

Figure 5.27. Showing the predicted sensitivities of m-TNT and β-NTO (red). Presented alongside the predicted sensitivities of other EMs.

Conclusions

Here the impact sensitivities of polymorphic series have been predicted using the vibrational up-pumping method. The initial focus was on the EM RDX, which is known to exist in several polymorphs. The results here provide an insight into the detonation pathway of α-RDX, postulating that the impact upon the material during testing induced a phase change to the material which results in the IS of α-RDX being under-predicted using the vibrational up-pumping method, as the experimental IS correlates with the predicted IS of γ-RDX.

Next, the highly polymorphic series of DNAN has been investigated, with the high pressure phase of DNAN-VI being investigated for the first time. This high-pressure phase exhibits molecules in a layered system and is predicted to have a sensitivity in

the middle of the range of the polymorphic series. As a layered system, it would be expected for this polymorph to be the most insensitive to impact. However, this was not the case, as DNAN-VI is a high pressure structure (characterised at 4.5 GPa). Calculation of the phonon density of states of this structure results in blue-shift of the vibrational modes compared to ambient polymorphs. This has been shown to typically increase the value of Ω_{max} and subsequently increase the doorway mode region, and the range of modes onto which the 2PhonDoS can be captured. This likely increased the IS of DNAN-VI to a higher level than would initially be expected. The results here show that while DNAN has been proposed as a less sensitive replacement for TNT, only some of the polymorphs are predicted to be less sensitive than TNT, with DNAN-I being predicted as the most sensitive polymorph. If the other, lower sensitivity polymorphs can be isolated and stabilised then DNAN could indeed be seen to be a safer alternative to TNT, while still delivering the same explosive power.

This screening programme has also been utilised to predict the sensitivity of the polymorphs of TNT and NTO. Both of these EMs have one polymorph which have already been investigated through the vibrational up-pumping method and have been used as the reference set to test the vibrational up-pumping method initially. In both cases, the difference in predicted IS between polymorphs of the same EM fell within a 5 arbitrary unit range, which suggests that polymorphs will have similar sensitivities.

Overall, this chapter has shown that the vibrational up-pumping method here overwhelmingly shows that polymorphs of EMs are expected to exhibit different impact sensitivities. This provides powerful implications for the use of these materials in industrial applications. Materials which possess a wide range of predicted IS may be more dangerous to work with, however if a polymorph can be isolated and stabilised then this also provides the implication for being able to tailor the properties of materials for specific applications. However, it may be necessary to carry out further experiments to verify the results presented here. It is known that some of the polymorphs explored in this chapter are able to be isolated, carrying out impact sensitivity testing on these polymorphs will be able to further verify the results presented here and pave the way for this impact sensitivity prediction tool to be implemented in a computational screening programme.

The significance of DNAN not fitting to the established IS/up-pumped density trendline also highlights the need to go back and reassess the current up-pumping model to see if it can be improved by considering projection of 2PhonDoS onto modes which only contain trigger linkage motion as the first port of call. As well as investigating the computational model, this also highlights the necessity for high-quality experimental data to be collected for EMs which are used in the development of computational predictive models.

This chapter also highlights that using the vibrational up-pumping method as part of a larger computational screening method will be a valuable. Crystal structure prediction is a powerful tool to predict the crystal structure given a molecular structure. This process provides a range of possible crystal structures which differ in energy by as little as 5 kJ mol^{-1} , a similar range to naturally occurring polymorphs. Therefore, as part of a computational screening programme it may be difficult to achieve one numerical value of predicted IS, rather a range of sensitivities can be provided. The reliability of the predictive nature of the vibrational up-pumping method ensured that an accurate range of sensitives can be predicted, which will reduce physical resources when developing new EMs.

References

1 J. Haleblian and W. McCrone, Pharmaceutical applications of polymorphism, *J. Pharm. Sci.*, 1969, **58**, 911–929.

2 W. McCrone, *Physics and Chemistry of the Organic Solid State*, Interscience Publishers, New York, 1965.

3 J. Bernstein, *Polymorphism in Molecular Crystals*, Oxford University Press, 2010, vol. 9780199236565.

4 D. J. Kempf, K. C. Marsh, J. F. Denissen, E. McDonald, S. Vasavanonda, C. A. Flentge, B. E. Green, L. Fino, C. H. Park, X. P. Kong, N. E. Wideburg, A. Saldivar, L. Ruiz, W. M. Kati, H. L. Sham, T. Robins, K. D. Stewar, A. Hsu, J. J. Plattner, J. M. Leonard and D. W. Norbeck, ABT-538 is a potent inhibitor of human immunodeficiency virus protease and has high oral bioavailability in humans., *Proc. Natl. Acad. Sci. U. S. A.*, 1995, **92**, 2484.

5 J. Nyman and G. M. Day, Static and lattice vibrational energy differences between polymorphs, *CrystEngComm*, 2015, **17**, 5154–5165.

6 W. Cabri, P. Ghetti, G. Pozzi and M. Alpegiani, Polymorphisms and patent, market, and legal battles: Cefdinir case study, *Org. Process Res. Dev.*, 2007, **11**, 64–72.

7 P. Ravi, D. M. Badgujar, G. M. Gore, S. P. Tewari and A. K. Sikder, Review on Melt Cast Explosives, *Propellants, Explos. Pyrotech.*, 2011, **36**, 393–403.

8 F. P. Bowden and A. Yoffe, Hot spots and the initiation of explosion, *Symp. Combust. Flame, Explos. Phenom.*, 1948, **3**, 551–560.

9 A. T. Nielsen, A. P. Chafin, S. L. Christian, D. W. Moore, M. P. Nadler, R. A. Nissan, D. J. Vanderah, R. D. Gilardi, C. F. George and J. L. Flippen-Anderson, Synthesis of polyazapolycyclic caged polynitramines, *Tetrahedron*, 1998, **54**, 11793–11812.

10 D. I. A. Millar, H. E. Maynard-Casely, A. K. Kleppe, W. G. Marshall, C. R. Pulham and A. S. Cumming, Putting the squeeze on energetic materials—structural characterisation of a high-pressure phase of CL-20, *CrystEngComm*, 2010, **12**, 2524–2527.

11 H. H. Cady, A. C. Larson, D. T. Cromer and IUCr, The crystal structure of α-HMX and a refinement of the structure of β-HMX, *Acta Crystallogr.*, 1963, **16**, 617–623.

12 R. E. Cobbledick and R. W. H. Small, The crystal structure of the δ-form of 1,3,5,7-tetranitro-1,3,5,7-tetraazacyclooctane (δ-HMX), *Acta Crystallogr. Sect. B Struct. Crystallogr. Cryst. Chem.*, 1974, **30**, 1918–1922.

13 B. L. Korsunskii, S. M. Aldoshin, S. A. Vozchikova, N. I. Golovina, N. V. Chukanov and G. V. Shilov, A new crystalline HMX polymorph: ε-HMX, *Russ. J. Phys. Chem. B 2010 46*, 2011, **4**, 934–941.

14 N. Bolotina, K. Kirschbaum and A. A. Pinkerton, Structural Science Energetic materials: a-NTO crystallizes as a four-component triclinic twin, *Acta Cryst*,

2005, **61**, 577–584.

15 N. B. Bolotina, E. A. Zhurova and A. A. Pinkerton, Energetic materials: variable-temperature crystal structure of b-NTO, *J. Appl. Crystallogr.*, 2003, **36**, 280–295.

16 J. Evers, T. M. Klapötke, P. Mayer, G. Oehlinger and J. Welch, α- and β-FOX-7, polymorphs of a high energy density material, studied by X-ray single crystal and powder investigations in the temperature range from 200 to 423 K, *Inorg. Chem.*, 2006, **45**, 4996–5007.

17 M. J. Crawford, J. Evers, M. Göbel, T. M. Klapötke, P. Mayer, G. Oehlinger and J. M. Welch, γ-FOX-7: Structure of a High Energy Density Material Immediately Prior to Decomposition, *Propellants, Explos. Pyrotech.*, 2007, **32**, 478–495.

18 C. S. Choi and E. Prince, The crystal structure of cyclotrimethylenetrinitramine, *Acta Crystallogr. Sect. B Struct. Crystallogr. Cryst. Chem.*, 1972, **28**, 2857–2862.

19 D. I. A. Millar, I. D. H. Oswald, D. J. Francis, W. G. Marshall, C. R. Pulham and A. S. Cumming, The crystal structure of β-RDX—an elusive form of an explosive revealed, *Chem. Commun.*, 2009, **5**, 562–564.

20 A. J. Davidson, I. D. H. Oswald, D. J. Francis, A. R. Lennie, W. G. Marshall, D. I. A. Millar, C. R. Pulham, J. E. Warren and A. S. Cumming, Explosives under pressure—the crystal structure of γ-RDX as determined by high-pressure X-ray and neutron diffraction, *CrystEngComm*, 2008, **10**, 162–165.

21 D. I. A. Millar, I. D. H. Oswald, C. Barry, D. J. Francis, W. G. Marshall, C. R. Pulham and A. S. Cumming, Pressure-cooking of explosives—the crystal structure of ε-RDX as determined by X-ray and neutron diffraction, *Chem. Commun.*, 2010, **46**, 5662–5664.

22 R. M. Vrcelj, J. N. Sherwood, A. R. Kennedy, H. G. Gallagher and T. Gelbrich, Polymorphism in 2-4-6 Trinitrotoluene, *Cryst. Growth Des.*, 2003, **3**, 1027–1032.

23 B. A. Steele, S. M. Clarke and M. P. Kroonblawd, Pressure-induced phase transition in 1,3,5- triamino-2,4,6-trinitrobenzene (TATB), *Appl. Phys. Lett*, 2019, **114**, 191901.

24 B. W. Asay, B. F. Henson, L. B. Smilowitz, P. M. Dickson and B. W. Asay Bryan F Henson Laura B Smilowitz P M Dickson, On the Difference in Impact Sensitivity of Beta and Delta HMX On the Difference in Impact Sensitivity of Beta and Delta HMX, *Energ. Mater.*, 2003, **21**, 223–235.

25 A. A. L. Michalchuk, S. Rudić, C. R. Pulham and C. A. Morrison, Predicting the impact sensitivity of a polymorphic high explosive: the curious case of FOX-7, *Chem. Commun.*, 2021, **57**, 11213–11216.

26 F. P. A. Fabbiani and C. R. Pulham, High-pressure studies of pharmaceutical compounds and energetic materials, *Chem. Soc. Rev.*, 2006, **35**, 932–942.

27 D. D. Dlott and M. D. Fayer, Shocked molecular solids: Vibrational up pumping, defect hot spot formation, and the onset of chemistry, *J. Chem. Phys.*, 1998, **92**, 3798.

28 E. I. Mareevv and F. V. Potemkin, Dynamics of Ultrafast Phase Transitions in (001) Si on the Shock-Wave Front, *Int. J. Mol. Sci.*, 2022, **23**, 2115.

29 G. M. Day, Current approaches to predicting molecular organic crystal structures, *Crystallogr. Rev.*, 2011, **17**, 3–52.

30 S. L. Price, Predicting crystal structures of organic compounds, *Chem. Soc. Rev.*, 2014, **43**, 2098–2111.

31 D. H. Bowskill, I. J. Sugden, S. Konstantinopoulos, C. S. Adjiman and C. C. Pantelides, Crystal Structure Prediction Methods for Organic Molecules: State of the Art, *Annu. Rev. Chem. Biomol.*, 2021, **12**, 593–623.

32 C. R. Groom, I. J. Bruno, M. P. Lightfoot and S. C. Ward, The Cambridge structural database, *Acta Crystallogr. Sect. B Struct. Sci. Cryst. Eng. Mater.*, 2016, **72**, 171–179.

33 J. E. Arnold, I. L. Christopher, C. A. Morrison and G. M. Day, Structure Prediction and Energy-Structure-Function Maps of Energetic Materials, *Unpubl. Work*.

34 S. J. Clark, M. D. Segall, C. J. Pickard, P. J. Hasnip, M. J. Probert, K. Refson and M. C. Payne, First principles methods using CASTEP, *Zeitschrift fuer Krist.*, 2005, **220**, 567–570.

35 A. Tkatchenko and M. Scheffler, Accurate molecular van der Waals interactions from ground-state electron density and free-atom reference data, *Phys. Rev. Lett.*, 2009, **102**, 073005.

36 A. Otero-de-la-Roza, M. A. Blanco, A. M. Pendás and V. Luaña, Critic: a new program for the topological analysis of solid-state electron densities, *Comput. Phys. Commun.*, 2009, **180**, 157–166.

37 A. Otero-De-La-Roza, E. R. Johnson and V. Luaña, Critic2: A program for real-space analysis of quantum chemical interactions in solids, *Comput. Phys. Commun.*, 2014, **185**, 1007–1018.

38 K. Refson, P. R. Tulip and S. J. Clark, Variational density-functional perturbation theory for dielectrics and lattice dynamics, *Phys. Rev. B - Condens. Matter Mater. Phys.*, 2006, **73**, 155114.

39 J. Binns, M. R. Healy, S. Parsons and C. A. Morrison, Assessing the performance of density functional theory in optimizing molecular crystal structure parameters, *Acta Crystallogr. Sect. B Struct. Sci. Cryst. Eng. Mater.*, 2014, **70**, 259–267.

40 M. Jaidann, H. Abou-Rachid, X. Lafleur-Lambert and J. Brisson, Atomistic studies of RDX and FOX-7-Based Plastic-Bonded explosives: molecular dynamics simulation, *Procedia Comput. Sci.*, 2011, **4**, 1177–1185.

41 L. Whinnery, A. Nissen, P. Keifer and A. Tyson, *Imaging Indicator for ESD Safety Testing* , 2013.

42 R. M. Doherty and D. S. Watt, in *Propellants, Explosives, Pyrotechnics*, John Wiley & Sons, Ltd, 2008, vol. 33, pp. 4–13.

43 P. Hakey, W. Ouellette, J. Zubieta and T. Korter, Redetermination of cyclo-trimethylene-trinitramine, *Acta Crystallogr. Sect. E Struct. Reports Online*, 2008, **64**, o1428–o1428.

44 J. A. Ciezak, T. A. Jenkins, Z. Liu and R. J. Hemley, High-Pressure Vibrational Spectroscopy of Energetic Materials: Hexahydro-1,3,5-trinitro-1,3,5-triazine, *J. Phys. Chem. A*, 2006, **111**, 59–63.

45 Jmol: an open-source Java viewer for chemical structures in 3D., http://www.jmol.org/.

46 Y. Tao, W. Zou and S. Nanayakkara, LModeA-nano: A PyMOL plugin for Calculating Bond Strength in Solids, Surfaces and Molecules via Local Vibrational Mode Analysis, *J. Chem. Theory Comput.*, 2022, **18**, 1821–1837.

47 W. Zou, Y. Tao, M. Freindorf, M. Makos, N. Verma and E. Kraka, 2020.

48 S. Hunter, P. L. Coster, A. J. Davidson, D. I. A. Millar, S. F. Parker, W. G. Marshall, R. I. Smith, C. A. Morrison and C. R. Pulham, High-pressure experimental and DFT-D structural studies of the energetic material FOX-7, *J. Phys. Chem. C*, 2015, **119**, 2322–2334.

49 J. E. Patterson, Z. A. Dreger and Y. M. Gupta, Shock Wave-Induced Phase Transition in RDX Single Crystals, *J. Phys. Chem. B*, 2007, **111**, 10897–10904.

50 T. M. Klapötke, *Energ. Mater.*, 2010.

51 P. J. Davies and A. Provatas, Characterisation of 2,4-Dinitroanisole: An Ingredient for use in Low Sensitivity Melt Cast Formulations.

52 B. M. Rice and J. J. Hare, A quantum mechanical investigation of the relation between impact sensitivity and the charge distribution in energetic molecules, *J. Phys. Chem. A*, 2002, **106**, 1770–1783.

53 P. J. Davies and A. Provatas, *Characterisation of 2,4-Dinitroanisole: An Ingredient for use in Low Sensitivity Melt Cast Formulations*, 2006.

54 W. Qian, X. Chen and G. Luo, Polymer reinforced DNAN/RDX energetic composites: Interfacial interactions and mechanical properties, *Cent. Eur. J. Energ. Mater.*, 2017, **14**, 726–741.

55 R. Meyer, J. Köhler and A. Homburg, *Explosives*, Wiley-VCH, 6th edn., 2005, vol. 377.

56 H. Takahashi and R. Tamura, Low temperature phase transition induced biaxial negative thermal expansion of 2,4-dinitroanisole, *CrystEngComm*, 2015, **17**, 8888–8896.

57 P. Coster, C. Henderson, S. Hunter, W. Marshall and C. Pulham, Explosives at Extreme Conditions: Polymorphism of 2,4-Dinitroanisole, *Acta Crystallogr. Sect. A Found. Adv.*, 2014, **70**, C896–C896.

58 X. Li, Z. Tang, X. Zhang and X. Yang, The heats of formation in a series of nitroester energetic compounds: A theoretical study, *J. Hazard. Mater.*, 2009, **165**, 372–378.

59 R. Bu, Y. Xiong and C. Zhang, π-πStacking Contributing to the Low or

Reduced Impact Sensitivity of Energetic Materials, *Cryst. Growth Des.*, 2020, **20**, 2824–2841.

60 Y. Xiong, K. Zhong and C. Zhang, Trigger linkage mechanism: Two or multiple steps initiate the spontaneous decay of energetic materials, *Energ. Mater. Front.*, 2022, **3**, 38–46.

61 A. A. L. Michalchuk, J. Hemingway and C. A. Morrison, Predicting the impact sensitivities of energetic materials through zone-center phonon up-pumping, *J. Chem. Phys.*, 2021, **154**, 1–11.

62 S. Jing, Z. Jiang, Q. Jiao, Z. Li, Y. Liu and L. Yang, 3,5-difluoro-2,4,6-trinitroanisole: promising melt-cast insensitive explosives instead of TNT, *J. Energ. Mater.*, 2022, **40**, 206–217.

63 A. A. L. Michalchuk, M. Trestman, S. Rudić, P. Portius, P. T. Fincham, C. R. Pulham and C. A. Morrison, Predicting the reactivity of energetic materials: An: ab initio multi-phonon approach, *J. Mater. Chem. A*, 2019, **7**, 19539–19553.

Chapter 6 – Conclusions and Future Work

The overarching aim and theme of this thesis has been to understand how the development of a fully computational screening programme would work for the screening of new, and theorised energetic materials. This work has focused on both the properties which can be predicted for energetic molecules and the properties of solid EMs, focusing in the latter on how novel methods alter the properties of EMs.

Chapter 3 began with the problem which has long plagued the energetics community, which method is best suiting for predicting, and calculating the heat of formation of energetic materials? Robust methods have been proposed over the years to best calculate the gas phase heat of formation for energetic molecules, including isodesmic equations, group equivalence, and semi-empirical methods. All three methods were evaluated in this work across a range of 19 HCNO containing molecules. For the semi-empirical, PM7 method which is more robust a further XY molecules were included in the test set to calculate $\Delta H_{f(g)}$. All methods were shown to work well, which is supported by the literature. The standard heat of formation is required in software, such as EXPLO-5 and CHEETAH, to predict the detonation parameters of EMs. More often than not this is the solid heat of formation. Therefore alongside $\Delta H_{f(g)}$ calculations, $\Delta H_{sub,}$ or $\Delta H_{Lattice}$ calculations are also required to obtain $\Delta H_{f(s).}$ Work has previously been carried out to calculate ΔH_{sub} for single component molecular solids (using semi-empirical methods utilising the calculated electrostatic potential surface of the isolated molecule) and $\Delta H_{Lattice}$ for salts (Using the semi-empirical method devised by Jenkins *et. al.*). However there was a significant gap, that being the calculation of ΔH_{sub} for co-crystals, which are systems which are being increasingly used to alter the properties of known EMs (as has been carried out in Chapter 4). Here two methods were compared to calculate the lattice enthalpy, the semi-empirical PIXEL method and the use of dispersion corrected DFT. While comparing both methods it was concluded that the lattice enthalpy calculated using DFT-D provided similar results to when summing the ΔH_{sub} of the co-formers. While this is provides slightly more error to the results this still provides a quicker method with only a small compromise on accuracy of results. The summation of

these methods will enable experimentalists and computational chemists alike to quickly calculate the heat of formation for the EMs they are working with.

Chapters 4 and 5 focused on using a previously developed method for predicting the impact sensitivity of EMs, to elucidate structure property relationships and to assess how this method could work in a fully computational screening programme. Chapter 4 focused on using this method to assess a co-crystal of an energetic material, NTO and a non-energetic, 4,4-bipyridine (BIPY). Additionally in this chapter, the use of computational modelling was implemented to further the understand the system with regards to its behaviour under high pressures and the subsequent proposed co-crystal-salt transformation. Fitting of 1D Schrodinger Equations to potential energy surfaces of the NH…N vector in NTO.BIPY confirmed that there is no proton transfer occurring at high pressures. Instead, the system can be classified as a proton migration system, confirmed by the N-H bond lengthening by only 0.07 Å at 5.93 GPa. The pressure induced colour change of white to yellow was confirmed to be simply a direct result of unit cell compression, confirmed through calculation of the band gap of the ambient and high pressure structures.

Finally the vibrational up-pumping method was used to predict the impact sensitivities of two highly polymorphic energetic materials, RDX and DNAN. These results showed that the IS is highly dependant upon the crystal packing of the material, and also led to the realisation that polymorphs which exist at high pressures can be expected to be more sensitive to impact than their ambient pressure systems when molecules display a high amount of flexiblity. A high pressure DNAN polymorph, DNAN-VI was presented here which exhibits the molecules packed in a parallel layers. The sensitivity of this high-pressure polymorph is in line with the other ambient-pressure polymorphs, which is a change from what is expected for EMs characterised under high pressure. However, the parallel layers appear to be the domineering factor in the IS, and this ensures the lower sensitivity of this, as yet, un-published polymorph. The outlying predicted sensitivities of DNAN also suggest that further optimisation of the vibrational up-pumping method is required before relying solely on these results. The sensitivities of polymorphs of NTO and TNT have also been predicted, and it appears that for these less flexible molecules, with similar crystal packing the sensitivity between polymorphs does not

significantly change, which is a reassuring result considering the widespread use of these materials.

Future Work

This thesis has focused on two key steps in a proposed computational screening programme for new energetic materials. With this, it would stand to reason that this screening programme should now be provided with a test case to assess its viability. Working with synthetic chemists, a test EM could be devised on paper (where there is further ongoing work based around the rational design of energetic molecules). This can then be fed through the crystal structure prediction to find a range of potential crystal structures. Using the density of the lowest energy structure, the methods proposed in Chapter 3 can then be used to calculate the condensed heat of formation. Thus, the energetic performance of the hypothesised material can be predicted using software such as EXPLO-5. The impact sensitivity of this proposed material can be calculated taking the CSP calculated structure as an input into the vibrational up-pumping method. Experimental validation is then vital to this process. The hypothesised material should be synthesised, its crystal structure determined and its sensitivity tested. The results from this would then provide either validation to the proposed computational screening programme, or highlight any gaps that are in the proposed screening programme. This would be the first instance of all properties of a hypothesised EM being calculated before a material is even synthesised. This screening programme will pave the way for the rational design of new materials with the focus on reducing waste during the design process, manufacturing safer materials and focusing on an environmentally conscious scheme. This will result in the important intersection of the powers of computational chemistry aiding the design of new energetic materials.

Appendices

Table 1. Experimental and computed $\Delta H_{f(g)}$ and $\Delta H_{f(s)}$ values

		ΔHf(g) (kJ mol^{-1})				**ΔH_{sub}** (kJ mol^{-1})	**ΔH_L** (kJ mol^{-1})	**ΔHf(s)** (kJ mol^{-1})	
	Molecule	Experimental [Ref]	Calculated Isodesmic	Calculated Atom Equivalence	Calculated PM7	Calculated	Calculated	Experimental [Ref]	Calculated
1	Pentaerythritoltetranitrate (PETN)	–386.6[1]	-279.7	-394.5	-477.8	134.5	-139.45	-538.1[2]	-612.4
2	Trimethylolethanetrinitrate (TMETN)	–361.7[3]	-253.6	-338.0	-399.3	–	–	–	–
3	Nitroglycerin	–279.1[4]	-306.3	-296.2	-343.2	101.6	-106.55	-380.0[5]	-444.8
4	Urea	-235.5[6]	-174.1	-171.7	-221.5	81.9	-86.85	-333.2[6]	-303.4
5	2–methyl–2–nitropropane	–177.0[7]	-207.9	-173.6	-190.8	62.8	-67.75	-230.0[7]	-253.6
6	t–butyl nitrite	–171.5[7]	-169.3	-153.5	-159.1	–	–	–	–
7	Ethyl nitrate	–154.8[8]	-156.7	-165.2	-168.9	–	–	–	–
8	n–butylnitrite	–145.6[7]	-141.8	-150.0	-159.0	–	–	–	–
9	2–nitrophenol	–132.2[9]	-115.2	-95.5	-129.2	76.1	-81.05	-199.3[9]	-205.3
10	Propyl nitrite	–118.8[7]	-120.9	-117.6	-138.3	–	–	–	–
11	4–nitrophenol	–114.6[9]	-145.5	-77.0	-122.6	99.5	-104.45	-226.7[9]	-222.2
12	3–nitrophenol	–109.2[9]	-140.1	-68.8	-110.7	98.4	-103.35	-200.5[9]	-209.1
13	Nitrobenzene	68.5[10]	51.6	48.5	73.6	–	–	–	–
14	Tetranitromethane	82.4[11]	82.1	80.4	119.9	57.5	-62.45	36.8[11]	62.3
15	3–azido–3–ethylpentane	169.9[12]	157.9	144.3	160.9	–	–	–	–
16	Hexanitroethane	179.1[13]	149.6	139.7	199.9	76.6	-81.55	117.2[13]	123.3
17	1,3,5–Trinitro–1,3,5–triazinane (RDX)	191.6[14]	157.1	189.5	124.4	95.2	-100.15	62.0[15]	29.2
18	1–azido–1,1–dinitroethane	252.7[16]	298.0	241.7	296.5	–	–	–	–
19	Acridine	272.0[17]	268.2	267.2	300.2	91.0	-95.95	179.4[17]	209.1
20	Azidotrinitomethane	352.7[16]	333.6	336.0	399.5	–	–	–	–
21	Hexanitrohexaazaisowurtzitane	–	–	–	441.68	150.0	-154.95	377.4[18]	291.7

	(CL-20)								
22	Octogen (HMX)	–	–	–	185.6	117.7	-122.65	87.9[19]	68.0
23	Titanium (IV) *sec*-butoxide	-1598.3[20]	–	–	-1648.0	–	–	–	–
24	ZrF_4	-1673.6[21]	–	–	-1469.8	–	–	–	–
25	SiF_4	-1615[22]	–	–	-1526.5	–	–	–	–
26	TeF_6	-1318.0[23]	–	–	-1132.0	–	–	–	–
27	SF_6	-1220.5[23]	–	–	-1218.2	–	–	–	–
28	ReF_6	-1142.2[24]	–	–	-1078.1	–	–	–	–
29	SeF_6	-1117[25]	–	–	-1031.4	–	–	–	–
30	$Mn(CO)_5Br$	-876.0[26]	–	–	-831.3	96.7	-101.65	-970[26]	-928.0
31	$Fe(CO)_5$	-723.8[21]	–	–	-771.3	–	–	–	–
32	$Cu(acac)_2$	-652.7[27]	–	–	-775.5	117.2	-122.15	-784.8[28]	-892.7
33	$ZrBr_4$	-646.0[21]	–	–	-581.6	–	–	–	–
34	$TiBr_4$	-550.2[29]	–	–	-508.0	49.0	-53.95	-616.7[30]	-557.0
35	$Mn(CO)_3$ η^5-cyclopentadiene	-475.5[29]	–	–	-220.0	84.1	-89.05	-528.1[26]	-304.1
36	SO_3	-395.8[29]	–	–	-423.6	–	–	–	–
37	$Cr(CO)_6\eta^6$-toluene	-380.0[31]	–	–	-380.3	98.2	-103.15	-473.0[31]	-478.5
38	AlF	-265.7[29]	–	–	-239.4	–	–	–	–
39	$SnCl(CH_3)_3$	-195.0[32]	–	–	-172.7	–	–	–	–
40	RuO_4	-180.8[21]	–	–	-130.9	–	–	–	–
41	*cis*-platin	-172.8[21]	–	–	-175.5	–	–	–	–
42	Nickel(II) diethyldithiocarbamate	–	–	–	103.9	126.8	-131.75	-118.4[33]	-70.7
43	$Hg(CH_2CH_3)Cl$	-77.8[34]	–	–	-58.9	–	–	–	–
44	$Ga(CH_3)_3$	-46.2[29]	–	–	-51.6	49.4	-54.35	-93.6[35]	-101.0
45	$Hg(CH_2CH_3)Br$	-44.3[34]	–	–	-32.7	–	–	–	–
46	$Hg(CH_2CH_3)I$	3.34[34]	–	–	10.2	–	–	–	–
47	ICl	17.5[29]	–	–	21.1	–	–	–	–

48	1,2-dibromobenzene	128.9[36]	–	–	132.6	–	–	–	–
49	$Pb(CH_3)_4$	136.1[37]	–	–	108.8	–	–	–	–
50	$Pb(Ph)_2Br_2$	177.7[38]	–	–	280.4	–	–	–	–
51	Diphenyl diselenide	237.0[39]	–	–	244.4	110.5	-115.45	120.6[39]	133.9
52	ferrocene	242.2[21]	–	–	231.5	71.4	-76.35	158.4[40]	160.1
53	$Pb(Ph)_4$	674.1[38]	–	–	693.5	–	–	–	–
–	benzotris[c]furazan-2-oxide (BTF)	–	–	–	697.6	92.6	-97.55	–	605.0
–	1-methyl-3,5-dinitropyrazole (MDNP)	–	–	–	340.3	88.7	-93.65	–	251.6
–	1-methyl-2,4,5-trinitropyrazole (MTNP)	–	–	–	282.2	94.0	-98.95	–	188.3
–	3,5-dinitropyrazole (DNP)	–	–	–	211.8	82.7	-87.65	–	129.0
–	3-bromopyridine (BrPyr)	–	–	–	153.3	70.1	-75.05	–	83.2
–	2,4,6-trinitrotoluene (TNT)	–	–	–	49.7	96.0	-100.95	–	-46.2
–	3-amino-2-chloropyrdine (AmClPyr)	–	–	–	98.3	85.1	-90.05	–	13.2
–	1-nitronapthalene (NNP)	–	–	–	164.8	93.6	-98.55	–	71.2
–	Picric acid (PIC)	–	–	–	-102.9	96.4	-101.35	–	-199.3
–	9-bromoanthracene (BRA)	–	–	–	283.7	93.8	-98.75	–	190.0
–	1,3,5-trinitrobenzene (TNB)	–	–	–	82.6	89.6	-94.55	–	-6.8
–	2,3-diaminetoluene (DAT)	–	–	–	65.8	82.8	-87.75	–	-17.0

Table 2. The isodesmic equations used to calculate gas phase heats of formation of molecules **1**-**20**

Compound No.	Isodesmic reaction
1	$C(CH_3)_4 + 4\ CH_3ONO_2 \rightarrow 4\ CH_4 + C(CH_2ONO_2)_4$
2	$C(CH_3)_4 + 3\ CH_3ONO_2 \rightarrow 3\ CH_4 + C(CH_2ONO_2)_3(CH_3)$
3	$3\ CH_3CH_2CH_2NO_2 \rightarrow 2\ CH_3CH_2CH_3 + CHONO_2(CH_2ONO_2)_2$
4	$2\ CH_3NO \rightarrow H_2N(CO)NH_2 + CH_2O$
5	$CH_3CH_2CH_2NO_2 + CH(CH_3)_3 \rightarrow C(CH_3)_3NO_2 + CH_3CH_2CH_3$
6	$CH(CH_3)_3 + CH_3CH_2CH_2ONO \rightarrow C(CH_3)_3ONO + CH_3CH_2CH_3$
7	$CH_3CH_3 + CH_3ONO_2 \rightarrow CH_3CH_2ONO_2 + CH_4$
8	$CH_3CH_2CH_2ONO + CH_3CH_2CH_2CH_3 \rightarrow CH_3CH_2CH_3 + CH_3CH_2CH_2CH_2ONO$
9	$C_6H_5OH + C_6H_5NO_2 \rightarrow$ *o*-$HOC_6H_4NO_2 + C_6H_6$
10	$CH_3CH_2CH_3 + CH_3ONO \rightarrow CH_3CH_2CH_2ONO + CH_4$
11	$C_6H_5OH + C_6H_5NO_2 \rightarrow$ *p*-$HOC_6H_4NO_2 + C_6H_6$
12	$C_6H_5OH + C_6H_5NO_2 \rightarrow$ *m*-$HOC_6H_4NO_2 + C_6H_6$
13	$C_6H_6 +$ *m*-$C_6H_4(NO_2)(NH_2) \rightarrow C_6H_5NH_2 + C_6H_5NO_2$
14	$2\ CH_2(NO_2)_2 \rightarrow C(NO_2)_4 + CH_4$
15	$CH_3CH_2CH(CH_2CH_3)CH_2CH_3 + CH_3N_3 \rightarrow CH_4 + CH_3CH_2C(N_3)(CH_2CH_3)CH_2CH_3$
16	$6\ CH_3CH_2NO_2 \rightarrow 5\ CH_3CH_3 + C(NO_2)_3C(NO_2)_3$
17	$3\ C_5H_{10}NNO \rightarrow (CH_2NNO_2)_3 + 2\ C_6H_{12}$
18	$CH_3N_3 + 2\ CH_3CH_3NO_2 \rightarrow CH_3C(NO_2)_2(N_3) + CH_3 + CH_3CH_3$
19	$C_{10}H_8 + C_{13}H_9N \rightarrow C_9H_7N + C_{14}H_{10}$
20	$CH_3N_3 + 3\ CH_3NO_2 \rightarrow C(NO_2)_3(N_3) + 3\ CH_4$

Table 3. Total energy values, zero point energy correction (ZPE) and thermal correction (H_T) to the enthalpy for molecules **1-20**, used for the calculation of gas phase heats of formation using the isodesmic method.

Molecule No.	**Total Energy** (a.u)	**ZPE** (kJ mol^{-1})	**H_T** (kJ mol^{-1})
1	-1316.27	498.04	56.93
2	-1036.61	479.18	47.71
3	-958.03	319.42	40.59
4	-169.84	118.83	12.98
5	-362.83	273.37	14.30
6	-362.83	273.37	14.30
7	-359.43	218.71	18.92
8	-362.82	353.93	24.72
9	-511.85	282.28	23.33
10	-323.53	278.05	21.26
11	-511.86	282.76	23.21
12	-511.86	282.53	23.27
13	-436.64	270.12	18.77
14	-858.36	145.65	30.28
15	-439.75	582.83	31.59
16	-1306.59	228.97	49.20
17	-897.27	376.46	17.45
18	-652.30	219.47	29.55
19	-555.39	479.50	26.83
20	-817.48	148.92	32.89

Table 4. Calculated electronic energies of molecules used to calculate $\Delta H_{f(g)}$ using the atom equivalence method.

Molecule	Calculated energy of molecule (a.u)
1	-1316.46
2	-1036.79
3	-958.16
4	-225.26
5	-362.96
6	-362.96
7	-359.51
8	-362.96
9	-511.98
10	-323.64
11	-511.97
12	-511.97
13	-436.75
14	-858.41
15	-440.12
16	-1306.67
17	-897.41
18	-652.38
19	-555.57
20	-817.53

Table 5. Experimental and calculated $\Delta H_{f(s)}$ for salts, calculated using Jenkins' method.

Compound No.	Salt	Ion 1 $\Delta H_{f(g)}$ - PM7 (kJ mol^{-1})	Ion 2 $\Delta H_{f(g)}$ – PM7 (kJ mol^{-1})	Calculated ΔH_L (kJ mol^{-1})	Experimental $\Delta H_{f(s)}$ (kJ mol^{-1})	Calculated $\Delta H_{f(s)}$ (kJ mol^{-1})
54	Barium nitrate	1654.0	-340.4	1935.3	-992.1[5]	-962.0
55	Barium chlorate	1654.0	-249.0	1872.4	-771.5[5]	-716.4
56	Ammonium nitrate	647.7	-340.4	656.0	-366.1[5]	-348.7
57	Guanylurea dinitramide (FOX-12)	4734.0	-242.3	507.2	-356.2[41]	-275.5
58	Ammonium perchlorate	647.7	-344.8	610.4	-295.8[5]	-307.4
59	Potassium 5,7-dinitro-[2,1,3]-benzoxadiazol-4-olate 3-oxide (KDNP)	561.2	-256.3	482.0	-197.1[42]	-177.0
60	Hydrazinium perchlorate	736.6	-344.7	581.2	-179.5[43]	-189.4
61	Ammonium dinitramide (ADN)	647.7	-242.3	588.2	-148.0[44]	-184.0
62	Dihydroxylammonium 5,5'-bitetrazole-1,1'-dioxide (TKX-50)	587.8	435.5	1498.6	111.3[45]	112.6
63	Ammonium azide	647.7	130.3	663.3	115.6[46]	114.7
64	Lead azide	2089.0	130.3	2088.8	484.5[5]	262.5
65	Copper(I) 5-Nitrotetrazolate (DBX-1)	951.1	65.3	590.4	280.9[45]	426.0
66	3,4-diamino-1,2,4-triaxolium 1-hydroxyl-5-amino-tetrazole (DATr.HATZ)	951.5	102.3	508.6	571.9[5]	545.2
67	Di(1-amino-1,2,3-triazolium) 5,5'-bitetrazole-1,1'-diolate (2ATr.BTO)	1016.5	435.6	1246.6	1273.6[5]	1221.9

Table 6. Lattice energies and heats of formation of co-crystal calculated PIXEL and DFT-D

Compound No.	Structure	ΔH_L PIXEL (kJ mol^{-1})	ΔH_L DFT-D (kJ mol^{-1})	$\Delta H_{f(s)}$ PIXEL (kJ mol^{-1})	$\Delta H_{f(s)}$ DFT-D (kJ mol^{-1})
68	Hexanitrohexaaxaisowurzitane/benzotris[c]furazan-2-oxide (CL-20/BTF)	-228.4	-236.3	910.9	903.0
69	Hexanitrohexaaxaisowurzitane/1-methyl-3,5-dinitropyrazole (CL-20/MDNT)	-259.6	-278.1	522.4	503.9
70	Hexanitrohexaaxaisowurzitane/1-methyl-2,4,5-trinitropyrazole (CL-20/MTNP)	-263.8	-246.9	460.1	477.0
71	3,5-dinitropyrazole/3-bromopyridine (DNP/BrPyr)	-184.4	-188.5	263.8	259.7
72	Hexanitrohexaaxaisowurzitane/2,4,6-trinitrotoluene (CL-20/TNT)	-255.6	-241.3	235.8	250.2
73	3,5-dinitropyrazole/3-amino-2-chloropyrdine (DNP/AmClPyr)	-213.8	-248.5	179.5	144.8
74	2,4,6-trinitrotoluene/1-nitronapthalene (TNT/NNP)	-194.8	-208.0	19.7	6.5
75	Picric acid/9-bromoanthracene (PIC/BRA)	-221.4	-263.2	-40.6	-82.4
76	2,4,6-trinitrotoluene /1,3,5-trinitrobenzene (TNT/TNB)	-190.6	-174.5	-58.1	-42.0
77	2,4,6-trinitrotoluene/2,3-diaminetoluene (TNT/DAT)	-210.6	-267.5	-95.0	-152.0
78	Picric acid/1-nitronapthalene (PIC/NNP)	-182.2	-222.1	-120.3	-160.3

Table 7. Molecules for which the force constants all bonds were calculated, and the force constants that were calculated

Molecule Number (where applicable)	Molecule	Bond types in molecule
1	PETN	CC, CH, CO, NO
2	TMETN	CC, CH, CO, NO
3	Nitroglycerin	CC, CH, CO, NO
4	Urea	CN, NH, CO
5	2-methyl-2-nitropropane	CC, CH, CN, NO
6	t-buytlnitrite	CC, CH, CO, NO
7	Ethylnitrate	CC, CH, CO, NO
8	n-butylnitrite	CC, CH, CO, NO
9	2-nitrophenol	CC, CH, CN, NO, CO
10	Propylnitrite	CC, CH, CO, NO
11	3-nitrophenol	CC, CH, CN, NO, CO
12	4-nitrophenol	CC, CH, CN, NO, CO
13	Nitrobenzene	CC, CH, CN, NO
14	Tetranitromethane	CN, NO
15	3–azido–3–ethylpentane	CC, CH, CN, NN
16	Hexanitroethane	CC, CN, NO
17	1,3,5–Trinitro–1,3,5–triazinane (RDX)	CN, CH, NN, NO
18	1–azido–1,1–dinitroethane	CC, CH, CN, NO, NN
29	Acridine	CC, CH, CN
20	Azidotrinitomethane	CN, NN, NO
-	Hexanitrohexaazaisowurtzitane (CL-20)	CC, CH, CN, NN, NO
-	Octogen (HMX)	CN, CH, NN, NO
-	Hexanitrobenzene	CC, CN, NO
-	Nitrotriazolone (NTO)	CN, NN, CO, NH, NO
-	1,1-diamino-2,2-dinitroethylene (FOX-7)	CC, CN, NO, NH
-	Benzonitrile	CC, CH, CN
-	Cyclooctyne	CC, CH
-	3,4,5-trinitropyrazole	CC, CN, NO, NH
-	3,5-dinitropyrazole	CC, CH, CN, NN, NO
-	1,3-dinitropyrazole	CC, CH, CN, NN, NO
-	TATB	CC, CN, NH, NO

Table 8. Equations for lines of best fit from Figure 5.

Chemical Bond	Equation of best fit	R^2
C–C	$y = 32550e^{\left(-\frac{x}{0.1577}\right)} + 1.914$	0.996
C–H	$y = -43.33x + 52.69$	0.989
C–N	$y = 30250e^{\left(-\frac{x}{0.1567}\right)} + 0.923$	0.980
C–O	$y = 38830e^{\left(-\frac{x}{0.1475}\right)} + 2.341$	0.998
N–N	$y = 37680e^{\left(-\frac{x}{0.1493}\right)} + 0.396$	0.994
N–O	$y = 2536e^{\left(-\frac{x}{0.2307}\right)} - 2.608$	0.993
N–H	$y = -138.1x + 146.7$	0.923

References

1 M. H. Keshavarz, Predicting heats of detonation of explosives via specified detonation products and elemental composition, *Indian J. Eng. Mater. Sci.*, 2007, **14**, 324–330.

2 D. L. Ornellas, J. H. Carpenter and S. R. Gunn, Detonation calorimeter and results obtained with pentaerythritol tetranitrate (PETN), *Rev. Sci. Instrum.*, 1966, **37**, 907–912.

3 R. Meyer, J. Köhler and A. Homburg, *Explosives*, Wiley-VCH, 6th edn., 2005, vol. 377.

4 E. A. Miroshnichenko, L. I. Korchatova and V. Shelaputina, Thermochemistry of Glyceryl Trinitrate, *Bull. Acad. Sci. USSR, Div. Chem. Sci*, 1988, 1778–1781.

5 T. M. Klapötke, *Energetic Materials Encyclopedia*, Berlin, Boston: De Gruyter, 2018.

6 G. Y. Kabo, E. A. Miroshnichenko, M. L. Frenkel, A. A. Kozyro, V. V. Simirskii, A. P. Krasulin, V. P. Vorob'eva and Y. A. Lebedev, Thermochemistry of alkyl derivatives of urea, *Bull. Acad. Sci. USSR Div. Chem. Sci.*, 1990, **39**, 662–667.

7 L. Batt, K. Christie, R. T. Milne and A. J. Summers, Heats of formation of C1□C4 alkyl nitrites (RONO) and their RO-NO bond dissociation energies, *Int. J. Chem. Kinet.*, 1974, **6**, 877–885.

8 P. Gray, M. W. T. Pratt and M. J. Larkin, The latent heat of vaporization and the thermochemistry of ethyl nitrate, *J. Chem. Soc.*, 1956, 210–212.

9 M. Sabbah, R, Gouali, Energies of intra- and inter-molecular bonds in the three nitrophenols, *Aust. J. Chem*, 1994, **47**, 1651–1660.

10 N. D. Lebedeva, Y. A. Katin and G. Y. Akhmedova, Standard enthalpy of formation of nitrobenzene, *Russ. J. Phys. Chem. (Engl. Transl.)*, 1971, **45**, 1192–1193.

11 V. P. Lebedev and Y. N. Miroshnichenko, E A Matyushin, Calorimetric determination of enthalpies of formation of tetranitromethane, *Russ. J. Phys. Chem. (Engl. Transl.)*, 1975, **49**, 1133–1136.

12 G. S. Wayne, G. J. Snyder and D. W. Rodgers, Measurement of the strain energy of a transient bridgehead imine, 4-azahomoadamantan-3-ene, by photoacoustic calorimetry, *J. Am. Chem. Soc.*, 1993, **115**, 9860–9861.

13 V. I. Pepekin, E. A. Miroshnichenko and Y. A. Lebedev, Ethalpy of formation of hexanitroethane, *Russ. J. Phys. Chem. (Engl. Transl.)*, 1968, **42**, 1583–1584.

14 V. I. Pepekin, Y. N. Matuushin and Y. A. Lebedev, Thermochemistry of N-nitro- and N-nitrosoamines of the alicyclic series, *Bull. Acad. Sci. USSR, Div. Chem. Sci1*, 1974, 1707–1710.

15 R. N. Rogers, Thermochemistry of explosives, *Thermochim. Acta*, 1975, **11**, 131–139.

16 P. W. Atkins, *Physical Chemistry*, Oxford University Press, Oxford, 1982.

17 W. V. Steele, R. D. Chirico, I. A. Hossenlopp, A. Nguyen, N. K. Smith and B. E. Gammon, The thermodynamic properties of the five benzoquinolines, *J. Chem. Thermodyn.*, 1989, **21**, 81–107.

18 R. L. Simpson, P. A. Urtiew, D. L. Ornellas, G. L. Moody, K. J. Scribner and D. M. Hoffman, CL-20 performance exceeds that of HMX and its sensitivity is moderate, *Propellants, Explos. Pyrotech.*, 1997, **22**, 249–255.

19 G. Krien, H. H. Licht and J. Zierath, Thermochemische untersuchungen an

nitraminen, *Thermochim. Acta*, 1973, **6**, 465–472.

20 D. C. Bradley and M. J. Hillyer, Thermochemistry of Metal Alkoxides, *Trans. Faraday Soc.*, 1966, **62**, 2377–2381.

21 T. R. Cundari, H. Arturo Ruiz Leza, T. Grimes, G. Steyl, A. Waters and A. K. Wilson, Calculation of the enthalpies of formation for transition metal complexes, *Chem. Phys. Lett.*, 2005, **401**, 58–61.

22 S. W. Benson, Bond Energies, *J. Chem. Educ.*, 1965, **42**, 502–515.

23 D. M. Yost and W. H. Claussen, The Thermochemical Constants of the Hexafluorides of Sulfur, Selenium and Tellurium, *J. Am. Chem. Soc.*, 1933, **55**, 885–891.

24 R. Craciun, D. Picone, R. T. Long, S. Li, D. A. Dixon, K. A. Peterson and K. O. Christe, Third row transition metal hexafluorides, extraordinary oxidizers, and lewis acids: Electron affinities, fluoride affinities, and heats of formation of WF6, ReF6, OsF6, IrF6, PtF 6, and AuF6, *Inorg. Chem.*, 2010, **49**, 1056–1070.

25 D. R. Lide, *CRC Handbook of Chemistry and Physics*, CRC Press, 85th edn., 2005.

26 G. Pilcher and H. A. Skinner, in *The Chemistry of the Metal-Carbon Bond*, eds. H. F. R and P. S, John Wiley & Sons Ltd, 1982, pp. 43–90.

27 R. J. Irving and M. A. . Ribeiro da Silva, Standard Enthalpies of Formation of Bis(pentane-2,4-dionato)copper(II) and Tetrakis[bis(pentane-2,4-dionato)cobalt(II)] and an Estimation of the Metal-Oxygen Bond Energies, *J. Chem. Soc. Dalt. Trans.*, 1981, 99–102.

28 W. Kąkołowicz and E. Giera, Standard enthalpies of formation of the chelate complexes of some 3d-electron elements with pentane-2,4-dione metal-oxygen bond energies and ligand-field stabilization energies, *J. Chem. Thermodyn.*, 1983, **15**, 203–210.

29 M. W. Chase, *NIST-JANAF Thermochemical Tables*, American Chemical Society ; American Institute of Physics for the National Institute of Standards and Technology, Washington D.C, 4th edn., 1998, vol. 9.

30 W. H. Johnson, A. A. Gilliland and E. J. Prosen, Heat of formation of titanium tetrabromide, *J. Res. Natl. Bur. Stand. Sect. A Phys. Chem.*, 1959, **62**, 67–69.

31 G. Al-Takhin, J. A. Connor, H. A. Skinner and M. T. Zafarani-Moattar, Thermochemistry of arenetricarbonylchromium complexes containing toluene, anisole, N,N-dimethylaninine, acetophenone and methylbenzoate, *J. Organomet. Chem.*, 1984, **260**, 189–197.

32 T. F. Bolles and R. S. Drago, The Enthalpy of Formation of Coordination Compounds of Trimethyltin Chloride, *J. Am. Chem. Soc.*, 1966, **88**, 3921–3925.

33 K. J. Cavell, J. O. Hill and M. R. J, Standard Enthalpy of Formation of Bis(diethyldithiocarbamato)nickel(ii) at 298 K and the Nickel-Sulphur Bond Energy, *J. Chem. Soc. Dalt. Trans.*, 1980, 763–766.

34 J. A. Martinho Simões, *Energetics of Organometallic Species*, Springer Netherlands, 1st edn., 1992.

35 M. Fulem, K. Růžička, V. Růžička, E. Hulicius, T. Šimeček, K. Melichar, J. Pangrác, S. A. Rushworth and L. M. Smith, Vapor pressure of metal organic precursors, *J. Cryst. Growth*, 2003, **248**, 99–107.

36 C. L. Yaws, *Yaws' Handbook of Thermodynamic Properties for Hydrocarbons and*

Chemicals, Gulf Publishing Company, 2009.

37 W. D. Good, D. W. Scott, J. L. Lacina and J. P. McCullough, Tetramethyllead: Heat of formation by rotating-bomb calorimetry, *J. Phys. Chem.*, 1959, **63**, 1139–1142.

38 J. A. Martinho Simoes and M. E. Minas de Piedade, in *Energetic of Organic Free Radicals*, eds. J. A. Martinho Simoes, J. F. Liebman and A. Greenberg, London, 1996.

39 C. T. Mortimer and J. Waterhouse, Enthalpy of combustion of diphenyl diselenide, *J. Chem. Thermodyn.*, 1980, **12**, 961–965.

40 J. R. Chipperfield, J. C. R. Sneyd and D. E. Webster, The thermorchemistry of the di-η5-cyclopentadienyl derivatives of the first transition series and their unipositive ions, *J. Organomet. Chem.*, 1979, **178**, 177–189.

41 H. Östmark, A. Helte and T. Carlsson, Guanylurea-dinitramide (FOX-12): A new extremely insensitive energetic material for explosives applications, *Proc. 13th Int. Detonation Symp. IDS 2006*, 2006, 121–127.

42 J. W. Fronabarger, M. D. Williams, W. B. Sanborn, D. A. Parrish and M. Bichay, KDNP - A lead free replacement for lead styphnate, *Propellants, Explos. Pyrotech.*, 2011, **36**, 459–470.

43 H. Gao, C. Ye, C. M. Piekarski and J. M. Shreeve, Computational characterization of energetic salts, *J. Phys. Chem. C*, 2007, **111**, 10718–10731.

44 H. Östmark, U. Bemm, A. Langlet, R. Sandén and N. Wingborg, The properties of ammonium dinitramide (adn): Part 1, basic properties and spectroscopic data, *J. Energ. Mater.*, 2000, **18**, 123–138.

45 J. J. Sabatini and K. D. Oyler, Recent advances in the synthesis of high explosive materials, *Crystals*, 2015, **6**, 1–22.

46 B. Nazari, M. H. Keshavarz, M. Hamadanian, S. Mosavi, A. R. Ghaedsharafi and H. R. Pouretedal, Reliable prediction of the condensed (solid or liquid) phase enthalpy of formation of organic energetic materials at 298 K through their molecular structures, *Fluid Phase Equilib.*, 2016, **408**, 248–258.